Broadband ultrafast spectroscopy on mixed–dimensional InAs/GaAs systems

vorgelegt von

Diplom–Physiker Mirco Kolarczik

ORCID: 0000-0001-8368-453X

von der Fakultät II — Mathematik und Naturwissenschaften
der Technischen Universität Berlin
zur Erlangung des akademischen Grades

Doktor der Naturwissenschaften
— Dr. rer. nat. —

genehmigte Dissertation

Promotionsausschuss:
Vorsitzender: Prof. Dr. rer. nat. Stephan Reitzenstein (TU Berlin)
Gutachterin: Prof. Dr. rer. nat. Ulrike Woggon (TU Berlin)
Gutachter: Prof. Dr. rer. nat. Tobias Kampfrath (FU Berlin)
Gutachter: Dr. rer. nat. Jacek Kasprzak (Institut NÉEL, Grenoble, Frankreich)

Tag der wissenschaftlichen Aussprache: 16. Januar 2019.

Berlin 2019

Daneben gibt es aber noch eine Reihe andrer Philosophen, die die Möglichkeit einer Erkenntnis der Welt oder doch einer erschöpfenden Erkenntnis bestreiten. […] Die schlagendste Widerlegung dieser wie aller andern philosophischen Schrullen ist die Praxis, nämlich das Experiment und die Industrie. Wenn wir die Richtigkeit unsrer Auffassung eines Naturvorgangs beweisen können, indem wir ihn selbst machen, ihn aus seinen Bedingungen erzeugen, ihn obendrein unsern Zwecken dienstbar werden lassen, so ist es mit dem Kantschen unfaßbaren „Ding an sich“ zu Ende.

Friedrich Engels

Abstract

This thesis deals with light matter interaction and electron dynamics in coupled systems of nanostructured III-V semiconductors, particularly with quantum dots embedded in quantum wells. Its focus is on the role of dimensionality and the characterization of quantum dot states with respect to their two- and many-level nature. The sample under investigation is a semiconductor optical amplifier under standard operating conditions, in particular at room temperature.

An essential part of the work and a prerequisite of the experimental results is the re–development of a setup for heterodyne detection of laser pulses. Compared to the established pump–probe experiment, the duration of a single measurement was reduced by a factor of 100. This allowed the introduction of simultaneous multi–power measurements that are used to investigate the non–linear response of the system. More than that, several novel techniques have been developed: The Frequency Resolved Optical Short–pulse Characterization by Heterodyning (FROSCH) for pulse shape analysis, the sideband pump–probe technique for low signal measurements, and finally a method for two–dimensional coherent spectroscopy. All these techniques can be used on the same setup without significant realignment. A detailed description is given in part II.

In a first set of experiments we were able to observe Rabi oscillations of the quantum dot exciton ground state at room temperature as a typical property of two–level systems. These observations on a femtosecond timescale were enabled by the FROSCH technique when the ground state oscillations caused a characteristic pulse shape modification.

On the other hand, the many–level characteristics dominated a large set of pump–probe measurements presented in chapter 10. Under the assumption of a linear superposition of zero–dimensional quantum dot states on the one hand and two- or three-dimensional continuum states on the other hand, it was not possible to describe the electron dynamics. The introduction of "crossed excitons" into the model allowed for a consistent explanation of the gain dynamics. These crossed excitons are formed by Coulomb attraction of a zero–dimensional single carrier state and another one of higher dimensionality. The crossed excitons affect the optical transitions as well as the carrier diffusion in the quantum well.

The apparent contradiction in these findings with respect to the two- and many-level characteristics is resolved in the final experimental part by two–dimensional coherent spectroscopy. This technique uses white laser pulses and merges all technical approaches developed in the previous parts. This allows the observation of the coherent coupling of states with large energy separation. The reliability of the technique is proven by the extraction of dephasing times that are in excellent agreement with literature values. In the two–dimensional spectra we find distinct signatures of crossed excitons that can be investigated in detail by this novel technique.

Zusammenfassung

Diese Dissertation setzt sich mit der Licht–Materie–Wechselwirkung und der Elektronendynamik in gekoppelten Systemen von nanostrukturierten III-V–Halbleitern am Beispiel in Quantenfilme eingebetteter Quantenpunkte auseinander. Dabei wird insbesondere der Einfluss der Dimensionalität untersucht und die Frage nach der Charakterisierung von Quantenpunktzuständen hinsichtlich ihrer Eigenschaften als Zwei- bzw. Viel-Niveau-Systemen behandelt. Als Probe dient ein optischer Halbleiter-Verstärker, der unter typischen Anwendungsbedingungen untersucht wird, also insbesondere bei Raumtemperatur.

Wesentlicher Bestandteil der Arbeit und Grundlage der experimentellen Ergebnisse war die Weiterentwicklung eines Aufbaus zur heterodynen Detektion von Laserpulsen. Dabei konnte für die etablierte Pump-Probe-Technik die nötige Messzeit um einen Faktor 100 verkürzt werden. Dies ermöglichte auch die Einführung simultaner Messungen mit abgestuften Anregungsintensitäten zur Untersuchung nichtlinearer Antworten des Systems. Darüber hinaus wurden mehrere neue Techniken entwickelt: Die “Frequency Resolved Optical Short-pulse Characterization by Heterodyning” (FROSCH) zur Analyse von Pulsformen, die Seitenband-Pump-Probe zur Messung sehr kleiner Signale und zuletzt ein Aufbau zur zweidimensionalen kohärenten Spektroskopie. All diese Techniken sind ohne nennenswerte Umbauarbeiten am selben Versuchsstand nutzbar und im Teil II der Dissertation detailiert beschrieben.

Zunächst konnten mit der FROSCH–Technik Rabi-Oszillationen des Exzitonen-Grundzustandes als typische Eigenschaft eines Zwei-Niveau-Systems in Quantenpunkten bei Raumtemperatur nachgewiesen werden. Die Beobachtung dieses Effekts auf der Zeitskala von Femtosekunden wurde durch die FROSCH-Technik ermöglicht. Das Oszillieren des Grundzustandes führt dabei zu einer charakteristischen Pulsverformung.

Im Gegensatz dazu zeigte sich die Viel-Niveau-Charakteristik in einer Vielzahl von Pump-Probe-Messungen, die in Abschnitt 10 präsentiert werden. Die erhobenen Daten konnten dabei nicht im Rahmen einer linearen Überlagerung von nulldimensionalen Zuständen einerseits und zwei- bzw. dreidimensionalen Zuständen andererseits erklärt werden. Durch die Einführung gekreuzter Exzitonen (“crossed excitons”), die einen durch Coulomb-Weschselwirkung gebundenen Zustand je eines null- und eines höherdimensionalen Einzelladungsträgerzustands darstellen, konnte eine konsistente Erklärung für die beobachtete Verstärkungsdynamik geliefert werden. Dies gilt sowohl in Hinblick auf die Anregung optischer Übergänge als auch bezüglich der Ladungsträgerdiffusion im Quantenfilm.

Die Vereinigung dieser widersprüchlich anmutenden Ergebnisse hinsichtlich Zwei- oder Viel-Niveau-Charakteristik erfolgt im letzten experimentellen Teil mit Hilfe der zweidimensionalen kohärenten Spektroskopie. Diese Technik vereint alle zuvor entwickelten technischen Ansätze und ermöglicht durch den Einsatz von weißen Laserpulsen die Identifikation kohärenter Kopplungen von Übergängen mit großem energetischen Abstand. Die Zuverlässigkeit der Technik wird durch die Extraktion von Kohärenzzeiten der Quantenpunkte und den Abgleich mit Literaturdaten belegt. Darüber hinaus weisen die zweidimensionalen Spektren deutliche Signaturen gekreuzter Exzitonen auf, womit erstmalig eine direkte Beobachtung dieser optischen Übergänge möglich wird.

Contents

Acknowledgment

Many people contributed to the work presented here. I would like to thank all of them and to apologize to anyone who is not listed explicitly.

First of all, I would like to thank Ulrike Woggon, my principal investigator and supervisor. Her trust and patience were the basis for many new ideas that took lots of time to evolve, but have been finished succesfully.

During my membership in the Graduiertenkolleg 1558 (GRK 1558), Andreas Knorr acted as my second supervisor: My cordial thanks for many discussions and a fruitful cooperation with his entire group, especially with Sandra Kuhn.

The success of our work would have not been possible without the contribution of Nina Owschimikow. As the team leader of the ultrafast spectroscopy sub–group she enabled the work in the lab, deepened the insight into the physics, and guided the publication of our results. Widening our scope towards transitionmetal-dichalcogenides (TMDs) was one of her merits. More than that, she became a real friend.

Many other colleagues contributed by discussions and hands–on assistance: Nicolai Grosse, who recruited me for the group and brought in his profound knowledge of quamtum optics; Alexander Achtstein contributed in many cases as an expert for nanocrystals; Yücel Kaptan, Bastian Herzog, and Sophia Helmrich were the best lab mates one can imagine. And, finally, my student assistants as well as bachelor and master students Mitra Pasche, Florian Buchholz, Kevin Thommes, and Aris Simos brought new impulses into the group, everyone in her or his very own way.

Jenny Schwadtke, our secretary, deserves special thanks for shielding us from the administration and for doing much more than her duty for us.

An invaluable stimulation of our experimental efforts was gained from the permanent interaction with our colleagues of the Insitut für Theoretische Physik. Together with the group of Kathy Lüdge and Eckehard Schöll and in particular with Benjamin Lingnau and Julian Korn, we developed numerous experimental approaches and models for the description of carrier dynamics.

A highlight of my work was my research stay at the University of Texas (UT) at Austin with the group of Elaine Li. The warmhearted welcome to her group and the collaboration during her Humboldt stays in Berlin made this collaboration special, professionally as well as personally. I owe special thanks to Akshay Singh, not only for introducing me to the Indian community of Austin and to the “Crown and Anchor Pub”, but also for allowing me to contribute to his setup. The work with him and Kha Tran granted me new insights into the TMD world and allowed first applications of my ideas for multiband measurements.

Another special experience was my involvement in the PhotonX proposal for a Cluster of Excellence. The coordination of 25 principal investigators in the Berlin–Brandenburg area was challenging as well as exciting. Besides Ulrike Woggon, I would like to thank Stephan Reitzenstein and Oliver Benson for this opportunity.

Finally, I’d like to express my gratitude to the institutions that enabled our research, namely the Technische Universität Berlin (TU), the UT at Austin, the Deutsche Forschungsgemeinschaft (DFG), the Sonderforschungsbereich 787 (SFB 787), and the GRK 1558. Not only their funding, but also the countless people they represent were through all our work a solid foundation and reliable backup.

Introduction

Over the past two decades the availability of mass data transfer had an enormous impact on the lives of billions of people in the industrialized countries. Besides the achievements in solid state physics and nanotechnology that enabled the miniaturization of processing units and data memories, the key technology of connecting the globe is the optical data transfer. The interface between optics and electronics is still the hotspot of hardware development. Semiconductors are the material system of choice to link both worlds. On established platforms—such as the III-V semiconductors this thesis deals with—nanostructuring opens new avenues and generates a complexity that is experimentally and theoretically challenging. On the other hand, promising new material classes like the TMDs arise—and are nanostructured as well. Independent of the platform: Understanding interfaces and coupling mechanisms between subsystems is the path to future hardware development.

Nowadays, hardware development does not exhaust the requirements of technology development any more. "Big data" is one of the buzzwords of our days. The data processing structures do not yet level the new abilities of modern hardware. Furthermore, the user interfaces for scientists in the lab and the data handling and evaluation methods become a bottleneck for the efficient generation of ideas. While big companies like Google or Tencent address these problems using their enormous manpower, comparatively small university labs like ours fall behind. From a societal perspective, this means that publicly funded technology development is at risk.

This is the environment in which this thesis is settled. Before going into the physics, a look at the experimental background is necessary. We inherited an established setup in 2011 on which I collected the data for my diploma thesis. This heterodyne setup and its development are at the core of the present thesis. Despite continuous data production, the original setup was not up–to–date anymore: Single data point acquisition was on the timescale of seconds and there were no functionalities for convenient alignment. The data transfer was digital, but via the outdated General Purpose Interface Bus (GPIB) system which limited further development. In the course of this thesis, the setup was improved tremendously, as will be described in detail in part II:

- Frequency Resolved Optical Short–pulse Characterization by Heterodyning (FROSCH) has been developed for spectro-temporal pulse analysis, the More–Or–Less Characterization by Heterodyning (MOLCH) became a valuable alignment tool.
- The traditional pump-probe (PP) data acquisition (DAQ) rate is today more than 1000 times higher than five years ago, scanning a full curve about 100 times faster, while the data quality has been significantly increased.
- While traditional PP requires signal levels of 10^{-2}, the sideband PP has been developed for the investigation of low signals in the range of 10^{-5} without losing the phase resolution of heterodyne detection.
- For traditional PP as well as FROSCH, the Simultaneous multi-power measurement (SMPM) has been implemented to investigate pulse power dependencies with high reliability.

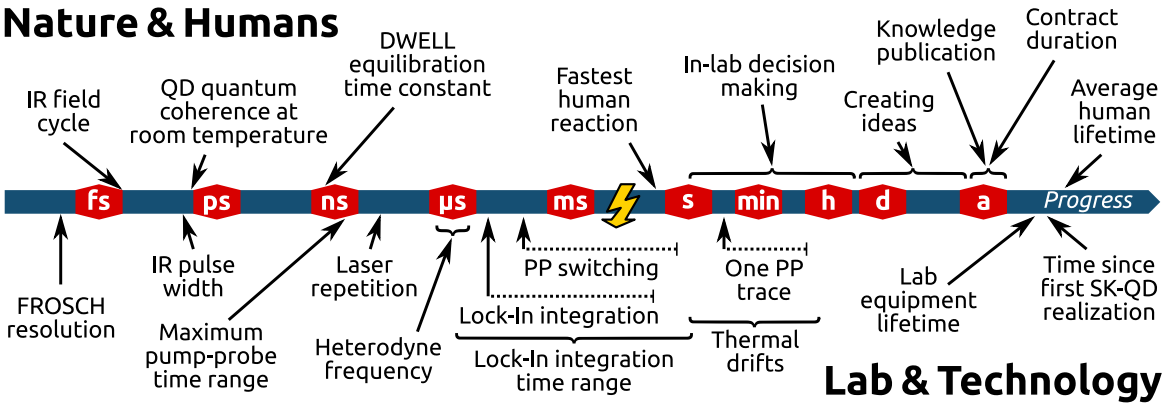

Figure 1: The logarithmic time scale visualizes the widespread number of events and circumstances this work deals with. The yellow flash in the millisecond time range indicates line noise at 50 Hz and 100 Hz, respectively, posing an obstacle to every experiment based on electrical signals. Important improvements of the experimental setup during this thesis are indicated by dotted lines, notably leapfrogging the line noise range.

- The concepts of traditional PP, sideband PP, SMPM, and FROSCH have finally been merged into a two-dimensional coherent spectroscopy (2DCS) setup that we refer to as Supercontinuum–based Two–dimensional Observation of Radiation Coherence by Heterodyning (STORCH). This setup also utilizes the broadband spectra of a fiber laser system with supercontinuum generation, which enables the observation of state coupling over an unusual wide energy range.

This development aimed to optimize the setup on every part of the timescale shown in fig. 1. The FROSCH technique enabled us to have a look into the single cycles of our signals, corresponding to a temporal resolution of about 100 as. This was a prerequisite for the results in chapter 9 that required sub–pulse–duration time resolution not provided by PP experiments. The reduction of lock–in integration times from the millisecond to the microsecond time range allowed the DAQ at kilohertz rates and also reduced the susceptibility of the setup to acoustic noise and thermal drifts. This fast DAQ approach discussed in chapter 5 enabled us to explore a much larger part of the parameter space. The results in sections 10.1 and 10.2 are mainly based on this approach.

With FROSCH and STORCH, the concept of Fourier transform spectroscopy (FTS) has enriched our methodological toolbox. This widened scope makes it necessary to emphasize the respective terminology in this thesis. This is the motivation to start in chapter 1 with a detailed collection of basic terms of Fourier analysis and a discussion of the frequency domain.

The sample under investigation is a semiconductor optical amplifier (SOA) with indium arsenide (InAs) quantum dots (QDs) embedded in an indium gallium arsenide (InGaAs) quantum well (QW). We nevertheless do not focus on technology development, but on the fundamental understanding of the coupling mechanisms of these subsystems. The questions that arise under these circumstances are, for example: Does the QD preserve its characteristic properties as a discrete two level system (2LS)? Is the coupled system a superposition of its constituents with defined transition paths—or is the new system more than the sum of its parts? What channels interconnect the large scale system in terms of excitation paths and carrier kinetics? And if there are new properties, can we utilize them?

This thesis is a collection of answers to most of these questions. These answers have already been published in various journal articles, but under varying circumstances. I would like to take

the opportunity of this thesis to present the results in an overarching terminology and under consideration of the development process. One important step to reach this goal is the introduction of the four pulse scheme (4PS) in section 1.2.3. Although many graphs might seem familiar from the former publications, almost everyone of them has been revised and adjusted to comply with the symbols and theoretical background presented in the following chapters.

Part I.

Theoretical background

1. General concepts

1.1. The Fourier space

Understanding heterodyne experiments means understanding the frequency domain. Here and in the following, any symbol ν refers to a frequency, while the analog symbol ω refers to the angular frequency with

$$\omega = 2\pi\nu. \tag{1.1}$$

For the sake of linguistic convenience, the term "angular" will often be omitted, the reader is asked to decide on the basis of the symbols. In a similar manner, the photon energy

$$E = h\nu = \hbar\omega \tag{1.2}$$

with the Planck constant h and the reduced Planck constant $\hbar = h/(2\pi)$ will be used as an alternative representation of the frequency.

The one-dimensional Fourier transform (FT) F of a function $f : \mathbb{R} \to \mathbb{C}$ is defined as

$$F(\nu) = \mathcal{F}\left\{f(t)\right\}(\nu) = \int_{-\infty}^{\infty} f(t')e^{-i2\pi\nu t'}\,\mathrm{d}t', \tag{1.3a}$$

$$f(t) = \mathcal{F}^{-1}\left\{F(\nu)\right\}(t) = \int_{-\infty}^{\infty} F(\nu')e^{i2\pi\nu' t}\mathrm{d}\nu', \tag{1.3b}$$

where a representation was chosen that omits prefactors and uses a notation in ν.[18] From that mathematical point of view, the Fourier transformation $\mathcal{F}$ and the inverse Fourier transformation $\mathcal{F}^{-1}$ are structurally identical. All considerations in this section apply in both directions, although from a technical point of view it might be easier to obtain sharp spectral lines in the lab than it is to create short pulse durations. There is a reciprocal relation between pulse duration and spectral width. This can be easily calculated for the important case of the Gaussian pulse with a spectrum $F_{\mathrm{Gauss}}(\nu) = \exp(-4\ln 2(\nu/\sigma)^2)$, where σ denotes the spectral full width at half maximum (FWHM). The corresponding temporal signal is

$$f_{\mathrm{Gauss}}(t) = \sigma\sqrt{\frac{\pi}{4\ln 2}}\exp\left(-\frac{\pi^2\sigma^2}{4\ln 2}t^2\right) \tag{1.4}$$

with a temporal FWHM of $(2\ln 2)/(\pi\sigma)$. The time–bandwidth product for the Gaussian pulse is therefore $(2\ln 2)/\pi = 0.441$, which is often used to approximate the minimal pulse duration for a given spectrum or the necessary spectral width for a desired pulse duration.

In this calculation, a real function $F_{\mathrm{Gauss}}(\nu)$ was chosen, which means a phase of zero for all spectral components. This resulted in a real $f_{\mathrm{Gauss}}(t)$ centered at $t = 0$. A modification of the spectral phase would have significant influence on the temporal signal: Adding a constant to the spectral phase shifts the carrier wave temporally, while the envelope remains unchanged. A linear tilt, on the other hand, shifts the temporal envelope. Finally, bending the phase function results in a "chirped" pulse. The pulse duration is increased, the pulse is not transform–limited anymore.

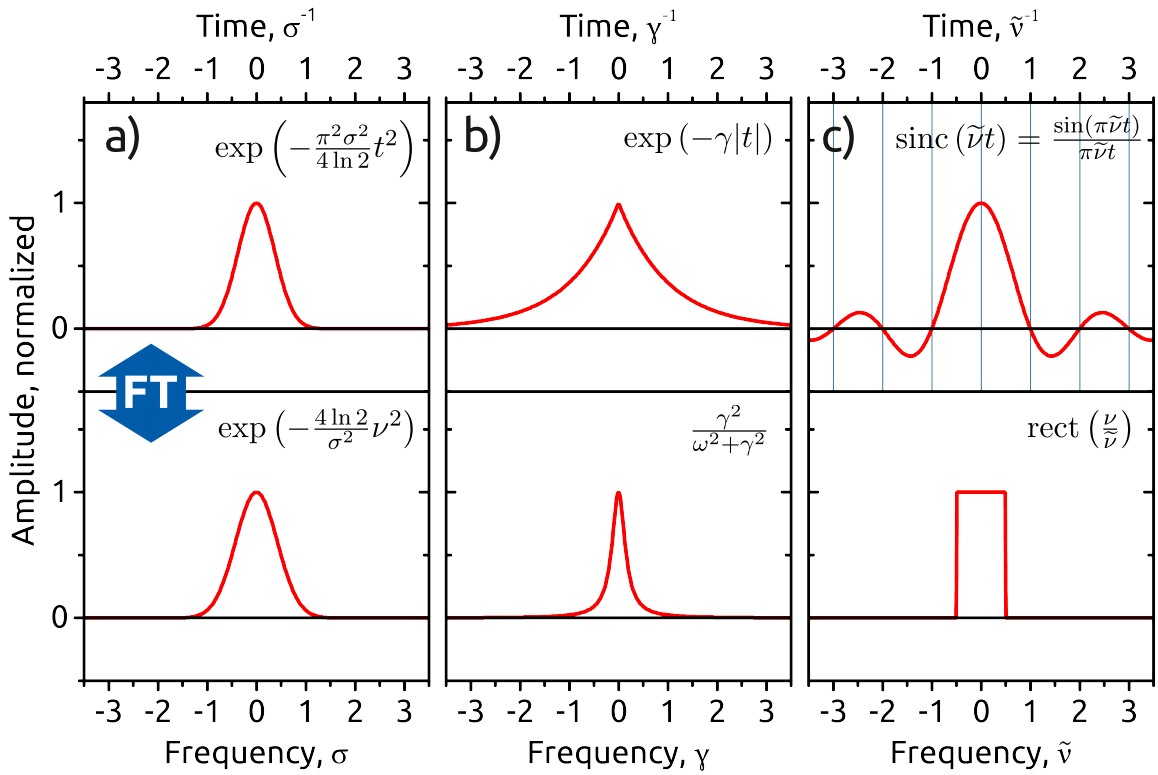

Figure 2: Three fundamental cases of FTs: a) A temporal Gaussian signal also has a Gaussian spectrum. b) The exponential decay has a Lorentzian spectrum. c) A rectangular spectrum of width $\widetilde{\nu}$ results in a temporal sinc-function with equally spaced zeros.

The pulse has a "positive chirp" if the components with long wavelengths arrive earlier than the short wavelengths, which occurs upon normal dispersion in optical media.

Besides the Gaussian, there are two other fundamental Fourier transforms that will occur several times. They are illustrated in fig. 2. In fig. 2 (b), the exponential temporal decay is shown, which corresponds to a Lorentzian line in the spectrum. This case is important for optical transitions (section 3.2.1) as well as for frequency filters (section 1.3.2). In fig. 2 (c), the FT correspondence of the sinc and the rect function is shown. This correspondence is important for a spectral rectangle, e.g. in the case of pulse amplitude shaping, but also for a temporal rectangle (section 7.3).

1.1.1. Products of signals: Convolution, cross–correlation, coherence

The multiplication of two monochrome signals, $f(t) = \exp(i\omega t)$ and $g(t) = \exp(i\widetilde{\omega}t)$, results in

$$f(t)g(t) = \exp i(\omega + \widetilde{\omega})t \tag{1.5}$$

and thereby creates a new mode $\omega + \widetilde{\omega}$. The generation of new frequency bands will often be caused by two or more original bands that mix in a non–linear element.

In interferometric measurements we will need to deal with products of more complex temporal signals and their spectra, respectively. The *convolution* of two signals f and g is defined as

$$(f * g)(t) = \int_{-\infty}^{\infty} f(t')g(t - t')\mathrm{d}t' \tag{1.6}$$

and the well–known convolution theorem

$$\mathcal{F}\left\{(f * g)(t)\right\}(\omega) = \mathcal{F}\left\{f(t)\right\}(\omega) \cdot \mathcal{F}\left\{g(t)\right\}(\omega) \tag{1.7}$$

says that its spectrum is the product of the spectra of the convoluted signals. In contrast to the convolution, the *cross–correlation* is defined as

$$(f \star g)(t) = \int_{-\infty}^{\infty} f^*(t')g(t+t')\mathrm{d}t' \tag{1.8}$$

and its FT is given by

$$\mathcal{F}\left\{(f \star g)(t)\right\}(\omega) = \mathcal{F}\left\{f(t)\right\}^*(\omega) \cdot \mathcal{F}\left\{g(t)\right\}(\omega). \tag{1.9}$$

The mathematical cross–correlation leads directly to one of the central physical terms: the signal *coherence*. The coherence of two signals f and g is given by

$$C_{fg}(t) = \left| \frac{2\,(f \star g)(t)}{(f \star f)(0) + (g \star g)(0)} \right|. \tag{1.10}$$

In the auto–correlation case $f = g$, the coherence is obviously $C_{ff}(0) = 1$ and $C_{ff}(t > 0) \leq 1$. One will usually observe a coherence decay when t increases.

Signal convolutions are also very important for the FT of real world signals. As can be seen from the definition of the FT in eq. (1.3a), infinite temporal information is required for a full FT. This is not possible in general and sometimes not desired in particular. To restrict the Fourier analysis to a certain range, a window function $w(t)$ with $w(t) \to 0$ for $t \to \pm\infty$ is applied. According to eq. (1.7), the FT of $f(t)w(t)$ is the convolution of $\mathcal{F}\left\{f(t)\right\}$ and $\mathcal{F}\left\{w(t)\right\}$. In the case of a Gaussian window the resulting transform

$$G(\omega, t, \Delta t) = \frac{1}{\sqrt{2\pi}} \int_{-\infty}^{\infty} \exp\left[-\left(\frac{t'-t}{\Delta t} \right)^2 \right] f(t')e^{-i\omega t'}(t)\mathrm{d}t' \tag{1.11}$$

is referred to as the Gabor transform (GT). The GT does only partially transfer information from the time to the frequency domain and vice versa. Δt is a tuning parameter that determines the composition of spectral and temporal information, with $G(\omega, t, \Delta t) \to \mathcal{F}\left\{f(t)\right\}(\omega)$ for $\Delta t \to \infty$.

1.1.2. Composing signals: Modulation, repeating signals, discrete Fourier transform

When two monochrome signals with different frequencies interfere, there is a periodic change between constructive and destructive interference. This oscillation of the signal envelope is called *beating*. The beating is one example for the concept of signal *modulations*. In the time domain, a modulation is the multiplication of a *carrier signal* $f_{\mathrm{car}}(t) = \cos(\omega t + \varphi)$ with a complex modulation signal $g_{\mathrm{mod}} = \widetilde{A}_0 + \widetilde{A}\exp(i\widetilde{\omega}t)$. The product of the real oscillations is now given by

$$f_{\mathrm{car}}(t)g_{\mathrm{mod}}(t) = \frac{1}{2}\left(\widetilde{A}_0 \left(e^{i\omega t + i\varphi} + e^{-i\omega t - i\varphi} \right) + \widetilde{A}\left(e^{i(\omega+\widetilde{\omega})t} + e^{-i(\omega-\widetilde{\omega})t} \right) \right). \tag{1.12}$$

In the frequency domain, the modulation is therefore represented by three components: the original carrier band at ω and two *sidebands*, an upper one at $\omega + \widetilde{\omega}$ and a lower one at $\omega - \widetilde{\omega}$. Without a constant offset $\mathrm{Re}(\widetilde{A}_0)$, the carrier band would vanish. A signal can be modulated both, in amplitude and in phase. The particular type of the modulation is defined by the orientation of the sidebands with respect to the main band. This is illustrated in fig. 3.

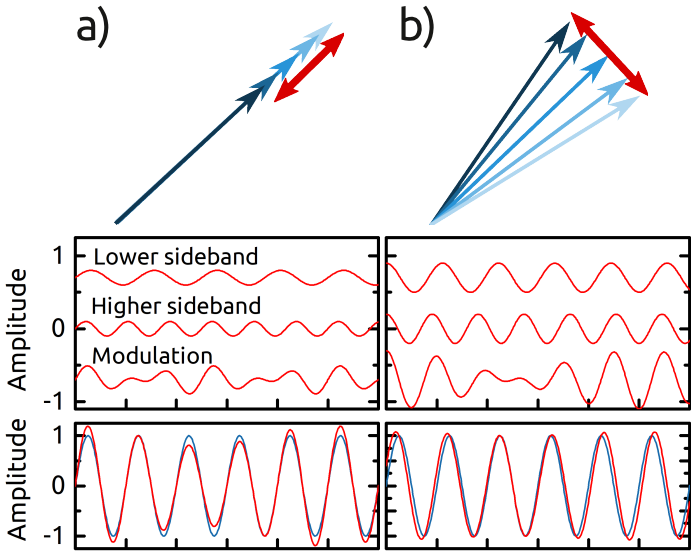

Figure 3: Illustration of amplitude modulation (a) and phase modulation (b). In the upper row, the signal is represented by a complex vector that varies temporally (shades of blue). This variation can be approximated by a sideband (red arrow) that is added to the average value of the oscillating signal. In the middle row, the contributions of the sidebands are displayed. The lower row shows the resulting signals (red) in comparison to the main band (blue).

This example showed that a modulation of the time signal is represented by a replication of the main band in form of a sideband. The concept works, of course, also the other way round: A repetition of the temporal signal causes a modulation of the frequency signal. This is especially the case for pulsed lasers, where the time signal (the pulse) is not only duplicated, but repeated infinitely. With a repetition rate $\widehat{\nu}_{\mathrm{rep}}$, the corresponding spectrum is not only modulated by $\cos(\nu/\widehat{\nu}_{\mathrm{rep}})$, but by

$$f_{\mathrm{rep}}(\nu) = \sum_{n\in\mathbb{N}} \cos\left(\frac{\nu}{n\widehat{\nu}_{\mathrm{rep}}}\right) = \sum_{n\in\mathbb{N}} \delta(\nu - n\widehat{\nu}_{\mathrm{rep}}). \tag{1.13}$$

The spectrum of a pulsed laser is therefore composed of sharp laser modes. Although a real world laser does not provide δ-like modes, the mode spacing $\widehat{\nu}_{\mathrm{rep}}$ can exceed the mode width easily by a factor of 10^6.[19] This extreme reduction of the spectrum is at the core of heterodyne detection: All this free spectral range in between the sharp laser modes can be used to encode information.

Mathematically very similar to the repeating laser are some considerations about the discrete FT. The discrete sampling of a continuous signal will also result in an artificially repeating spectrum. This effect is called *aliasing*. The second problem of discrete sampling is the impossibility of infinite temporal information. In the most simple case, the measured signal will be a multiplication of the actual signal and a rectangular window function. Also here, the measured spectrum will be a convolution of the original signal and the applied sampling window according to eq. (1.6). These facts result in some basic rules for discrete FT:

- Increasing the density of sampling points results in a wider spectral range due to the avoiding of aliasing.
- An increased temporal range will improve the spectral resolution because the corresponding window function spectrum is narrower.

- It should be avoided to apply a rectangular window unless the sampled signal vanishes at the border of the sampling window. As its FT is an extended sinc-function, the rectangular window will result in a "ringing". The spectrum can be improved at the expense of peak–broadening by the numerical application of a window that vanishes at the border.

1.1.3. Spatial Fourier transform: The k-space

Now that we already touched on laser resonators, it is time for a brief discussion of space and its Fourier correspondent, the k-space. The laser resonator is one particular representation of the general *particle in a box* problem. A closed box of width L (in one dimension) restricts the allowed spatial frequencies to wavelengths λ with $n\lambda/2 = L$ ($n \in \mathbb{N}$). The respective wave numbers are

$$k_n = \frac{2\pi}{\lambda_n} = \frac{\pi}{L} n. \tag{1.14}$$

The allowed spatial frequencies are therefore homogeneously distributed in the k-space.

Closely related to the particle in a box is the finite potential pot. This problem will become very important under varying aspects. There is no conceptual difference between the treatment of light and matter in this respect. In the case of light, the Helmholtz equation

$$\left(\Delta + \frac{\omega^2}{{c_0}^2} n(\boldsymbol{r})\right) \mathcal{E}(\boldsymbol{r}) = 0 \tag{1.15}$$

can be used to calculate resonator modes or waveguide modes in a fiber based on the *refractive index* landscape $n(\boldsymbol{r})$. In the case of matter, we use the time–independent *Schrödinger equation*

$$\widehat{H}\psi(\boldsymbol{r}) = \left(-\frac{\hbar}{2m}\Delta + V(\boldsymbol{r})\right)\psi(\boldsymbol{r}) = E\psi(\boldsymbol{r}) \tag{1.16}$$

to determine particle states in a potential landscape $V(\boldsymbol{r})$. Depending on the symmetry of the potential landscape, the coordinate system and a corresponding representation of the Laplace operator Δ is chosen.

We restrict the discussion here to the textbook case of one dimension x, a particle obeying eq. (1.16), and a finite potential pot of width L. This will be the typical approach to determine quantum dot (QD) states. The potential is given by

$$V(x) = \begin{cases} -V_0: & |x| \le L/2 \\ 0: & \text{else.} \end{cases} \tag{1.17}$$

The problem can be solved in k-space using the ansatz $\psi(x) = a_i \exp(kx) + a_j \exp(-kx)$. Here, we need to distinguish between the different cases

$$\psi(r) = \begin{cases} a_1 \exp\left(k_{\text{out}} x\right) + a_2 \exp\left(-k_{\text{out}} x\right): & x < -L/2 \\ a_3 \exp\left(k_{\text{in}} x\right) + a_4 \exp\left(-k_{\text{in}} x\right): & |x| \le L/2 \\ a_5 \exp\left(k_{\text{out}} x\right) + a_6 \exp\left(-k_{\text{out}} x\right): & x > L/2 \end{cases} \tag{1.18}$$

with wave vectors outside and inside of the pot of

$$k_{\text{out}} = \sqrt{-2mE}/\hbar \tag{1.19a}$$

$$k_{\text{in}} = \sqrt{-2m(E + V_0)}/\hbar. \tag{1.19b}$$

The continuity of $\psi(x)$ and $\partial_x\psi(x)$ restricts the coefficients a_i. Two cases need to be discussed.

Bound states exist for $-V_0 < E < 0$. Outside the potential pot, $\psi(x)$ decays exponentially ($a_2 = a_5 = 0$). Inside the pot, the solution is given by sine ($a_3 = a_4$) and cosine ($a_3 = -a_4$) functions. Inside and outside wave vectors are related by

$$k_{\mathrm{out}} = \tan\left(k_{\mathrm{in}}\frac{L}{2}\right) k_{\mathrm{in}}. \tag{1.20}$$

Both, eqs. (1.19) and (1.20), cannot be fulfilled for arbitrary energy values E. In the general case, a numerical solution is necessary. In the limit case of $V_0 \to \infty$, representing the particle in a box, the allowed energies are given by

$$E_n + V_0 = \frac{h}{8m^*L}n^2. \tag{1.21}$$

For $E > 0$, there are no more bound states. Although these states will still be calculated according to the particle in a box model, e.g. using periodic boundary conditions, we will refer to those states as *continuum states*. The continuum has an extension far beyond L, which makes the energy separation between the single states (eq. (1.21)) negligible. There are still different wavevectors inside and outside the pot according to eq. (1.19), but now also eq. (1.19a) is imaginary. Continuum states are extended states oscillating at a higher spatial frequency above the pot.

1.2. Electric field symbol conventions

1.2.1. Temporal and spectral representation

In the context of this thesis it will be unnecessary to consider electric fields as vectors. An electric field is therefore a real scalar. For the description of oscillating fields, however, it is convenient to define the complex electric field $\mathcal{E}(t)$. We will omit a special symbol for the real part of the electric field and specify it by $\mathrm{Re}(\mathcal{E}(t))$ if necessary. The complex field spectrum $\mathcal{E}(\nu)$ is defined as

$$\mathcal{E}(\nu) = \mathcal{F}\left\{\mathcal{E}(t)\right\}. \tag{1.22}$$

The same symbol $\mathcal{E}$ will be used for both, temporal and spectral representation, thus it will be depicted explicitly as $\mathcal{E}(t)$ or $\mathcal{E}(\nu)$, respectively. In cases of a discrete spectral mode distribution, $\mathcal{E}(\nu)$ will be replaced by $\mathcal{E}_\nu$.

1.2.2. Frequency ranges

Electrical frequencies will span an enormous range in the following. This has been already indicated in fig. 1. From the highest frequencies in the THz range to switching frequencies at kHz to thermal drifts of optical paths on the timescale of minutes: From the perspective of the field description there is no fundamental difference. My goal is to present an overarching description of all these frequency ranges. A labeling convention will ease the identification of the functionality of a certain frequency:

Light fields: ν. Light fields that will be found mostly in the range around 250 THz will be labeled without an additional character on top.

Laser mode spacing: $\widehat{\nu}$. Frequencies $\widehat{\nu}$ in the range of the laser repetition rate $\widehat{\nu}_{\mathrm{rep}} = 75.4\,\mathrm{MHz}$ will be labeled with a hat. This includes modulation frequencies that are used to shift laser modes by acousto-optic modulators (AOMs). As the subtraction of $\widehat{\nu}_{\mathrm{rep}}$ will often result in an almost equivalent result, a prime will indicate a respective shift: $\widehat{\nu}' = \widehat{\nu} - \widehat{\nu}_{\mathrm{rep}}$.

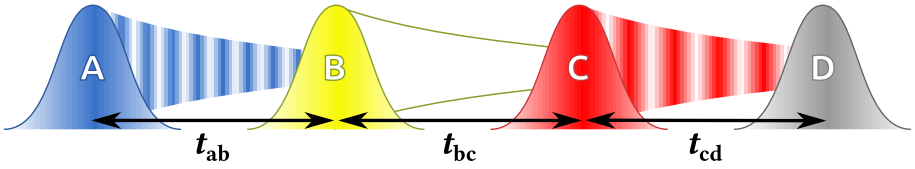

Figure 4: The general four pulse scheme (4PS). The pulses are labeled A to D with corresponding delays t_{ij}.

Slow modulation frequencies: $\widetilde{\nu}$. Switching and modulation frequencies in the range from 0 Hz to few MHz will be labeled by a tilde.

Resulting signals may include all these components. In this case and under consideration of section 1.1.2 it is important to have in mind that often $\nu + \widetilde{\nu} \not\approx \nu$.

1.2.3. The four pulse scheme

Different types of experiments will bring in different terminology. For example, in our publications the terms "reference pulse"[1–5,7,10,12] and "local oscillator"[9,15] refer to one and the same pulse. The usage depends on the experimental context.

One goal of this thesis is to give an overarching description of the experiments. Therefore I decided to use a unified terminology to describe all heterodyne experiments. The pulse labeling follows the terminology of two-dimensional coherent spectroscopy (2DCS).[20] The pulse sequence is shown in fig. 4. Four pulses will be sufficient to describe any experiment, they are labeled from A to D. In this scheme, pulse D will correspond to the "reference pulse". On the other hand, the traditional 2DCS labeling of pulse delays τ, T, and t is unhandy. The τ, for example, will be reserved for decay times within this thesis. Pulse delays are alternatively denoted t_{ij} where i and j depict the respective pulses (in lower case). Thus the traditional 2DCS notation corresponds to this notation according to $\tau \equiv t_{\mathrm{ab}}$, $T \equiv t_{\mathrm{bc}}$, and $t \equiv t_{\mathrm{cd}}$.

1.3. Transfer functions

A transfer function (TF) is a mathematical expression that describes the modification of a signal upon the passage of an object. There are numerous objects, e.g. semiconductor devices (samples) or electrical frequency filters, that modify a passing signal. Therefor it will be useful to define a general terminology for this work, although this terminology might deviate from the strict definition of TFs in linear system engineering.[21]

1.3.1. Differential gain and phase

In our experiments, the phase of the signal waves is very important, so the signals will be described by their complex field representation $\mathcal{E}(\nu)$ rather than by their power. For a single element, a TF is given by

$$\mathcal{E}_{\mathrm{out}}(\nu) = \mathfrak{T}\mathcal{E}_{\mathrm{in}}(\nu) = \left[Ge^{i\Phi}\right]\mathcal{E}_{\mathrm{in}}(\nu) \tag{1.23}$$

with the (field) gain $G \in \mathbb{R}$ and the (field) phase shift $\Phi \in \mathbb{R}$. In general, $\mathfrak{T}$ can depend on numerous parameters, typically the signal frequency ν, the time t after an excitation of the object,

or the power P of the excitation. If we compare the transfer functions for two parameter sets $A = \{t_\mathrm{A}, P_\mathrm{A}, \ldots\}$ an $B = \{t_\mathrm{B}, P_\mathrm{B}, \ldots\}$, we define

$$\begin{aligned}\frac{\ln 10}{10}\Delta G(\nu, A, B) + i\Delta\Phi(\nu, A, B) &= \ln\left[\frac{\mathcal{E}_\mathrm{out}(\nu, B)}{\mathcal{E}_\mathrm{out}(\nu, A)}\right] = \ln\left[\frac{\mathfrak{T}_\mathrm{B}(\nu)\mathcal{E}_\mathrm{in}(\nu)}{\mathfrak{T}_\mathrm{A}(\nu)\mathcal{E}_\mathrm{in}(\nu)}\right] \\ &= \ln\left[\frac{G_\mathrm{B}(\nu)e^{i\Phi_\mathrm{B}(\nu)}}{G_\mathrm{A}(\nu)e^{i\Phi_\mathrm{A}(\nu)}}\right] = \ln\left[\frac{G_\mathrm{B}(\nu)}{G_\mathrm{A}(\nu)}\right] + i\left[\Phi_\mathrm{B}(\nu) - \Phi_\mathrm{A}(\nu)\right]\end{aligned} \tag{1.24}$$

with the differential gain $\Delta G \in \mathbb{R}$ and the phase difference $\Delta\Phi \in \mathbb{R}$. As the exact input field $\mathcal{E}_\mathrm{in}(\nu)$ is commonly unknown, the differential approach in eq. 1.24 is often the only quantitative experimental access.

Especially for semiconductor devices it is appropriate to replace 1.23 by a description that takes propagation into account. In this case we define analog to the Lambert–Beer law a

$$\mathcal{E}_\mathrm{out}(\nu, x) = \mathfrak{T}(\nu, x)\mathcal{E}_\mathrm{in}(\nu, 0) = e^{(g(\nu)+i\phi(\nu))x}\mathcal{E}_\mathrm{in}(\nu, 0) \tag{1.25}$$

with the gain coefficient g and the phase coefficient ϕ. For a device of length L this means $g = (\ln G)/L$ and $\phi = \Phi/L$. Equation 1.24 in this case becomes

$$\frac{\ln 10}{10}\Delta G + i\Delta\Phi = \left(\left[g_\mathrm{B} - g_\mathrm{A}\right] + i\left[\phi_\mathrm{B} - \phi_\mathrm{A}\right]\right)L \tag{1.26}$$

which means that this representation eliminates the effect of propagation and the measured value ΔG linearly corresponds to the material property $g_\mathrm{B} - g_\mathrm{A}$.

1.3.2. Frequency filters

In many cases a wide spectrum needs to be reduced to a narrow area of interest by electrical filtering. Perfect spectral cuttoffs cannot be realized, of course, since they require infinite temporal information. Based on resistors (R), coils (L), and capacitors (C), different configurations of RLC circuits can be used for a variety of analogue filter types. In many applications, analogue filters are replaced by digital ones nowadays, but the basic terms to describe filter properties are identical. The most frequently used terms, cutoff frequency and roll-off, can be derived from the example of a Butterworth filter.[22] This class of filters is designed to provide flat spectral gain in the pass band. The gain function is given by

$$\mathfrak{T}_n(\widehat{\nu}) = \left[\prod_{k=1}^{n}\left(i\frac{\widehat{\nu}}{\widehat{\nu}_\mathrm{cut}} - \exp\frac{i(2k+n-1)\pi}{2n}\right)\right]^{-1} \tag{1.27}$$

with cutoff frequency $\widehat{\nu}_\mathrm{cut}$ and the order n of the Butterworth filter.[23] For $n = 1$ this becomes

$$\mathfrak{T}_1(\widehat{\nu}) = \frac{1}{i\frac{\widehat{\nu}}{\widehat{\nu}_\mathrm{cut}} + 1} \tag{1.28}$$

At the cutoff frequency the power gain drops to $|\mathfrak{T}_1(\widehat{\nu}_\mathrm{cut})|^2 = 0.5 \approx -3\,\mathrm{dB}$ and is therefore often referred to as the 3 dB frequency. In a RLC filter the order n depicts the sum of numbers of coils and capacitors, respectively. Often filters of even order $n = 2m$ with m pairs of coil and capacitor are used. In this case the gain shows a roll-off for high frequencies, i.e. it decreases by $0.5^n \approx -6\,\mathrm{dB} \cdot m$ as the frequency doubles according to eq. (1.27). Therefore specifications like 6 dB/octave are often used to characterize filters. It is also common to denote a time constant $\tau_\mathrm{TC} \equiv \widehat{\nu}_\mathrm{cut}^{-1}$ to visualize the delay of a changing signal that comes with the cutting of the high frequencies. The actual filter settling time depends on the filter order (higher order means longer settling time) and exceeds the time constant roughly by a factor of 5 for a first order filter.

Digital low pass filter

A digital low–pass can be implemented in different ways. In the later used Zurich Instruments (ZI) HF2LI lock–in, an *exponential running average filter* is used that resembles the properties of eq. (1.28).[24] A data point x_n acquired with sampling time Δt is added to the previous average value $\bar{x}_{n-1}$

$$\bar{x}_n = \bar{x}_{n-1} \exp\left(-\frac{\Delta t}{\tau_{\mathrm{TC}}}\right) + x_n \left(1 - \exp\left(-\frac{\Delta t}{\tau_{\mathrm{TC}}}\right)\right). \tag{1.29}$$

This method is elegant as it only needs a single memory and mimics the Butterworth filter well. In section 7.3, however, we will discuss a case where this kind of filtering might pose an obstacle to the ultimate exploitation of the frequency range in the future.

2. Semiconductors

2.1. Carrier wavefunctions and their symmetry

Before we start to discuss the coupling of semiconductor systems, some fundamental terms should be reviewed. The basic statements of solid state physics are predominantly variations of the particle in a box problem (section 1.1.3) under certain restrictions.

2.1.1. Extended states

In extended crystals, the atoms form a periodic lattice. The periodicity puts a boundary condition to the wavefunctions of the electrons. The simple vacuum dispersion relation

$$E_{\mathrm{vac}}(\boldsymbol{k}) = \frac{\hbar^2}{2m_0}\boldsymbol{k}^2 \tag{2.1}$$

with wavevector $\boldsymbol{k}$ and electron rest mass m_0 is replaced by bands of allowed states. These states are distributed homogeneously in k-space. Of particular interest are the the lowest energy states of these bands, the so called *band edge*. At this energetic minimum, a Taylor expansion allows to appoximate the dispersion relation $E(\boldsymbol{k})$ by a parabola, which is again quite similar to eq. (2.1). In correspondence, one defines the *effective mass*

$$m^* = \hbar^2 \left(\frac{\partial^2 E}{\partial \boldsymbol{k}^2}\right)^{-1} \tag{2.2}$$

of a carrier in the crystal based on the band curvature in k-space. Based on the homogeneous distribution of states in the k-space and the band functions $E(\boldsymbol{k})$, one can calculate a density of states (DOS) $D(E)$. The DOS is an important factor that determines the probability of optical transitions.

Carriers occupy the low energy bands first up to the Fermi level, which is predominantly defined by the available number of carriers in the neutrally charged crystal. The occupied bands are called valence bands (VBs), the unoccupied bands of higher energy conduction bands (CBs). Materials are classified as *semiconductors* if there is an energetic *band gap* between VB and CB of up to several eV. Carrier transitions from CB to the VB correspond to photon energies from the infrared (IR) to the ultraviolet (UV) range. This makes semiconductors the ideal interface between optics and electronics.

To describe the carrier dynamics, it is useful to call occupied states in the CB "electrons" and unoccupied states in the VB "holes". The determination of states based on the particle in a box model and periodic potentials has neglected the charge of these particles. In analogy to the hydrogen atom, electrons and holes can form bound states that are called *excitons*. These excitons can be described as a new type of quasi–particle with a single wave function.[25]

2.1.2. Confined states and Dimensionality

The extension of a semiconductor can be confined in one or more dimensions. This has crucial impact on the DOS. For each of the three dimensions, the crystal can either be extended, with a

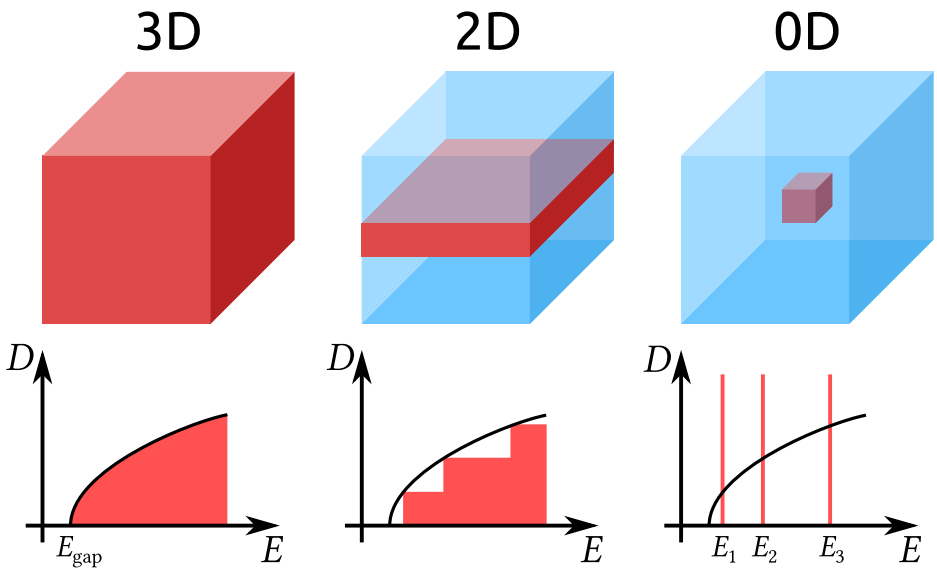

Figure 5: Density of states for the three confinement cases that will be important in the following.

continuuous DOS (section 2.1.1), or confined, with discrete energy levels (section 1.1.3). We call a crystal n-dimensional, if it is extended in n of theses three dimensions. Three different cases will occur in the following, they are illustrated in fig. 5: The three–dimensional (3D) or *bulk* material has a $D_{3D}(E) \propto \sqrt{E}$. The two–dimensional (2D) case is referred to as quantum well (QW) and has a stepwise increasing DOS. A semiconductor crystal with strong confinement in each direction, i.e. the zero–dimensional (0D) case, is called QD. It has a discrete DOS which qualifies it to be called an "artificial atom". QDs will be the primary subject in the following.

A epitaxially grown QD will not be spherical, but rather a truncated pyramid.[26] This is comparable to the case of a strong confinement in z direction and a moderate confinement in x and y direction, respectively. According to eq. (1.21), the energy contribution of the z confinement is large, while that of the xy plane confinement is smaller. Typically, this leads to an exciton ground state (GS) of the QD that is s-type in all direction. Above this GS, there are two states that are p-type in one of the planar directions. This state is therefore twofold degenerate and referred to as the first excited state (ES) of the QD.

2.1.3. Optical transitions

On a quantum mechanical level, the transition of carriers from one state to another upon optical excitation can be described by first order perturbation theory. The Hamiltonian of the system is split into a Hamiltonian $\widehat{H}_0$ of the unperturbed system, and a Hamiltonian $\widehat{H}_1$ that represents the interaction of the external field and the system. The calculation results in Fermi's Golden Rule

$$\Gamma_{\mathrm{fi}} = \frac{2\pi}{\hbar} D(E_{\mathrm{f}}) \left| \langle E_{\mathrm{f}} | \, \widehat{H}_1 \, | E_{\mathrm{i}} \rangle \right|^2 \tag{2.3}$$

that describes the transition rate Γ_{fi} from an initial state $|E_{\mathrm{i}}\rangle$ to a final state $|E_{\mathrm{f}}\rangle$. This description is actually not limited to optical transition, but describes any transition triggered by an external perturbation.

In eq. (2.3), two factors contribute to the transition rate: Firstly, there is the DOS $D(E_{\mathrm{f}})$—without a final state, there is no transition. Secondly, the transition rate is determined by the integral

$\langle E_\mathrm{f}| \, \widehat{H}_1 \, |E_\mathrm{i}\rangle$. Quantum confinement is an important technique to increase the overlap of the wavefunctions and to thereby maximize the integral. Additionally, this factor results in selection rules depending on the respective symmetry of initial and final state under the particular perturbation. Some transitions might be (dipole) forbidden. However, if the ideal system is modified, for instance by the contribution of Coulomb interaction or by complicated potential landscapes, some selection rules might be lifted. An exact theoretical description is extremely demanding.

2.2. Semiconductor classes

2.2.1. Epitaxially grown III-V Semiconductors

III-V semiconductors are basically composed of group III elements—aluminum (Al), gallium (Ga), or indium (In)—and group V elements—nitrogen (N), phosphorus (P), arsenic (As), or antimony (Sb). Their bandgap energies span almost the entire semiconducting range, from InAs at 0.35 eV to AlN at 6.2 eV. By mixing of elements, for instance in InGaAs, the bandgap energy can be tuned. III-V semiconductors are usually epitaxially grown. The standard techniques are molecular beam epitaxy (MBE) and, more industrial, metalorganic vapor–phase epitaxy (MOVPE). In both cases, new material is deposited on a substrate layer. The tunability of the band gap together with the elaborate fabrication techniques make III-V semiconductors an important platform for a wide range of applications.

Epitaxial growth requires that the lattice constant of the deposited material matches the lattice constant of the substrate within a certain tolerance. A mismatch induces strain and thereby increases the surface energy. The formation of islands can minimize the surface energy and be therefore favorable. Depending on the surface energies of the materials and the lattice mismatch, three different growth modes occur: The layer–by–layer growth (Frank–van der Merwe growth), the formation of islands (Volmer–Weber growth), and the formation of islands on top of a single layer (Stranski-Krastanow (SK) growth).[26] This single layer is also called wetting layer (WL). For example, InAs with a lattice constant of 0.606 nm and GaAs with 0.565 nm at room temperature have a lattice mismatch of 7.3 %. The formation of SK QDs is a self–organized process. This results in QDs of varying size and therefore varying transition energies. This energy distribution is referred to as the *inhomogeneous broadening* of the QD ensemble. For typical QD ensembles, the inhomogeneous broadening of the GS can be approximated by a Gaussian with a FWHM σ_G of 10 eV to 100 eV.[26] A small inhomogeneous broadening is often desired to increase the DOS for a desired wavelength.

Binding energies of excitons and exciton complexes in InAs/GaAs and its nanostructures are in the range of $< 10\,\mathrm{meV}$.[27–29] Compared to the roomtemperature $k_\mathrm{B}300\,\mathrm{K} \approx 25\,\mathrm{meV}$, these binding energies are usually negligible and the quasiparticles therefore unstable. In our nanostructures, the confinement energy is the dominant contribution to the exciton energy levels.

2.2.2. Colloidal PbS/CdS quantum dots

Although we are mostly dealing with III-V semiconductor, we will investigate colloidal PbS/CdS core-shell[30,31] QDs in a side–project. Unlike the InAs QDs, the PbS/CdS QDs are created in a wet–chemical process.[32] These QDs are also interesting for photonics and opto–electronics applications as their emission wavelength is tunable from 900 nm to 2000 nm, covering all important telecommunication windows[33]. In order for systems based on colloidal QDs to compete with the established technology, e.g. In(Ga)As structures, data rates are required to lie in the Gbit/s range, corresponding to one bit per 1 ns. An important aspect that needs consideration is the long lifetime of the

exciton GS in colloidal QDs, exceeding this time by up to three orders of magnitude.[33]Fast data manipulation mechanisms therefore needs to be based on an efficient nonlinear process[34,35] or the GS lifetime has to be dramatically reduced. For all–optical signal conversion, the relevant processes are in particular fast multi–exciton scattering events. A competing process is efficient broadband intraband absorption, which has been observed in pump-probe (PP) experiments[36]. Recently, it has been demonstrated that the effect of intra- and interband processes cancels at a specific wavelength, making ultrafast switching operations based on nonlinear interaction possible.[35]

During the development process, spin–coating is a suitable fabrication technique for an easy combination of waveguide structures and optically active colloidal QDs. One drawback of spin–coating is the comparatively small overlap between the QD emission mode and the waveguide mode.[4] The QDs are simply deposited on top of a chip with silicon nitride waveguides, while in more sophisticated techniques an integration of the QDs into the waveguide is possible, which increases the overlap. Silicon and silicon nitride (Si_3N_4) are important platforms in nanophotonics, with the perspective of chip-sized devices based on a CMOS-compatible fabrication technology.[37] Si_3N_4 can be manufactured into high quality low-loss waveguides and resonators.[38–40] Additionally, a range of hybrid photonic devices based on silicon nitride structures has been demonstrated.[41–46] In contrast to silicon, the material does not display large intrinsic nonlinearities or a substantial free carrier absorption,[47] and therefore allows us to observe the nonlinear response of the QDs without waveguide–induced background.

The technical challenges that we will address in section 6.4 are in particular the low mode overlap and the fact that most studies on the ultrafast dynamics of similar samples have been performed using amplified laser systems with kHz repetition rate. For the high repetition rates we use, tending towards 100 MHz and thereby towards telecom applications, the long GS lifetime will have a distinct effect on the observed effects.

2.2.3. Transitionmetal-Dichalcogenides

The material class of transitionmetal-dichalcogenides (TMDs) has attracted tremendous interest of the semiconductor community since the crossover from an indirect to a direct bandgap in the monolayer limit was demonstrated.[48] TMDs have a chemical composition of the type MX_2 with a transition metal ion M—molybdenum (Mo) or tungsten (W)—and two chalcogen ions X—sulfur (S), selenium (Se), or tellurium (Te)—that form 2D layers. The bulk material is composed of stacked layers held together by van der Waals interactions. Especially the compounds of Mo/W and S/Se have been investigated by many groups, as their lowest exciton energies are in the range of 650 nm to 850 nm, which is addressable by the popular Ti:sapphire laser. But also the investigation of $MoTe_2$ with transition energies in the near infrared (NIR) has been intensified recently.[16,49]

In TMDs, very large binding energies have been observed. The exciton binding energy can be larger than 300 meV, which is roughly two orders of magnitude more than in GaAs.[50,51] Also the trion binding energy is in the range of 30 meV.[52,53] These high binding energies make these quasiparticles interesting for opto–electronic applications at room temperature. More than that, indirect excitons in TMD heterostructures are discussed in the literature,[54] which is very similar to the discussion of crossed excitons (CEs) later on (section 2.3.4 and chapters 10 and 11.

Simple monolayer TMD samples are prepared either by exfoliation or by chemical vapor deposition. The optical excitation geometry is usually perpendicular to the TMD monolayer plane. Although TMD monolayers absorb about 10 % of the incident cw radiation,[55] the signals in the non–linear experiments we perform are still on the level of 10^{-4}. This made a modification of our pump-probe (PP) detection scheme necessary that will be discussed in detail in section 6.2.

Parameter	GaAs[57]	InAs[58]
$E^{(0)}$ [eV]	1.517	0.415
α [μeV K^{-1}]	550	276
β [K]	225	83

Table 1: Varshni parameters for GaAs and InAs.

2.3. Coupled semiconductor systems

2.3.1. Heterostructures and diodes

Heterostructures are a spatial combination of different semiconductors that are used to tailor a spatial potential landscape. In epitaxially grown III-V semiconductors, this is achieved by a modification of the composition of the deposited material, for instance the ratio of In and Ga in InGaAs crystals.[26] But also TMDs are used to create heterostructures by stacking monolayers of different types.[56] Additional dopands can be used to shift the Fermi level inside the band gap either towards the VB (p-doping) or the CB (n-doping). The creation of heterostructures is a key to realize new technical applications. Besides transistors, the most important basic type of such heterostructures are pin-diodes. These diodes are composed of an intrinsic (undoped, i) layer sandwiched between a p- and an n-doped bulk material. In the contact region, a band bending due to carrier redistribution equilibrates the Fermi level. The doped areas allow for carrier transport. Under forward bias ($+$ at p, $-$ at n), carriers can be injected into the i region. Under reverse bias ($-$ at p, $+$ at n), carriers are extracted.

Electro–optical devices are often variations of pin-diodes with an optical active material in the i-region. While there are also surface emitting devices (emitting in growth direction), we will deal with edge emitters (emitting perpendicular to the growth direction). Semiconductor lasers, light emitting diodes (LEDs), semiconductor optical amplifiers (SOAs), detectors, and solar–cells are in principle variations of the same device—with totally different optimization demands, of course, and emission will be only observed for direct band gaps. On one hand, an unbiased device acts as a solar–cell, while detectors have usually a high reverse bias to extract newly generated carriers efficiently from the active region. Under moderate forward bias, on the other hand, they start to spontaneously emit photons. For higher forward bias above the lasing threshold, edge emitters start lasing if no precautions are taken. To suppress lasing, SOAs have anti–reflection coated waveguide facets. In the amplifying regime, the emission is referred to as amplified spontaneous emission (ASE).

Electrical carrier injection always comes along with heat generation which affects the band gap energy. The temperature dependence is well described by the empirical Varshni formula

$$E(T) = E^{(0)} - \alpha \frac{T^2}{T + \beta} \tag{2.4}$$

with phenomenological parameters α and β according to table 1 for the important cases of GaAs and InAs.

2.3.2. The dot-in-a-well system

For the purpose of data transmission, the optical emission needs to fit the telecom windows around wavelengths of 1.3 μm (O-band) and 1.55 μm (C-band). These windows provide minimal absorption in optical fibers that allows for long range optical data transfer. Tuning the emission wavelength of

InAs QD to these transmission windows was a long development process.[26,59] Besides the emission wavelength, also the efficient carrier injection into the QDs was a development goal.[59].

Investigating a single QD of the dot–in–a–well (DWELL) ensemble is quite challenging. In contrast to non–overgrown SK QDs, it is more difficult to identify a single dot in the ensemble.[60] There are also some other issues that need to be considered: On one hand, the optical excitation perpendicular to the QD plain differs from that in–plane. On the other hand, the potential landscape of the free–standing DWELL differs from that in the active region of the diode. The resulting states might be affected by the modified environment.

2.3.3. Rate equation modeling

Rate equations are a simple yet powerful method to describe basic carrier kinetics in coupled systems. Rate equations represent in a simplified picture what Fermi's Golden Rule (2.3) tries to explain microscopically: There is an initial state N_1, a final state N_2, and transition rates Γ_{ij} that represents transitions from N_j to N_i. The nature of the state is not important here, it acts as a "bin" with population N_i. For these two states, the rate equation system is

$$\dot{N}_1 = \Gamma_{11} N_1 + \Gamma_{21} N_2 \tag{2.5a}$$

$$\dot{N}_2 = \Gamma_{12} N_1 + \Gamma_{22} N_2. \tag{2.5b}$$

The rates Γ_{ii} can be interpreted as decay (or feeding) rates coupling the system to its environment. For more states, a matrix notation

$$\dot{\boldsymbol{N}} = \Gamma \cdot \boldsymbol{N} \tag{2.6}$$

is more appropriate. Just like eq. (2.3), the transition matrix Γ might depend on the number of available final states. Especially in fermionic systems, where Pauli blocking needs to be considered, there will be a population–dependent transition rate $\Gamma(\boldsymbol{N})$. This makes eq. (2.6) a nonlinear differential equation (DEQ) which requires a numerical solution. In section 10.2.1, however, we will even in the case of electrons discuss a linear rate equation model. In this case, for a static Γ, eq. (2.6) can be solved by the determination of the eigenvalue and eigenvectors of Γ. The eigenvalues $-\tau_i^{-1}$ represent decay rates with the corresponding eigenvector

$$\boldsymbol{N}_i \exp\left(-\frac{t}{\tau_i}\right). \tag{2.7}$$

The numerical determination of eigenvalues and eigenvectors and the transformation of the problem to the according basis is much faster than the solution of the DEQ using methods like Runge–Kutta. This allowed us to perform the calculations presented in section 10.2.1 on a standard desktop PC.

In the extended 2D systems of QWs, we also will observe Brownian motion, i.e. diffusive processes. These are described by a second order DEQ

$$\partial_t \varrho(x,t) = D \partial_x^2 \varrho(x,t) \tag{2.8}$$

for the density ϱ of particles at a distance x from the origin with a diffusion constant D. This DEQ has the solution

$$\varrho(x,t) = \frac{N}{\sqrt{4\pi D t}} \exp\left(-\frac{x^2}{4Dt}\right) \tag{2.9}$$

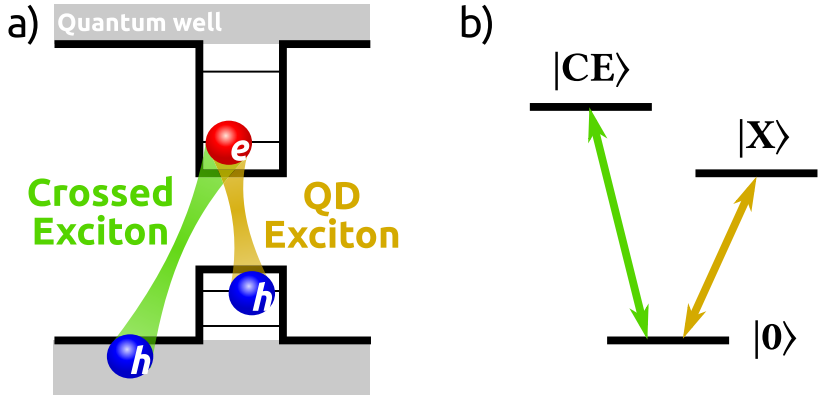

Figure 6: Illustration of Crossed Excitons. (a) An electron in the QD can either form a QD exciton together with a hole that is also confined in the QD, or it can form a CE together with a hole in the 2D continuum of the QW. (b) As both, QD exciton and CE state, share one carrier, there is an intrinsic coherent coupling between these states that form a V system together with the crystal ground state $|0\rangle$.

for N particles in the system. In our case, the case $x = 0$ will be of particular interest, because this will represent the QD in section 10.2.1. The density at this point is $\varrho(x = 0, t) \propto 1/\sqrt{t}$ with a "decay constant"

$$\tau(t) = -\frac{\varrho(x = 0, t)}{\partial_t \varrho(x = 0, t)} \propto t \tag{2.10}$$

which is no constant, of course, but a linearly increasing value where $t = 0$ represents the δ-like distribution according to eq. (2.9). This linear rise of the decay time characterizes the Brownian motion in contrast to the first order linear DEQ characterized by eigenvectors according to eq. (2.7).

A representation of the Brownian motion in terms of rate equations requires a discretization of the space. Every bin of the rate equation model represents a certain volume in space. A good approximation of the diffusion behavior can be achieved by a random walk, which is characterized by an equal probability to transit in any direction. Of course, bin sizes and bin geometry need to be considered. An example will also be given in section 10.2.1.

2.3.4. Crossed Excitons

Excitons are bound states of electrons and holes, they are described analog to the hydrogen atom.[61] The necessary Coulomb attraction will also be present if one carrier occupies a bound state (bound with respect to the potential landscape), the other one a continuum state. The formation of a hydrogen–like state is not forbidden by the different dimensionality of the states. In part III we will find evidence for the existence of such states in the systems we investigate. Similar observations can be found in the literature, and we decided to use the term crossed exciton (CE) in Ref. 2 and derived it from the argumentation in Refs. 62, 63.

To evaluate the relevance of these anticipated states, several typical assumptions about excitons need to be reviewed. First of all, it is necessary to leave the picture of photoluminescence (PL) experiments. In these experiments, carriers are created with high excess energy and emission is predominantly detected from the long–lived GS. Excitons need to be formed first and their binding energy needs to exceed $k_\mathrm{B}T$ to be detected in PL. In III-V semiconductors, this requires cryogenic temperatures. In our experiments, however, we will deal with distinct non–equilibrium states. If these states are occupied directly by optical excitation or from classical QD excitons, they might

play a role at least on the ultrafast timescale. The optical excitability is the second aspect to be reviewed: Within QDs, some transitions are forbidden by selection rules due to the wavefunction symmetry. Such selection rules might be lifted under the formation of bound states from carriers of different dimensionality and under the influence of Coulomb attraction. The third aspect is the interaction with the surrounding environment. In the vacuum, a hydrogen atom either exists as a bound state or it does not. In a semiconductor, scattering processes might keep a dissociated exciton together, as the movement in the environment is rather diffusive than ballistic, as we will discuss in section 10.2. Also effects like Anderson localization might come into play.

The theoretical handling of these states is challenging. Our observations will here stay on a phenomenological level that is supposed to motivate a deeper investigation of the theory of CEs.

3. The theory of light–matter interaction

The scope of the theoretical description of light–matter interaction is set by the methods applied and the samples investigated. While many fundamental properties can be derived in a fully classical theory of light as well as matter, the nature of QDs enforces a quantum–mechanical description of matter. Such a semi–classical description, however, will be sufficient, as the experimental results presented in this thesis are obtained in the many–photon limit. Although the term "photon" will be widely used in a phenomenological way and the heterodyne setup has been used to perform experiments in the few–photon limit[9], a detailed description of the quantization of the light will be omitted.

The very fundamentals for the description of light–matter interaction can be found in Maxwell's equations:

$$\nabla \cdot \boldsymbol{\mathcal{D}}(\boldsymbol{r},t) = \rho(\boldsymbol{r},t) \equiv 0 \tag{3.1a}$$

$$\nabla \cdot \boldsymbol{\mathcal{B}}(\boldsymbol{r},t) = 0 \tag{3.1b}$$

$$\nabla \times \boldsymbol{\mathcal{E}}(\boldsymbol{r},t) = -\partial_t \boldsymbol{\mathcal{B}}(\boldsymbol{r},t) \tag{3.1c}$$

$$\nabla \times \boldsymbol{\mathcal{H}}(\boldsymbol{r},t) = \boldsymbol{j}(\boldsymbol{r},t) + \partial_t \boldsymbol{\mathcal{D}}(\boldsymbol{r},t) \equiv \partial_t \boldsymbol{\mathcal{D}}(\boldsymbol{r},t)\,. \tag{3.1d}$$

Here it is already indicated by $\equiv$ that for our description of dielectric media the free charge–carrier density ρ and the free current density j can be widely neglected. The interesting material properties are contained in the electric displacement field $\boldsymbol{\mathcal{D}}$ and the magnetizing field $\boldsymbol{\mathcal{H}}$:

$$\boldsymbol{\mathcal{D}}(\boldsymbol{r},t) = \varepsilon_0 \boldsymbol{\mathcal{E}}(\boldsymbol{r},t) + \boldsymbol{\mathcal{P}}(\boldsymbol{r},t) \tag{3.2a}$$

$$\boldsymbol{\mathcal{H}}(\boldsymbol{r},t) = \frac{1}{\mu_0}\boldsymbol{\mathcal{B}}(\boldsymbol{r},t) - \boldsymbol{\mathcal{M}}(\boldsymbol{r},t) \equiv \frac{1}{\mu_0}\boldsymbol{\mathcal{B}}(\boldsymbol{r},t)\,. \tag{3.2b}$$

From eqs. (3.1) and (3.2) one can derive the wave equation

$$\Delta \boldsymbol{\mathcal{E}}(\boldsymbol{r},t) - \frac{1}{c_0^2}\partial_t^2 \boldsymbol{\mathcal{E}}(\boldsymbol{r},t) = \mu_0 \partial_t^2 \boldsymbol{\mathcal{P}}(\boldsymbol{r},t)\,. \tag{3.3}$$

3.1. Matter acting on light

It will be sufficient from now on to discuss the respective fields in one dimension. As the investigated semiconductors can be considered non–magnetizable ($\mathcal{M}(\boldsymbol{r},t) \equiv 0$), the description of light–matter interaction shrinks down to the description of the relation of the electric field $\mathcal{E}$ and the polarization $\mathcal{P}$. This relation is given by the electric susceptibility $\chi(\mathcal{E})$ that can be written as a Taylor expansion

$$\mathcal{P} = \varepsilon_0 \left(\chi^{(1)}\mathcal{E} + \chi^{(2)}\mathcal{E}\mathcal{E} + \chi^{(3)}\mathcal{E}\mathcal{E}\mathcal{E} + \ldots\right). \tag{3.4}$$

The linear term $\chi^{(1)}$ does not need a detailed discussion. Also the $\chi^{(2)}$ contribution is of minor interest, firstly, because $\chi^{(2)}$ is suppressed in general by the crystal symmetry, and secondly, because $\chi^{(2)}$-effects are not investigated. The $\chi^{(3)}$-term, however, will be of major importance. We will here focus on four-wave mixing (FWM) as the most important non–linear effect in the following.

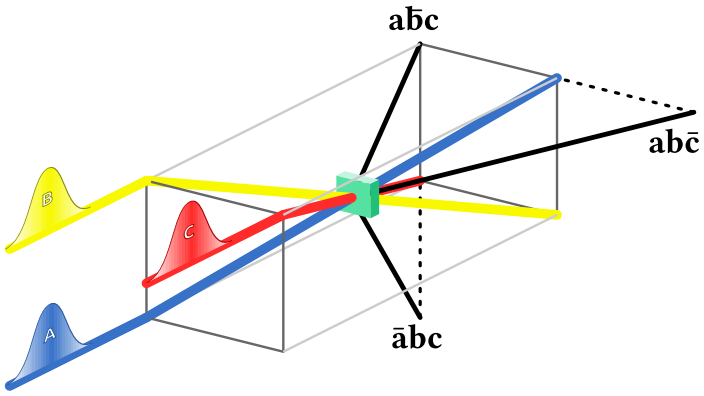

Figure 7: FWM in the box geometry. The original beams and the mixing bands can be filtered spatially. Only the relevant mixing cases that incorporate exactly one conjugate field are shown.

3.1.1. Four wave mixing

FWM is very closely related to the four pulse scheme (4PS) that we will use to describe the experiment in chapter 4. Three incident waves (A, B, and C) mix according to the $\chi^{(3)}$-nonlinearity of the medium:

$$\begin{aligned}\mathcal{P}_{\mathrm{FWM}} = \varepsilon_0\chi^{(3)} &\left(\mathcal{E}_{0,\mathrm{a}}e^{i\boldsymbol{k}_\mathrm{a}\cdot\boldsymbol{r}+i\omega_\mathrm{a}t} + \mathcal{E}^*_{0,\mathrm{a}}e^{-i\boldsymbol{k}_\mathrm{a}\cdot\boldsymbol{r}-i\omega_\mathrm{a}t}\right)\left(\mathcal{E}_{0,\mathrm{b}}e^{i\boldsymbol{k}_\mathrm{b}\cdot\boldsymbol{r}+i\omega_\mathrm{b}t} + \mathcal{E}^*_{0,\mathrm{b}}e^{-i\boldsymbol{k}_\mathrm{b}\cdot\boldsymbol{r}-i\omega_\mathrm{b}t}\right)\\ &\left(\mathcal{E}_{0,\mathrm{c}}e^{i\boldsymbol{k}_\mathrm{c}\cdot\boldsymbol{r}+i\omega_\mathrm{c}t} + \mathcal{E}^*_{0,\mathrm{c}}e^{-i\boldsymbol{k}_\mathrm{c}\cdot\boldsymbol{r}-i\omega_\mathrm{c}t}\right).\end{aligned} \tag{3.5}$$

An illustration of a FWM experiment in the *box geometry* is given in fig. 7. There are eight different contributions to P_{FWM} which result in different fields obeying energy and momentum conservation. These resulting fields will be very important later on. To distinguish them, we will use the notation

$$\mathcal{E}_{\mathrm{a\bar{b}c}}(t) \propto \mathcal{E}_\mathrm{a}(t)\mathcal{E}^*_\mathrm{b}(t)\mathcal{E}_\mathrm{c}(t) = \mathcal{E}_{0,\mathrm{a}}\mathcal{E}^*_{0,\mathrm{b}}\mathcal{E}_{0,\mathrm{c}}e^{i(\boldsymbol{k}_\mathrm{a}-\boldsymbol{k}_\mathrm{b}+\boldsymbol{k}_\mathrm{c})\boldsymbol{r}+i(\omega_\mathrm{a}-\omega_\mathrm{b}+\omega_\mathrm{c})t}, \tag{3.6}$$

so $\mathcal{E}_{\mathrm{a\bar{b}c}}$ originates from pulses A, B, and C. The bar on top of the "b" indicates that the complex conjugate wave has been used. Not all possible combinations are important to us, because all of our incident pulses will be in the NIR range and the resulting field needs to be as well, in order to be observed. For example, $\mathcal{E}_{\mathrm{abc}}$ will oscillate at a frequency of $\omega_\mathrm{a}+\omega_\mathrm{b}+\omega_\mathrm{c}$, which is out of our spectral range. Relevant for us are all combinations that incorporate exactly one conjugate field. These combinations are also displayed in fig. 7.

3.1.2. Frequency conversion

Every gain medium is limited to a certain frequency range. Although there are established gain media from the Mid-IR to the UV range[64] and free–electron lasers provide almost arbitrarily tunable coherent radiation, a typical optics lab needs to rely on frequency conversion to generate desired frequencies from standard sources. In the visible (VIS) and UV the generation of higher harmonics is a standard approach. However, the discussion of available methods is restricted to the ones applied later on.

Ti:sapphire laser and parametric down–conversion

For 30 years now the Ti:sapphire laser has been the dominating solid state laser and has revolutionized non–linear optics. Typical mode–locked Ti:sapphire lasers are built as free–space cavities

with a repetition rate around 80 MHz. The emission is centered around 800 nm and is tunable from 600 nm to 1000 nm. For the investigation of transitions with longer wavelengths, an optical parametric oscillator (OPO) can be used for the frequency conversion. The OPO is basically a resonator (with a length adjusted to the laser resonator length) with a non–linear crystal inside. In the non–linear crystal, the pump photons of frequency ν_p are split into two photons of lower energy in a parameteric downconversion process. The higher frequency photon $\nu_\mathrm{s}$is referred to as "signal", the lower one at ν_i as "idler", with $\nu_\mathrm{s} + \nu_\mathrm{i} = \nu_\mathrm{p}$. In one series of experiments (chapter 9) we will use the signal photons created by an OPO.

Supercontinuum generation

The frequency range covered by the OPO is restricted by the pump pulse bandwidth due to the defined photon–breakup in the phase–matched crystal. In highly non–linear devices that do not fulfill such conditions, higher order mixing processes can lead to the generation of a so called supercontinuum. The supercontinuum can cover more than one octave and is quasi–continuous, but is still based on the resonator modes. The original laser modes have frequencies

$$\nu_n = \widehat{\nu}_\mathrm{off} + n \cdot \widehat{\nu}_\mathrm{rep} \tag{3.7}$$

with an offset $\widehat{\nu}_\mathrm{off}$ and an equal mode spacing of $\widehat{\nu}_\mathrm{rep}$. The generation of the supercontinuum can be considered as a cascaded FWM process, and like in the FWM case only such processes are relevant that incorporate one conjugate field. This, however, results in the cancellation of two of the $\widehat{\nu}_\mathrm{off}$ and thereby forces all newly generated modes to also fulfill eq. (3.7).

3.2. Light acting on matter

For the understanding of the mechanisms of light–matter interaction, it is necessary to relate the macroscopic parameters like χ to microscopic processes on the level of single or few charge carriers. In a first step, the oscillating light field is treated as an external and stiff boundary condition. It is not modified by its action on the polarized matter.

3.2.1. The Hertzian dipole

In classical physics, a microscopic explanation of the optical susceptibility χ is given by the Hertzian dipole. We consider a single electron of charge e and mass m_0. A displacement r of this electron causes a proportional restoring force, so the electron movement under the influence of the external field is that of a driven damped harmonic oscillator with the natural frequency ω_0. The inhomoegenous differential equation is

$$\ddot{r} + 2\gamma\dot{r} + \omega_0^2 r = \frac{q}{m_0}\mathcal{E}_0 e^{-i\omega t} \tag{3.8}$$

and its homogeneous solution is

$$r_\mathrm{hom}(t) = Ae^{(-\gamma + i\omega_0)t} + c.c. \tag{3.9}$$

under the assumption that $\gamma \ll \omega_0$, which means that the reduction of the carrier frequency due to the damping is neglected. Also the inhomogeneous solution is easily found:

$$r_\mathrm{inh}(t) = -\frac{1}{\left(\omega^2 - \omega_0^2\right) + 2i\omega\gamma}\left(\frac{q}{m_0}\mathcal{E}_0 e^{-i\omega t}\right). \tag{3.10}$$

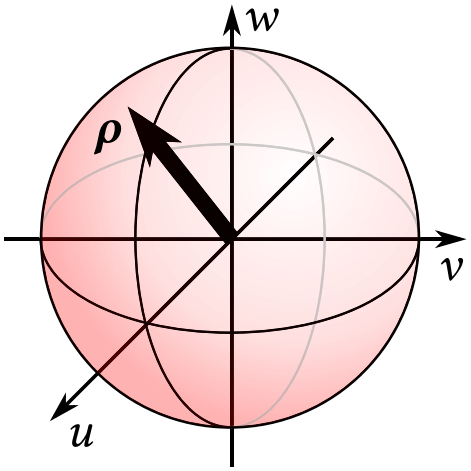

Figure 8: The Bloch sphere and the Bloch vector $\boldsymbol{\rho}$.

By applying the near–resonant approximation $\omega^2 - \omega_0^2 \approx 2\omega_0(\omega - \omega_0)$, this solution can be written in the more familiar form

$$r_{\mathrm{inh}}(t) \approx -\frac{1}{2\omega_0}\left(\frac{\omega-\omega_0}{(\omega-\omega_0)^2+\gamma^2} - i\cdot\frac{\gamma}{(\omega-\omega_0)^2+\gamma^2}\right)\left(\frac{q}{m_0}\mathcal{E}_0 e^{-i\omega t}\right) \tag{3.11}$$

where the imaginary part of $r_{\mathrm{inh}}(t)$ has the shape of a Lorentzian. The FWHM of this function is 2γ. As this is a property of the single oscillator, it is referred to as the *homogeneous linewidth* in contrast to the inhomogeneous broadening, which is an ensemble property. For the interpretation of two–dimensional spectra, the phase of the response function will be of particular interest later on, so we calculate it from eq. (3.11) and find

$$\varphi(\omega) = \arctan\left(\frac{-\gamma}{\omega-\omega_0}\right). \tag{3.12}$$

This describes the typical behavior of a driven harmonic oscillator: For $\omega \to 0$, we find in–phase oscillation ($\varphi \to 0$), while counter–phase oscillation ($\varphi \to \pi$) appears for $\omega \gg \omega_0$. At the resonance there is a rapid phase change described by the derivative

$$\frac{\mathrm{d}}{\mathrm{d}\omega}\varphi(\omega) = \frac{1}{1+\left(\frac{-\gamma}{\omega-\omega_0}\right)^2}\cdot\frac{\gamma}{(\omega-\omega_0)^2} = \frac{\gamma}{(\omega-\omega_0)^2+\gamma^2} \Rightarrow \frac{\mathrm{d}}{\mathrm{d}\omega}\varphi(\omega_0) = \frac{1}{\gamma}, \tag{3.13}$$

so the phase slope at the resonance can be used to directly derive γ.

3.2.2. Optical Bloch equations

The classical description has revealed the fundamental mechanism that mediates the energy transfer from one oscillator (the light field) to another (the dipole). It was also possible to derive the spectral lineshape from the fact of a finite lifetime. But of course we know today that in the microcopic world we have to deal with quantized energy. Equations like eq. (3.10) that predict a linear amplitude response to an $\mathcal{E}_0$ increasing towards infinity must find their limitations in a quantum world.

The quantum nature of matter must be taken into account, while the oscillatory behavior of the light field can be further described in the previous classical way. In this semi–classical approach,

the Hamiltonian is composed of an unperturbed term which represents the energy stored in the two level system (2LS) of eigenfrequency ω_0 and an interaction term. The temporal evolution of the system is determined by the Schrödinger equation. An analysis yields the optical Bloch equations[25,65]

$$\dot{u} = (\omega - \omega_0)\, v, \tag{3.14a}$$

$$\dot{v} = -(\omega - \omega_0)u + \Omega w, \tag{3.14b}$$

$$\dot{w} = -\Omega v \tag{3.14c}$$

for an oscillatory electric field $\mathcal{E}(t) = \mathcal{E}_0 \exp(i\omega t)$ of frequency ω in the rotating wave approximation (RWA). The coupling to the electric field is given by the *Rabi frequency*

$$\Omega = \frac{d\mathcal{E}_0}{\hbar}. \tag{3.15}$$

The pseudospin vector $\boldsymbol{\rho} = (u, v, w)^T$ is called the Bloch vector with $|\boldsymbol{\rho}| \equiv 1$ for an isolated 2LS. Its components u and v are the dispersive and absorptive components of the dipole moment, respectively, while the component w is the inversion. The constant length of the Bloch vector defines the Bloch sphere that is illustrated in fig. 8. It is important to have in mind that the Bloch vector is defined under the RWA in a rotating frame according to the respective light frequency. If the external field amplitude is reduced to zero, the temporal evolution is governed by the detuning $\omega - \omega_0$. In the resonant case $\omega = \omega_0$, the Bloch vector would be static.

A fundamental property of the dynamics governed by eq. (3.14) are Rabi oscillations. Temporal derivation of eq. (3.14b) and application of eqs. (3.14a) and (3.14c) yields

$$\ddot{v} = -\left((\omega - \omega_0)^2 + \Omega^2\right) v \tag{3.16}$$

which is the DEQ of a harmonic oscillation. For $\boldsymbol{\rho}(t = 0) = (-1, 0, 0)^T$ and under the condition $|\boldsymbol{\rho}| \equiv 1$, this results in

$$w(t) = -\frac{(\omega - \omega_0)^2 + \Omega^2 \cos\left(\sqrt{(\omega - \omega_0)^2 + \Omega^2}t\right)}{(\omega - \omega_0)^2 + \Omega^2}. \tag{3.17}$$

In the resonant case, the inversion oscillates between -1 and 1 at a frequency of Ω. With detuning, the amplitude of the oscillation is reduced and the frequency increased to $\sqrt{(\omega - \omega_0)^2 + \Omega^2}$.

For the problems discussed in the following, we will use an average Bloch vector to describe the state on an ensemble, with a Bloch vector length of $|\boldsymbol{\rho}| \leq 1$. In the real world, the coupling to the environment will also cause a polarization decay as well as an inversion decay. These decays are introduced phenomenologically to eq. (3.14) by decay constants:

$$\dot{u} = (\omega - \omega_0)\, v - \frac{u}{T_2}, \tag{3.18a}$$

$$\dot{v} = -(\omega - \omega_0)u - \frac{v}{T_2} + \Omega w, \tag{3.18b}$$

$$\dot{w} = -\Omega v - \frac{w + 1}{T_1}. \tag{3.18c}$$

These decay constant T_1 and T_2 will be crucial for the interpretation of our experiments. T_1 describes the decay of the inversion, it represents the lifetime of a population. The decay of the system polarization, on the other hand, is described by T_2. This process is referred to as *dephasing*.

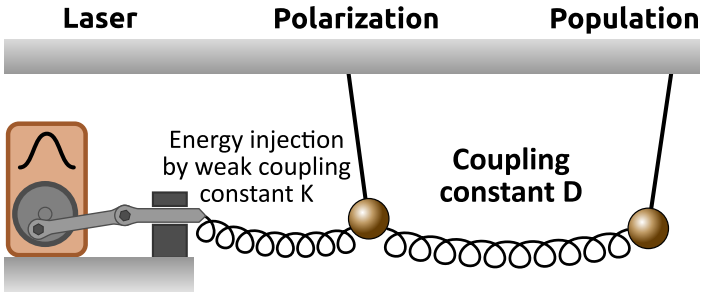

Figure 9: Illustration of a mechanical analog for the modification of a propagating light field. The initial field from the laser is fed into the coupled pendula system by a weak coupling constant. The coupled pendula exchange energy analog to the mutual energy exchange of light and matter during Rabi oscillations. Similarly published in Ref. 1.

3.3. Light interacting with matter

3.3.1. Maxwell–Bloch equations

The Maxwell–Bloch approach is quite exactly what its name tells us: a combination of the Maxwell equations (eq. (3.1)) and the Bloch equation (eq. (3.18)).[66,67] While the Bloch equations determine the inversion and polarization dynamics under the external perturbation, the Maxwell equations are used to calculate the feedback of the polarization that modifies the electric field. Additionally, a system environment can be modeled in the simple form of rate equations (section 2.3.3). Our colleagues Kathy Lüdge, Julian Korn, and Benjamin Lingnau used a full model like this to calculate the effect of Rabi oscillations induced by a laser pulse on this pulse itself:

$$\partial_t p_m^j = -i\Delta\omega_m^j p_m^j - i\frac{\Omega}{2}\left(\rho_{\mathrm{e},m}^j + \rho_{\mathrm{h},m}^j - 1\right) - \frac{1}{T_2}p_m^j \tag{3.19a}$$

$$\partial_t \rho_{b,m}^j = -\mathrm{Im}\left[\Omega\, {p_m^j}^*\right] - W_m \rho_{\mathrm{e},m}^j \rho_{\mathrm{h},m} + \partial_t \rho_{b,m}^j\Big|_{\mathrm{col}} \tag{3.19b}$$

$$\partial_t w_b = \frac{J}{e_0} - B^S w_{\mathrm{e}} w_{\mathrm{h}} - 2N^{\mathrm{QD}} \sum_{j,m} v_m f(j)\, \partial_t \rho_{b,m}^j\Big|_{\mathrm{col}} \tag{3.19c}$$

$$\left(\partial_z + \frac{1}{v_{\mathrm{g}}}\partial_t\right) E(z,t) = \frac{1}{v_{\mathrm{g}}}\frac{i\omega\gamma}{2\varepsilon_{\mathrm{bg}}\varepsilon_0} P(z,t). \tag{3.19d}$$

These equations are taken exactly from Ref. 1 and do not follow the nomenclature of this thesis, of course. A brief discussion is worthwhile, because this equation system merges the numerical approaches discussed so far. The first line, eq. (3.19a), describes the polarization. It is a complex entity that represents both, u and v, in the form of $p \equiv u + iv$, with indices j representing the QD subensemble and $m \in \{\mathrm{GS}, \mathrm{ES}\}$ accounting for ground and excited state. The second line, eq. (3.19b), describes the inversion $\rho \equiv w$ with $b \in \{\mathrm{e}, \mathrm{h}\}$ depicting electrons and holes. These first two lines are basically the Bloch equation. The third line describes the population change of the reservoir w. This reservoir w is coupled to the inversion ρ by transition rates represented by $(\partial_t \rho_{b,m}^j)|_{\mathrm{col}}$. Finally, the last line, eq. (3.19d), is the Maxwell wave equation in the plane-wave and the slowly-varying amplitude and phase approximation.[67]

3.3.2. A mechanical analog

The full Maxwell–Bloch equations 3.19 are a powerful tool to evaluate light field and QD dynamics. There is, however, only a very limited intuitive access. To illustrate the underlying physical concepts, it is possible to reduce the system to an analogue mechanical toy model. We used this model to understand the basic mechanisms of pulse deformation under the influence of Rabi oscillations.[1] The description of this toy model in Ref. 1 is in some ways misleading, although the calculations are carefully performed and the conclusions will remain valid under the revision given in the following paragraphs.

As a first step of simplification of the eq. (3.19) we neglect many aspects of the full model: The QD ensemble is reduced to a single representative, only a single charge–carrier type is investigated ($p_m^j \to p$, $(\rho_{\mathrm{e},m}^j + \rho_{\mathrm{h},m}^j - 1) \to \rho$), the reservoir is cut off ($w_b \equiv 0$), spontaneous recombination is assumed to be infinitely slow ($W_m \equiv 0$), propagation is ignored (neglect z), and the QD transition energy shall match the light field central frequency ($\Delta\omega_m^j \equiv 0$). This results in a simplified set of equations:

$$\partial_t p = -i\frac{\Omega}{2}\rho - \frac{1}{T_2}p \tag{3.20a}$$

$$\partial_t \rho = -\mathrm{Im}\left[\Omega p^*\right] \tag{3.20b}$$

$$\partial_t E(t) = \frac{i\omega\gamma}{2\varepsilon_{\mathrm{bg}}\varepsilon_0}p. \tag{3.20c}$$

From a mathematical point of view, the eqs. (3.20a) and (3.20b) are identical to the problem of two coupled pendula as sketched in fig. 9. The equations of motion for the displacement $\boldsymbol{x} = (x_{\mathrm{p}}, x_\rho)^T$ are

$$\partial_t^2 \boldsymbol{x} + \begin{pmatrix} \beta \\ 0 \end{pmatrix} (\partial_t \boldsymbol{x}) + \begin{pmatrix} \omega^2 + D & -D \\ -D & \omega^2 + D \end{pmatrix} \boldsymbol{x} = \begin{pmatrix} x_{\mathrm{ext}}(t) \\ 0 \end{pmatrix}. \tag{3.21}$$

To evaluate the pulse deformation, it is necessary to look at eq. (3.20c). The pulse modification is proportional to the polarization pendulum displacement. The resulting pulse would be the sum of the original pulse (x_{ext}) and the contribution of the QD polarization. In Ref. 1, we reduced this problem and negelcted the contribution of x_{ext}. This is done legitimately, as the single oscillator model only represents an infinitesimal modification and the resulting modification still needs to be calculated iteratively, i.e. by consideration of propagation. This, however, would leave the realm of a toy model. Instead of choosing an arbitrary ratio for the summation of the original excitation and the modification by polarization, we neglect the original pulse.

It is important to stress that the Rabi oscillations are not derived from this coupled system, but rather constructed by the implementation of the coupling constant D. The mechanical analog therefor resembles the dynamics of the system under Rabi oscillations, but does not replace the derivation given in section 3.2.2. A much more sophisticated mechanical model can be found in Ref. 68.

Part II.

Experimental setup development

4. Established experimental concepts

The sophisticated setups presented in the later chapters have not been build from scratch. There are different types of experiments that have either been built by previous generations of scientists in our lab or that inspired the development of new experimental configurations.

4.1. Heterodyne detection

The terms heterodyne and homodyne detection originate from radio frequency engineering, but the concept has been used in IR and VIS optics for more than 25 years now.[69] In both cases, a signal wave of carrier frequency $\widehat{\nu}$ is superposed with a local oscillator (LO) (homodyne: $\widehat{\nu}_{\mathrm{LO}} \approx \widehat{\nu}$; heterodyne: $\widehat{\nu}_{\mathrm{LO}} \neq \widehat{\nu}$) and the interfering signals are mixed by a non–linear element. In the optical case, the LO and signal wave are laser modes and the non–linear element is simply the detector (that is linear in power and quadratic in field).

The heterodyne concept is thus the concept of modulation and demodulation. Like for an analog radio, the transmitter encodes information by modulating it onto a defined carrier band. The receiver knows the band and demodulates the transmission accordingly. The very same is done in the optical case: The set of laser modes is shifted by a defined frequency and demodulated later on. The three frequency regimes introduced in section 1.2.2 become important for optical heterodyning. The demodulation process is in fact twofold: The optical interference, which results in a detectable beating, demodulates the light field oscillation from the THz (ν) to the MHz ($\widehat{\nu}$) range. The detector signal is subsequently demodulated to the kHz range ($\widetilde{\nu}$) which can be analyzed by the computer. The signal quality of the optical interference is often improved by a *balanced detection*.[70] This type of detection provides common mode rejection and suppresses all signals that do not arise from the interference of the signal wave and the local oscillator.

4.1.1. Spectral shifting by acousto–optic modulators

Frequency shifts in the MHz range can be achieved by AOMs. An AOM can be understood both, in the wave and in the particle picture. In the wave picture, the acoustic field in a medium creates a

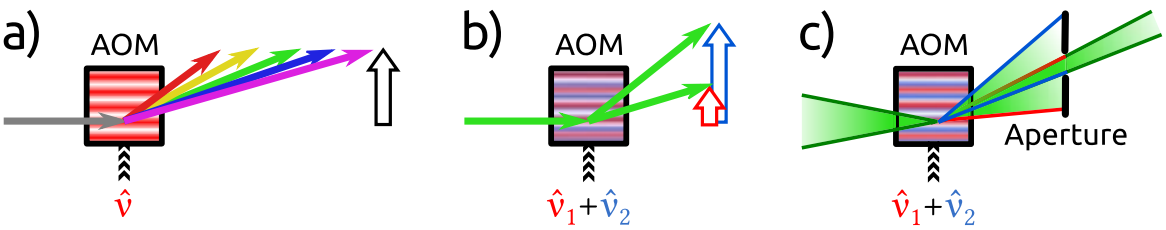

Figure 10: Beams deflected by an AOM under consideration of momentum conservation. (a) Dispersion separates white light at single AOM frequency $\widehat{\nu}$. (b) Application of two frequencies $\widehat{\nu}_1$ and $\widehat{\nu}_2$ creates two beams from monochromatic light. (c) For a focused incident beam, the overlap of beam cones can be spatially filtered in case b) (same applies for a)).

periodic density modulation which comes along with a periodic refractive index modulation. This periodic modulation acts as a Bragg grating where an incoming beam is diffracted. Besides the transmitted beam, several orders of diffracted beams may appear. The particle picture, however, is more intuitive: The AOM provides a field of phonons. Passing photons with frequency ν_{in} and momentum $\hbar\boldsymbol{k}_{\mathrm{in}}$ may be scattered by a phonon of energy $h\widehat{\nu}_{\mathrm{phon}}$ and momentum $\hbar\boldsymbol{k}_{\mathrm{phon}}$. Using energy and momentum conservation, the resulting photon is defined by

$$h\nu_{\mathrm{out}} = h\nu_{\mathrm{in}} + h\widehat{\nu}_{\mathrm{phon}} \tag{4.1a}$$

$$\hbar\boldsymbol{k}_{\mathrm{out}} = \hbar\boldsymbol{k}_{\mathrm{in}} + \hbar\boldsymbol{k}_{\mathrm{phon}}. \tag{4.1b}$$

Looking at the transmitted beam, the diffraction acts as an intensity modulation. The diffracted beam, on the other hand, is frequency shifted. The AOM is in this case often referred to as an acousto–optical frequency shifter (rather than a modulator). An amplitude modulation can also be achieved by electro–optical modulators that utilize e.g. the Pockels effect. The distinct advantage of AOMs is the easy selection of a single sideband by spatial filters due to eq. (4.1b).

This spatial selection becomes more complicated in the case of broadband laser pulses or if a superposition of frequencies is applied to the AOM. Each combination of photon and phonon momentum can result in a different diffraction angle according to eq. (4.1b). These cases are illustrated in fig. 10. In the white light experiments developed later on, the use of an aperture in the cone overlap (fig. 10 (c)) of a focused incident beam was a useful trick to achieve the desired output.

4.1.2. Heterodyne detection with lock-in amplifiers

A lock-in amplifier is an adjustable band-pass filter that allows signal analysis in amplitude and phase by homodyne detection. It consists of a signal demodulator of adjustable frequency and subsequent low-pass filters. By a phase–locked loop, the demodulator can be locked to an external reference frequency that is used as the local oscillator $\widehat{\nu}_{\mathrm{LO}}$. Demodulation is performed by multiplication of the signal by $\cos(\omega_{\mathrm{LO}}t)$ (denoted as X or "in-phase" component) and $\sin(\omega_{\mathrm{LO}}t)$ (Y or "quadrature" component), respectively, so the signal is transformed to a rotating frame. In this rotating frame, low-pass filters are applied that are adjustable by their filter order n ("slope") and their time constant $\omega_{\mathrm{cut}}^{-1}$.

Lock–in amplifiers are nowadays available with frequency ranges up to several hundred MHz. With slower lock–ins it is necessary to choose $\widehat{\nu}_{\mathrm{phon}}$ close enough to $\widehat{\nu}_{\mathrm{rep}}$, so that the interference of a mode with a neighboring mode at $\widehat{\nu}'_{\mathrm{phon}} = \widehat{\nu}_{\mathrm{phon}} - \widehat{\nu}_{\mathrm{rep}}$ can be observed.

4.1.3. Heterodyne spectral interferometry

Although not used in our experiments, an advanced approach of heterodyne detection is worth a brief discussion: the heterodyne spectral interferometry.[71,72] This technique is not based on lock–in detection. The modulation/demodulation concept is based solely on AOMs, while the low–pass function is emulated by the comparatively slow charge–coupled device (CCD). After the sample, the probe and the reference beam both enter a demodulation AOM set to the respective frequency difference of the desired signal band. The angle between probe and reference beam is aligned to the deflection angle of the first order of the AOM, so that the reference is deflected to the probe beam and vice versa. The AOM power is set to 50:50 deflection ratio. The desired mode is thereby shifted to 0 Hz and all other modes cancel out on the CCD.

This method has two advantages: A standard grating spectrometer can be used to detect a spectrally resolved signal and there is no frequency limitation by a limited bandwidth of the lock–in.

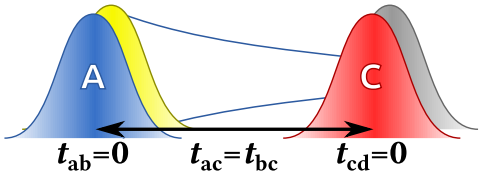

Figure 11: The 4PS of a PP experiment. In this case, pulse A also acts as pulse B which prepares a system population. Pulse D ("reference pulse") is superposed with pulse C ("probe pulse") to maximize the heterodyne signal.

Drawbacks, on the other hand, are the more complex setup and alignment as well as the impossibility of multi–band detection (chapter 6). Nowadays, lock–ins with far beyond 100 MHz bandwidth are available, so the entire relevant frequency range defined by the laser repetition rate is covered. Also spectral analysis will in our case be done by Fourier transform spectroscopy (FTS) (sections 4.3 and 5.2) rather than by grating spectrometers. Heterodyne spectral interferometry, however, impressively demonstrates that the concept of heterodyne detection is not limited to electronic filtering.

4.2. Pump-probe spectroscopy

In ultrafast spectroscopy, pump-probe (PP) experiments are used to reveal the temporal evolution of a system state after an initial perturbation by a strong pump pulse. Of course, the system evolution is not accessible directly, but needs to be recovered from the temporal evolution of the sample TF. A probe pulse with a defined time delay follows the pump pulse and passes under a modified TF. The differential gain and phase of the on and off case can be determined as described in section 1.3.1. From that, one can recover the actual processes in the system.

The 4PS is shown in fig. 11. The probe pulse is represented by pulse C. The pump pulse that generates a population modification in the sample is represented by a combination of pulse A and pulse B. This description has multiple advantages and will become more clear in the discussion of the 4PS of 2DCS in section 4.5.1. The pump probe delay is therefore t_{bc} which is in this case equivalent to t_{ac}.

4.2.1. By heterodyning

In heterodyne PP experiments, both, probe and reference pulse, are taken from the original laser beam and shifted by a specific frequency marker: the pump by $\widehat{\nu}_{\mathrm{ab}}$, the probe by $\widehat{\nu}_{\mathrm{c}}$. Pulse A and B are completely identical in this case. The frequency marker makes the pulses which pass the sample distinguishable even in collinear and co–polarized geometry. This is particularly useful for samples in waveguides that restrict the experimental geometry. To distinguish the pulses, the signal beam is interfered with the reference pulse D. The reference delay t_{cd} is usually kept constant at the signal maximum that defines the temporal overlap $t_{\mathrm{cd}} = 0$.

The data acquisition in the setup we inherited[8] was straightforward: After setting the pump–probe delay t_{bc}, the pump was switched on and off. For every state a lock–in value $S_{\mathrm{c}}^{(\mathrm{on})}$ and $S_{\mathrm{c}}^{(\mathrm{off})}$ was acquired, respectively. According to 1.24 the differential gain ΔG and phase difference $\Delta\Phi$ are given by

$$\frac{\ln 10}{10}\Delta G(t_{\mathrm{bc}}) + i\Delta\Phi(t_{\mathrm{bc}}) = \ln\left|\frac{S_{\mathrm{c}}^{(\mathrm{on})}(t_{\mathrm{bc}})}{S_{\mathrm{c}}^{(\mathrm{off})}}\right| + i\left(\varphi^{(\mathrm{on})}(t_{\mathrm{bc}}) - \varphi^{(\mathrm{off})}\right). \tag{4.2}$$

4.2.2. Chopping setups

Heterodyne detection of a beat frequency due to frequency shifts as described above is not the only pump-probe detection scheme using lock–in technique. In many cases an amplitude modulation of the pump beam[73] or both, pump and probe beam,[53] is sufficient to retrieve the desired signal. While mechanical chopping is limited to few kilohertz, AOMs are nearly unlimited in frequency (up to several 10 MHz) and allow for arbitrary modulation functions. Unlike heterodyne detection, these techniques do not provide phase information as interference with a reference beam is omitted. The major advantage, however, is superior sensitivity. While our standard heterodyne setup (section 5.3) requires averaging below differential signals of 1 % (0.04 dB) the standard chopping setups detected signals below 10^{-5} (0.000 04 dB).

If pump and probe beam are not collinear, modulation of the pump at $2\widetilde{\nu}_{\mathrm{ab}}$ is sufficient to generate a signal: The pump modulation creates a modulated excitation, this results in a modulated probe signal. Since the pump beam can be spatially filtered and does not hit the detector, the modulation imprinted on the probe is the only signal at $2\widetilde{\nu}_{\mathrm{ab}}$ and can be detected easily by the lock-in amplifier. In the 4PS the pump modulation is displayed as a superposition of two sidebands, namely pulse A with frequency $\nu_{\mathrm{a}} = \nu_{\mathrm{ab}} - \widetilde{\nu}_{\mathrm{ab}}$ and pulse B with $\nu_{\mathrm{b}} = \nu_{\mathrm{ab}} + \widetilde{\nu}_{\mathrm{ab}}$. Here it becomes evident why it is useful to represent the pump pulse by two constituent pulses in the 4PS.

In collinear geometry or for very low signal levels this is more difficult: The pump beam cannot be separated, its modulation is therefore also detected, and will dominate the lock-in signal. One circumvents this problem by modulation of the probe beam at $\widetilde{\nu}_{\mathrm{c}}$. Instead of $\widetilde{\nu}_{\mathrm{ab}}$ the lock-in is now locked to $(\widetilde{\nu}_{\mathrm{ab}} - \widetilde{\nu}_{\mathrm{c}})$, i.e. one of the sidebands resulting from the modulation of the pump imprinted to the already modulated probe signal. Neither pump nor probe alone carry this difference frequency, so their impact is filtered out by the lock-in. However, in this scheme there is no qualitative difference between pump and probe anymore, both are modulated the same way. This results in an undesired “probe-pump signal” that overlaps the pump-probe signal if both are on the same intensity level. For this double-chop technique, pump power exceeding probe power becomes crucial.

In sections 6.2 and 6.3 chopping techniques and frequency shift heterodyning will be applied in a hybrid setup to combine the sensitivity of chopping setups and the advantage of phase resolution and probe isolation of the frequency shift technique.

4.3. Fourier transform spectroscopy

Although one usually has prisms and gratings in mind when it comes to spectral analysis, a totally different type of spectrometry shows superior performance in a wide range of applications: Fourier transform spectroscopy (FTS). None of these commercial spectrometers has been used for this thesis, but the basic idea of FTS was the seed for our development of the Frequency Resolved Optical Short–pulse Characterization by Heterodyning (FROSCH) method (section 5.2) and the elaborate theory of FTS[18] has been and will be helpful to improve our approach.

The key idea of FTS is to obtain the spectral composition from a spatially resolved interference signal by Fourier transformation. Broadband light sources and a Michelson interferometer are used to create an interference pattern $I(x)$ depending on an optical pathway difference x. For monochromatic light of wavelength λ, a periodic sinusoidal signal is obtained. For a continuous spectrum of light this periodicity allows to identify contributions of specific wavelengths. As shown in section 1.1.2, the spectral resolution is here defined by the total range of x, while the spectral range depends on the spatial sampling rate.

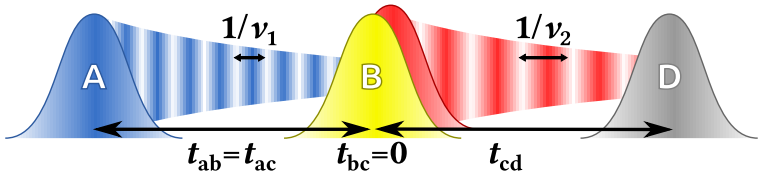

Figure 12: The 4PS of FWM experiments. The traditional FWM experiments do not resolve the frequency dependence, but rather scan the envelope of the signals.

The main advantages of FT spectrometers are high optical throughput, simultaneous broadband measurements (multiplexing), and nevertheless high spectral resolution by only using a single detector. Standard FT spectrometers cover pathway differences from 1 m to 5 m. The limiting factor for broadband measurements are the spectral limitations of beamsplitters, coatings, and detector sensitivity. By replacing these components the spectral range can be extended.[18]

4.4. Four-wave mixing

The theoretical aspects of FWM have already been described in section 3.1.1. In PP spectroscopy, carrier population dynamics are investigated and coherent effects are widely neglected. FWM experiments, on the other side, focus on the polarization dynamics. The inherited setup we mostly used for PP experiments has originally also been designed for FWM experiments. We will not conduct FWM experiments in the original way. In our context, FWM is the fundamental ingredient for 2DCS, so a brief review of this particular history will suffice.

Relevant for us are especially experiments in the *self–diffraction* configuration.[74] In this configuration, only two pulses are used instead of three. One of these two acts twice: It forms the transient grating together with the second pulse and is also diffracted. The according 4PS is shown in fig. 12, where the second pulse represents pulse B and pulse C as well. The heterodyne implementation of FWM does not rely on spatial k-vector selection, but on frequency filtering.[75] It is easy to see from eq. (3.6) that the frequency identifies that band as well as the k-vector does. In the case illustrated in fig. 12, the band of interest is $\widehat{\nu}_{\bar{\mathrm{a}}\mathrm{cc}}$, which oscillates at $2\widehat{\nu}_{\mathrm{c}} - \widehat{\nu}_{\mathrm{a}}$.

The typical question in FWM experiments is the determination of the T_2 time of an optical transition.[70,76] Already in the early experiments, both delays, t_{ab} and t_{cd}, have been scanned. A scan of t_{cd} is referred to as "time–resolved FWM", while the signal integrated over t_{cd} is called "time–integrated FWM". The delay between the two pulses, t_{ab}, reveals the coherence properties of the material. The ability of the two delayed pulses to form a transient grating depends on the ability of the material to maintain the coherence. This coherence decays with T_2. If this decay is measured over t_{ab}, this allows the direct determination of T_2. For InAs quantum dots in SOAs without carrier injection, T_2 decreases from 630 ps at cryogenic temperatures[77] to 220 fs at room temperature[78].

4.5. Multidimensional coherent spectroscopy

Multi-dimensional coherent spectroscopy (MDCS) combines the concepts of FTS and FWM. The observed signal is the very same as in FWM, but now it is not only "time–resolved", but even "phase–resolved". The concept of MDCS originates from nuclear magnetic resonance (NMR).[79] From this starting point in the radio frequency range it evolved to optical frequencies up to the

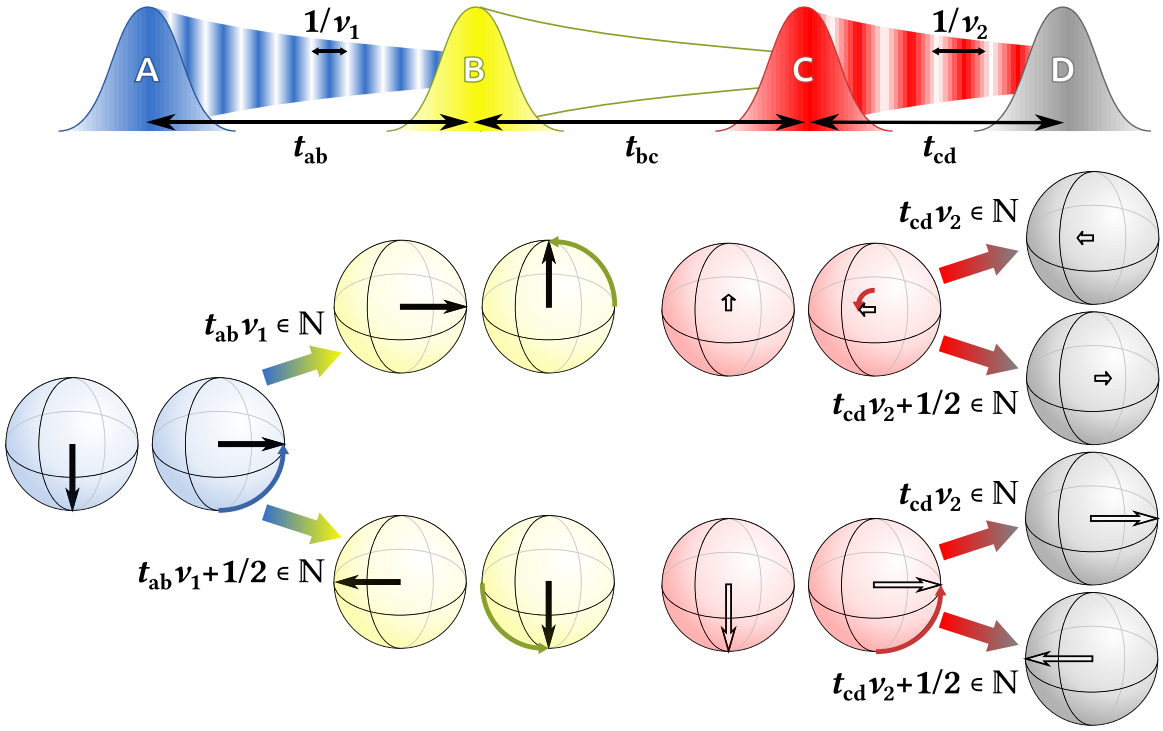

Figure 13: Excitation scheme for 2D spectroscopy. Four pulses (A to D) depicted by color interact with two transitions ν_1 (solid Bloch vector) and ν_2 (open Bloch vector). Depending on the respective delays, the resulting signals oscillates between the four extreme cases illustrated in the grey Bloch spheres of pulse D. This oscillation enables us to identify the coupling by a 2D FT.

VIS range. From a theoretical point of view, the concept of MDCS can be applied in an arbitrary number of dimensions.[80] In the following, however, the scope will be restricted to the 2D case.

4.5.1. Signal generation in 2DCS

In 2DCS three pulses (A – C) generate a fourth wave analog to the FWM case. The excitation scheme is shown in fig. 13 and the typical explanation is as follows:[81] Pulse A creates a coherence in the medium. This coherence evolves during the time period t_{ab} ($\equiv \tau$ in the 2DCS literature) until pulse B arrives. Pulse B stores the phase of the initial coherence in a population state. The population state decays during the period t_{bc} ($\equiv T$) until pulse C arrives. This pulse generates a coherence that radiates the signal during the time period t_{cd} ($\equiv t$). The last pulse D interferes with this radiation and thereby probes the result with phase resolution.

A detailed walk–through

The meaning of this description is illustrated in a case–by–case analysis in the Bloch sphere in fig. 13. We assume two coupled transitions with eigen–frequencies ν_1 and ν_2, respectively. In a simplified case, we assume that pulses A and B are resonant to ν_1, while pulse C is resonant to ν_2. It is very important to understand which part of the frequency information is encoded in which delay and why it can be deciphered by FT. For this illustration we use π–pulses, but the argumentation can be easily applied to the general case. As described in section 3.2.2, the Bloch

vector is defined with respect to the driving field and preserves its orientation in the uv–plane upon resonant excitation. However, there is not only one driving field in a three–pulse experiment. Every pulse defines its own rotating frame and therefore its own Bloch vector, so the Bloch spheres in fig. 13 are diplayed in the respective colors. The transition between two Bloch spheres depends on the relative phase of the electric fields and thus on the respective delay. After the initial creation of the coherence in the transition ν_1 by pulse A (red Bloch sphere), we can distinguish two extreme cases. In the first case (upper row) the delay t_{ab} is chosen with respect to the eigen–frequency ν_1 in a way that $t_{\mathrm{ab}}\nu_1 \in \mathbb{N}$. In this case, the second excitation is in–phase with the first excitation and the Bloch vector is flipped to the north pole of the sphere. In the other case (lower row), the delay $t_{\mathrm{ab}}\nu_1 + 1/2 \in \mathbb{N}$ and the second interaction has an inverse phase, so the Bloch vector is flipped to the south pole. So the variation of the delay by half a wavelength results in different scenarios, in this extreme case even in a change of the prepared population from $w = 0$ to $w = 1$. The important thing is now, that the information about this change is encoded in the delay t_{ab}, so a FT of any signal depending on this w along the delay t_{ab} will result in a Fourier component unequal zero.

With this preparation of pure population, no phase dependent events are expected during the period t_{bc}. In many experiments in the literature the delay $t_{\mathrm{bc}} \equiv T$ is therefore kept constant. If there is a relaxation path from transition ν_1 to ν_2, pulse C will find an initial population of this transition depending on the phase scenario described above. Pulse C acts on the system analog to pulse A: It creates a coherence (but now in the transition ν_2) that radiates the FWM signal during the period t_{cd}, which is probed by pulse D with phase sensitivity. Here it is important to understand that the result generated by pulse D depends in an oscillatory manner on two delays: On one hand on t_{ab} with an oscillation frequency ν_1 (due to the initial state of pulse C, prepared by pulse B), and on the other hand on t_{cd} with a frequency of ν_2. Both frequencies, ν_1 and ν_2, can be extracted by FT of the respective delay.

4.5.2. Presentation and interpretation of 2D spectra

Compared to the complexity of the 2DCS experimental concept, the presentation of extracted data is quite intuitive. The two–dimensional FT transforms the oscillatory FWM patterns into a 2D energy map. On the y axis, the pump photon energy E_{pump} is shown that corresponds to the transformed delay t_{ab}. From the example process above, the association with a pump process can be understood as the transition ν_1 is initially populated and therefore "pumped". On the x axis the transformed delay t_{cd} is shown as the probe photon energy E_{probe}.

If two transitions $\nu_1 \neq \nu_2$ like in the example above participate in the process, an off-diagonal contribution will indicate that coupling. In the case of a coherent coupling, the pump–probe process works time–reversed as well, so both off-diagonal elements $(h\nu_1, h\nu_2)$ and $(h\nu_2, h\nu_1)$ will appear on an equal level (if both transtitions are addressed by all pulses). Incoherent processes, that may happen during the period t_{bc} will result in off–diagonal unequal spots with the dominant spot with $E_{\mathrm{pump}} > E_{\mathrm{probe}}$.

But besides coupling information, 2DCS also provides information if only a single transition is involved. The homogeneous linewidth of the transition mediates a coupling between slightly off–resonant external field components. In a simplistic model, the coupling can be derived from eq. (3.11). The Lorentzian shape of this one–dimensional response function causes a two–dimensional pattern that is illustrated in fig. 14(a). The shape is not circular as one might expect, but shows a star pattern.

This pattern, however, can only be observed for a single transition or several transitions of the exactly same transition energy. In most experiments, one observes an ensemble with an inhomo-

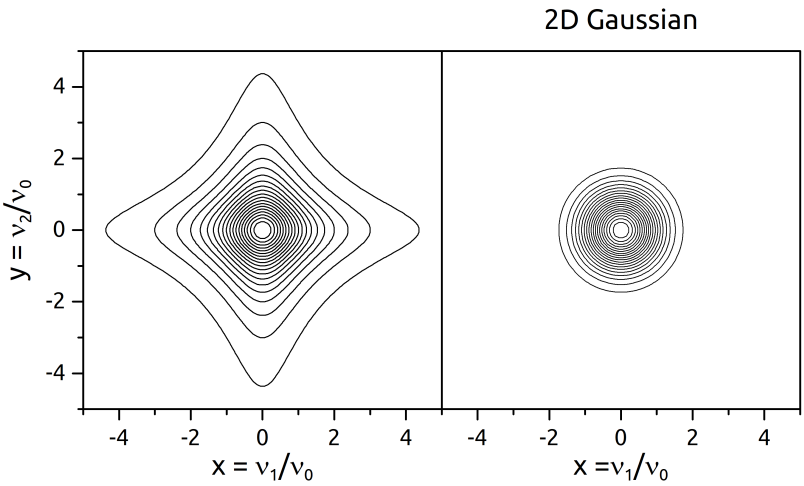

Figure 14: Comparison of a 2D spectrum with (left) Lorentzian response $\left(\left(x^2+1\right)\left(y^2+1\right)\right)^{-1}$ and (right) Gaussian response $\exp\left(-\left(x^2+y^2\right)\right)$. While the 2D Gaussian is radial symmetric due to $x^2+y^2=r^2$, the Lorentzian is not and shows the typical star pattern.

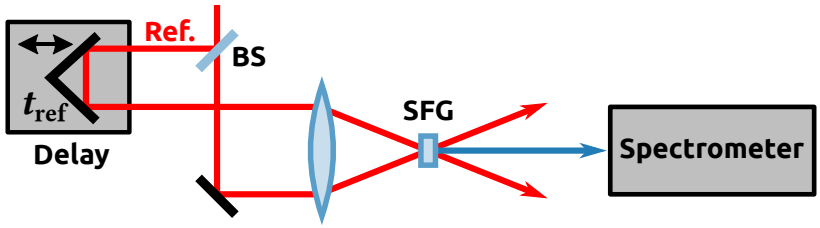

Figure 15: Concept of SFG FROG. If the beam–splitter (BS) is removed and an independent known reference pulse (Ref.) is used instead, this becomes the XFROG configuration.

geneous broadening of transition energies. The resulting pattern is therefore the superposition of a distribution of star patterns along the diagonal (ν_1, ν_2) with $\nu_1 = \nu_2$. It is a major benefit of 2DCS to distinguish between the inhomogeneous linewidth σ (diagonal section) and the homogeneous linewidth γ (cross–diagonal section). The quantitative determination of linewidths depends on the ratio of homogeneous an inhomogeneous linewidth. A calculation has been performed in ref. 82: The case of the "inhomogeneous limit" with $\sigma \gg \gamma$, which we assume for self–assembled QDs, shows a cross–diagonal section identical to eq. (3.11). To extract T_2 from a 2D spectrum, the phase slope along the cross–diagonal can be used according to eq. (3.13). This results in

$$T_2 = \frac{\hbar}{\gamma} = \hbar\left(\frac{\mathrm{d}}{\mathrm{d}E}\varphi(E_0)\right) \tag{4.3}$$

with γ in its photon energy representation.[83]

4.6. Pulse-shape analysis: FROG

FROG is a powerful non–linear technique for the analysis of femtosecond laser pulses. While the first FROG utilized self–diffraction as a third–order non–linearity[84], over the past 25 years several other types have been demonstrated.[85] Today the use second harmonic generation (SHG)[86]

(or more general the SFG) FROG is very popular. It is the most sensitive configuration and the formulae are very similar to the discussion of the FROSCH technique in section 5.2.1.

The scheme of the SFG FROG is displayed in fig. 15. The shown configuration is the standard auto–correlation configuration. If an independent pulse is used as the reference pulse, the modified scheme is referred to as the XFROG configuration. In the nonlinear crystal, the two incident pulses generate the sum frequency under momentum conservation. The resulting sum frequency beam analyzed by a spectrometer. The spectrogram is given by[87]

$$I^{\mathrm{SFG}}_{\mathrm{XFROG}}(\omega, t_{\mathrm{ref}}) = \left| \int_{-\infty}^{\infty} E(t) E_{\mathrm{ref}}(t - t_{\mathrm{ref}}) e^{-i\omega t} \mathrm{d}t \right|^2 , \tag{4.4}$$

so for a FROG measurement for every reference delay t_{ref} a spectrum is acquired. This spectro–temporal measurement allows the determination of the pulse frequency vs. time.

5. New opportunities by fast data acquisition

From a technical point of view, the most impressive progress in our lab during the past years has been reached due to a drastic reduction of lock–in integration times. This fast acquisition brings several benefits to the established detection schemes, but is also a prerequisite for some new experiment schemes. This section goes into the details of the new data acquisition scheme.

5.1. Fast data acquisition approach

In section 4.1 we have seen that heterodyne detection uses temporal integration to isolate a signal from a noisy background. In an ideal lab, long integration times improve the signal–to–noise ratio (SNR) by shrinking the bandpass window to the actual signal frequency (section 4.1.2). However, there is no ideal lab and long integration times become a bad idea if the signal is unstable, especially if it is subject to phase drifts of more than 180° as these will cancel out the signal upon integration. For interferometric detection, this means that beam paths lengths of probe and LO must not change by $\lambda/2$ during integration. Vibrations of mirrors caused by acoustic noise therefore pose a serious limitation to signal quality. To reduce the influence of the noisy lab environment, the optical table is equipped with housing walls and covers. Figure 16 (a) shows typical noise spectra with and without covers, respectively. The frequency range from 50 Hz to 5 kHz has a high noise level. The noise reduction by the cover is efficient in the range of few kHz (fig. 16 (b)), but does not suppress frequencies $\leq 200\,\mathrm{kHz}$. In this range, with acoustic wavelengths of about 10 cm, resonator effects inside the housing might play a role.

Under these external constraints, it is advisable to lift the data acquisition (DAQ) rate above this range. Early tests showed that the necessary reduction of the lock–in time constant to 50 µs or even 5 µs has a minor negative impact on the SNR compared to acoustic and thermal drifts.

5.1.1. Acquiring data

With the old detection scheme, however, this frequency range was not accessible due to simple speed limitations in digital data processing. In a digitalized world one tends to believe that analogue signal transmission is outdated and can be replaced in general. This might be true in case of well-defined tasks in a single apparatus, such as a personal computer or a digital lock-in amplifier. However, this statement becomes questionable or even wrong when a large number of loosely connected instruments is supposed to execute a task in a collective way. Without prepared data highways, data exchange based on requests and answers is limited to repetition rates of less than a kilohertz. If data from several instruments have to be documented simultaneously, serial requests reduce this rate even more, while parallel requests are hard to synchronize.

As an answer to this challenge, DAQ cards have become the heart of all our setups. First of all, they provide the setup clock defined by a single DAQ rate $\widetilde{\nu}_{\mathrm{daq}}$. Signals are acquired by the analog–to–digital converters (ADCs) of the DAQ card itself or by other instruments that receive a trigger signal provided by the DAQ card. Typical DAQ rates are in the range of 10 kHz to 50 kHz. If

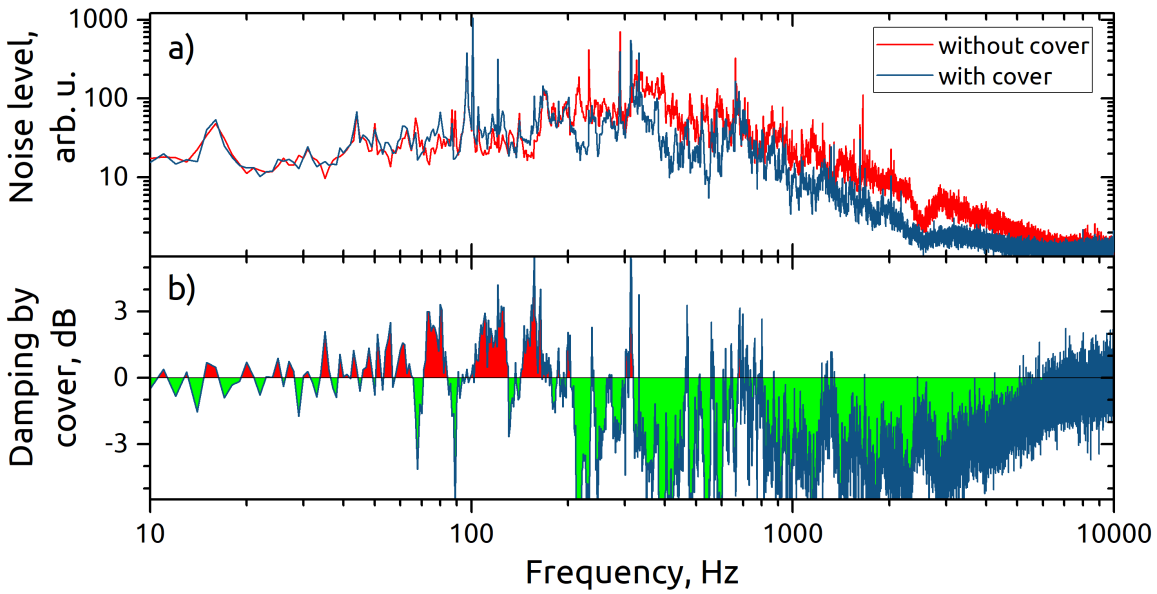

Figure 16: (a) Noise spectrum in the lab with and without table cover measured by a mobile phone. (b) Damping induced by cover, calculated from the noise data in (a).

a slave instrument is not able to follow the trigger with its digital data processing, it is sometimes advisable to use analog signal outputs that are linked to the ADCs of the DAQ card instead of direct digital DAQ. Such an implementation is for example shown in fig. 19: The lock–in signal is not acquired digitally, but transferred as an analog signal to the DAQ card. This scheme was used for the old DSP7280 lock–in, but is not necessary any more for the new ZI HF2LI (fig. 28).

5.1.2. Rapid scanning and MOLCH

The fast data acquisition (fDAQ) in the kilohertz range contradicts the old concept of stepwise setting delays and acquiring data. With fDAQ, it is inevitable to change to a *rapid–scan* approach. Delay stages are moving at constant velocity and the fDAQ ensures a sufficiently dense set of data points. The maximum velocity of the current stages is about $v_{\mathrm{del}}^{(\mathrm{max})} = 15\,\mathrm{mm/s}$. Two requirements must be fulfilled to allow heterodyne measurements at this velocity: On the one hand, the DAQ rate needs to be sufficiently high not to miss data features in between two sampling points. On the other hand, the signal needs to be constant during the lock–in integration time. The lock–ins used in our lab allow for minimal time constants (TCs) in the range of 1 µs, requiring the signal to be constant for about 10 µs. A corresponding DAQ rate of $\widetilde{\nu}_{\mathrm{daq}} = 100\,\mathrm{kHz}$ is easy to achieve. This results in a scan range of $2v_{\mathrm{del}}^{(\mathrm{max})}/(c\widetilde{\nu}_{\mathrm{daq}}) = 1\,\mathrm{fs}$ per data point. In the IR range, this equates $\lambda/4$. With a phase rotation of $2\pi/\lambda$ and a slowly varying signal envelope, this value is at the limit of what can be considered “constant”, but sufficient. With the present instruments, the stage velocity is therefore not a limitation.

Scanning the reference delay t_{cd} and tracking the lock–in signal $S(t_{\mathrm{cd}})$ has become a daily routine in the lab. We refer to this experiment as More–Or–Less Characterization by Heterodyning (MOLCH). More–Or–Less Characterization by Heterodyning (MOLCH) has been developed as a reduced version of FROSCH. MOLCH omits the measurement of t_{cd} on a sub–wavelength scale and thus does not provide spectral information. It is used to check the slowly varying envelope, so the typical display on the lab computer is $|S(t_{\mathrm{cd}})|$ (display of X and Y is also possible). With

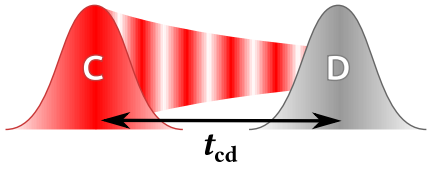

Figure 17: The 4PS of a FROSCH measurement is quite simple. Pulse A and pulse B are omitted, the measurement is a scan of the probe pulse C with the reference pulse D.

up to five scans per second in live–mode, MOLCH provides a real–time image of the heterodyne signal during alignment. The finding of the temporal overlap $t_{\mathrm{cd}} = 0$ as well as the optimization of the detector alignment have been simplified tremendously by the introduction of MOLCH.

5.1.3. Simultaneous multi-power measurements

In the traditional PP setup, the pump AOM power has been simply switched on and off. But whenever non–linear effects come into play, a more detailed power dependency becomes interesting. With the old detection scheme, one could for example repeat the measurement with half the AOM deflection power—but this would be ten minutes later and probably not very reliable. Here, fDAQ opens a new avenue: The power sequence is not limited to on and off, arbitrary sequences of power levels can be used. Instead of $S^{(\mathrm{on})}$ and $S^{(\mathrm{off})}$, a hole set of data like $S^{(1.0)}, S^{(0.9)}, \ldots, S^{(0.1)}, S^{(0)}$ is possible (where $S^{(j)}$ corresponds to a power level of $P = j \times P_{\mathrm{max}}$), as long as such a sequence period does not reach into the regime of acoustic noise. The diversification of power levels therefore implies an increased DAQ rate and a corresponding reduction of the lock–in time constant, but this is possible in many cases without a significant loss of SNR.

The concept of Simultaneous multi-power measurement (SMPM) can be applied for the pump AOM (detailed discussion in sections 5.3.1 and 10.2) as well as to the probe AOM (example in section 9.2). For a quantitative interpretation, a calibration measurement of the deflected beam power $P(|\mathcal{E}_{\mathrm{AOM}}|)$ over the driving electrical signal $\mathcal{E}_{\mathrm{AOM}}$ is necessary. A typical calibration curve is shown in fig. 25 (a) and can be used as a look–up table to determine $\mathcal{E}_{\mathrm{AOM}}$ for a desired power P.

In most of the presented experiments, we used an analog SMPM implementation: The scaling inputs ("video input") of the AOM drivers have been controlled via the analog output of the DAQ card and is thereby inherently synchronized to the analog inputs of the DAQ card. One drawback of this method is the scaling mechanism: While the frequency generator creates a continuous signal, a 0 V input on the "video input" refers to a maximal suppression of this signal. This maximal suppression, however, is not a complete annihilation of the signal, so a real "off" signal is not available. This problem is overcome with a digital implementation of SMPM presented in section 7.2.3.

5.2. The FROSCH technique

Frequency Resolved Optical Short–pulse Characterization by Heterodyning (FROSCH) is a technique we developed to analyze pulse shapes. Instead of using non–linear elements like the FROG technique (section 4.6), FROSCH is solely based on heterodyne detection. The pulse shape is calculated from the lock–in signal of a scan of t_{cd}

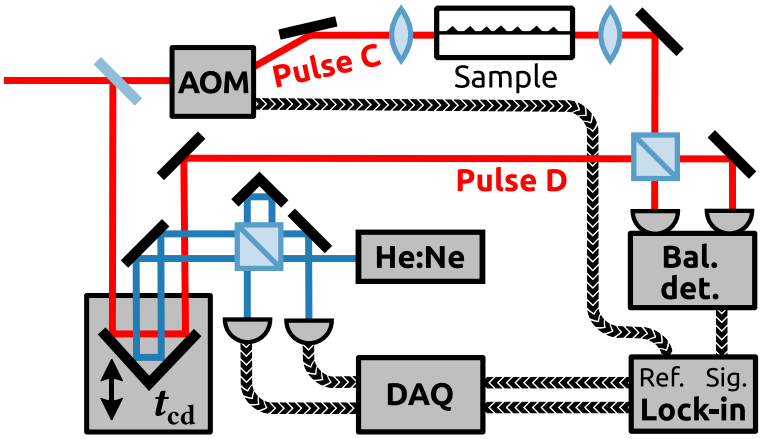

Figure 18: Minimal FROSCH setup. The incident pulse is split into a probe pulse C and the LO pulse D. The reference delay t_{cd} is scanned. The helium–neon laser is used to set up the complex Michelson interferometer. Four real signals are acquired.

5.2.1. The FROSCH signal

The initial pulse is composed of discrete laser modes with complex amplitudes $\mathcal{E}_\omega^{(0)}$. It is split into the pulse $\mathcal{E}_j$ that is supposed to be analyzed, and the LO pulse $\mathcal{E}_{\mathrm{LO}}$:

$$\mathcal{E}_{\mathrm{LO}}(t) = \sum_\omega \mathfrak{T}_{\mathrm{LO}}(\omega)\mathcal{E}_\omega^{(0)} e^{i\omega t} \tag{5.1}$$

$$\widehat{\mathcal{E}}_j(t) = \mathcal{E}_j(t)e^{i\widehat{\omega}t} = \sum_\omega \mathfrak{T}_j(\omega)\mathcal{E}_\omega^{(0)} e^{i(\omega+\widehat{\omega})t}, \tag{5.2}$$

where $\widehat{\mathcal{E}}_j(t)$ includes the frequency shift $\widehat{\omega}$ introduced by the AOM. The balanced detectors yield an electric field $\mathcal{E}_{\mathrm{det}}$ that is proportional to the light intensity:

$$\begin{aligned}
\mathcal{E}_{\mathrm{det}}(t, t_{\mathrm{cd}}) &\propto \mathfrak{T}_{\mathrm{det}}(\omega)\frac{1}{2}\left(\left|\widehat{\mathcal{E}}_j(t) + \mathcal{E}_{\mathrm{LO}}(t-t_{\mathrm{cd}})\right|^2 - \left|\widehat{\mathcal{E}}_j(t) - \mathcal{E}_{\mathrm{LO}}(t-t_{\mathrm{cd}})\right|^2\right) \\
&= \mathfrak{T}_{\mathrm{det}}(\omega)\left(\widehat{\mathcal{E}}_j(t)\mathcal{E}^*_{\mathrm{LO}}(t-t_{\mathrm{cd}}) + c.c.\right) \qquad (5.3a) \\
&= \mathfrak{T}_{\mathrm{det}}(\omega)\sum_{\omega,\omega'}\left(\mathfrak{T}_j(\omega)\mathfrak{T}^*_{\mathrm{LO}}(\omega')\mathcal{E}_\omega^{(0)}\mathcal{E}_{\omega'}^{(0)*} e^{i(\omega-\omega'+\widehat{\omega})t} + c.c.\right) \\
&= \sum_\omega \left|\mathcal{E}_\omega^{(0)}\right|^2\left(\mathfrak{T}_j(\omega)\mathfrak{T}^*_{\mathrm{LO}}(\omega)e^{i\widehat{\omega}t} + c.c.\right). \qquad (5.3b)
\end{aligned}$$

In the last line we assumed that the comparatively slow detector electronics $\mathfrak{T}_{\mathrm{det}}(\omega)$ filter out all frequencies with $\omega \neq \omega'$. At this point the major difference between FROSCH and FROG becomes evident: In eq. (5.3b), the original pulse $\mathcal{E}^{(0)}$ only contributes to the signal by its absolute value, not by its phase. Even though there will be more arguments, the restriction imposed by the detector electronics alone will make FROSCH insensitive to the phase of the initial pulse. FROG overcomes this problem by the use of a spectrometer, i.e. an array of detectors. This allows FROG to include the contributions of $\mathcal{E}_\omega^{(0)}\mathcal{E}_{\omega'}^{(0)*}$ for $\omega \neq \omega'$ to its analysis which reveal the original phase. So be aware: FROSCH is not suitable to characterize the original pulse, but it is an excellent tool to determine the relative modifications introduced by $\mathfrak{T}_j(\omega)\mathfrak{T}^*_{\mathrm{LO}}(\omega)$.

The detector signal is finally analyzed by the lock–in amplifier. The lock–in bandwidth is, of course, much smaller than that of $\mathfrak{T}_{\mathrm{det}}(\omega)$ (we can simply assume an infinite TC), so we can ignore $\mathfrak{T}_{\mathrm{det}}(\omega)$ and put eq. (5.3a) into the lock–in formula:

$$\begin{aligned} S(t_{\mathrm{cd}}) &= \int_{-\infty}^{\infty} \mathcal{E}_{\mathrm{det}}(t, t_{\mathrm{cd}}) e^{-i\widehat{\omega}t} \mathrm{d}t \propto \int_{-\infty}^{\infty} \widehat{\mathcal{E}}_j(t) \mathcal{E}^*_{\mathrm{LO}}(t - t_{\mathrm{cd}}) e^{-i\Delta\omega t} \mathrm{d}t \\ &= \int_{-\infty}^{\infty} \mathcal{E}_j(t) \mathcal{E}^*_{\mathrm{LO}}(t - t_{\mathrm{cd}})\, \mathrm{d}t = \left(\mathcal{E}_j \star \mathcal{E}_{\mathrm{LO}}\right)(t_{\mathrm{cd}}). \end{aligned} \tag{5.4}$$

The signal $S(t_{\mathrm{cd}})$ thus represents the cross–correlation of the two pulses according to eq. (1.8). Utilizing this fact, we can generalize the insensitivity of FROSCH to the initial pulse phase: If both pulses are exposed to the same additional transfer function $\mathfrak{T}(\omega) = G(\omega)\exp(i\Phi(\omega))$ defined according to eq. (1.23), we can use eq. (1.9) to determine the cross–correlation of the modified fields:

$$\begin{aligned} \left(\mathcal{E}'_j \star \mathcal{E}'_{\mathrm{LO}}\right)(t_{\mathrm{cd}}) &= \mathcal{F}^{-1}\left\{\left(\mathfrak{T}(\omega)\mathcal{E}_j(\omega)\right)^* \cdot \left(\mathfrak{T}(\omega)\mathcal{E}_{\mathrm{LO}}(\omega)\right)\right\} \\ &= \mathcal{F}^{-1}\left\{G^2(\omega) \cdot \left(\mathcal{E}^*_j(\omega) \cdot \mathcal{E}_{\mathrm{LO}}(\omega)\right)\right\} \\ &= \left(\mathcal{F}^{-1}\left\{G^2(\omega)\right\}\right) * \left(\mathcal{E}_j \star \mathcal{E}_{\mathrm{LO}}\right)(t_{\mathrm{cd}}). \end{aligned} \tag{5.5}$$

Just like the initial pulse phase, a common phase change imposed by the TF in both arms cancels out.

5.2.2. The complex-value interferometer

Precise position tracking is a crucial part of FROSCH measurements. A simple Michelson interferometer incorporating a Helium-Neon laser, a beamsplitter, two plane mirrors (one of them mounted on the delay stage), and one detector has been used in Ref. 1 and provided sufficient position control. However, there are two major drawbacks in this simple implementation: Firstly, reference beam and control beam do not use the same optical element, so differences in motion of these two elements will result in erroneous position values, in particular vibrations are observed. Secondly, a single detector provides a sinusoidal signal. At extreme values this signal is symmetric in direction, i.e. forward movement cannot be distinguished from backward movement.

Meanwhile we overcame both of these drawbacks. Using the same retro–reflector for the control beam as for the reference beam is a standard procedure.[88] To obtain unambiguous directional information, a second detector is necessary. It can be implemented as shown in fig. 18 in backward direction that is often ignored although 50 % of the intensity are back–reflected. Here, an interferometric fact can be incorporated that usually is seen as an error source: Any real world instrument with finite aperture size exhibits interference fringes in the detector plane,[18] i.e. constructive and destructive interference alternate spatially. By a slight imperfection of alignment it is easy to set one detector to a constructive fringe, while the other one is at a destructive fringe for the same delay. This phase offset of ideally 90° is usually maintained for a sufficient distance of some millimeters. If one detector is at its extreme value, the other one has a zero and provides optimal directionality.

While we desire a circular signal in the complex plane, we will accept oval signals in most cases. But these oval signals must be mapped to a circle. An easy way to do this is to rotate the oval in a way that the long axis superposes the real axis and afterwards stretch the imaginary part to

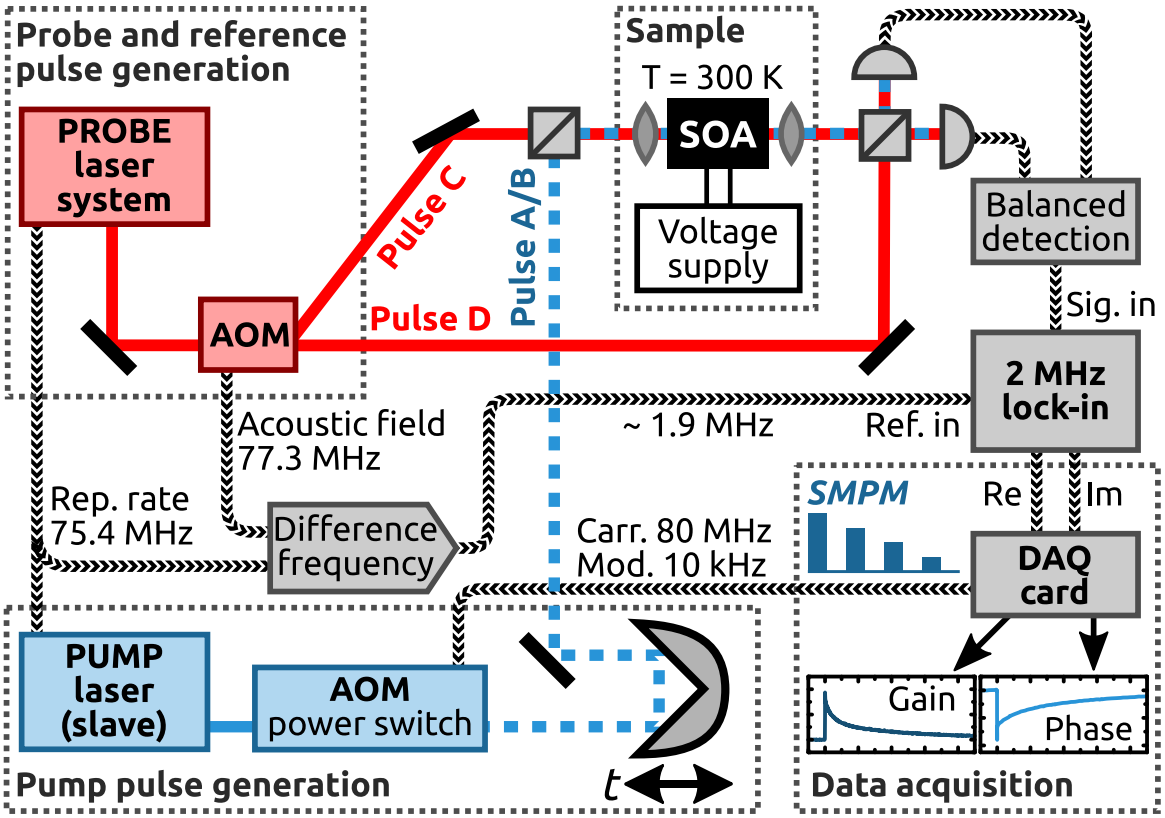

Figure 19: Heterodyne pump–probe setup as it has been used in Ref. 3. Caution: Using the transmitted AOM beam as local oscillator turned out to create artificial offsets. Similarly published in Ref. 3.

retrieve the circle. There is an astonishingly simple trick how to determine the long axis from an oval complex signal array $\boldsymbol{S}$:

$$Ae^{i\alpha} = \sqrt{\sum_{j=1}^{n}\left(S_j - \frac{1}{n}\left(\sum_{i=1}^{n} S_i\right)\right)^2}. \tag{5.6}$$

After the offset correction, the square turns opposite phase values to the same value, the oval is transformed to an “egg” shape. The square root of the center of mass of this egg indicates the position of the long axis.

5.3. Fast pump-probe

The general concept of traditional PP measurements has been described in section 4.2.1. The setup in the state of Ref. 3 is sketched in fig. 19. In contrast to a FROSCH measurement, there is no need to scan t_{cd}, it is set to the maximum signal at $t_{\mathrm{cd}} \equiv 0$. The new rapid–scan approach can now be applied to the pump–probe delay t_{bc}. Like in the following experiments, t_{ac} will be the delay that is controlled in the experiment. In the context of a PP experiment, this delay equals t_{bc}.

It turned out that DAQ rates of $\widetilde{\nu}_{\mathrm{daq}} = 100\,\mathrm{kHz}$ with corresponding lock–in time constants of $\leq 2\,\mu\mathrm{s}$ are possible. As discussed in section 5.1.2, this corresponds to a minimal temporal resolution of 1 fs, which is way too high for a PP measurement with a pulse duration limited resolution of

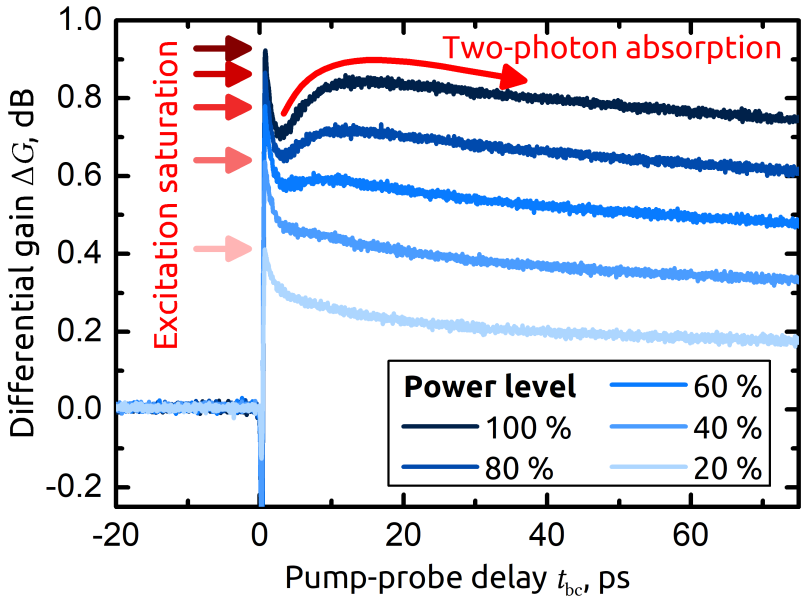

Figure 20: Example for processes that can be identified by SMPM. The excitation saturation causes a non–linearly increasing peak height. TPA and subsequent relaxation from higher states causes a carrier feeding on the timescale of tens of picoseconds. These resonant PP curves are taken on the QD GS at low injection current (2 mA).

200 fs. This oversampling, however, allows to average the processed data $S^{(\mathrm{on})}/S^{(\mathrm{off})}$ rather than the original values $S^{(\mathrm{on})}$ and $S^{(\mathrm{off})}$, respectively. This reduces the susceptibility to common phase drifts which are eliminated in the ratio.

In the setup shown in fig. 19, we still used the traditional scheme[70] that uses the transmitted beam of the AOM as reference pulse D. It turned out that this beam also carries a modulation at the driving frequency $\widehat{\nu}_{\mathrm{c}}$. We detected $S_{\mathrm{c}} \neq 0$ with pulse C blocked and only with pulse D on the detector. This results in artificial offsets, especially in PP experiments. With the later implementation (fig. 28) that splits pulse D from pulse C using a beam sampler right after the laser, such offsets have been widely eliminated.

5.3.1. Advantages of SMPM

There might be many processes that contribute to the temporal evolution of a pump-probe trace. Knowledge about the linearity of excitation response can be extremely useful to weight these contributions. SMPM provides this check of linearity with a high degree of accuracy. In the context of PP measurements, the observation of TPA and excitation saturation are typical phenomena to be identified by SMPM.

Exemplary sets of SMPM differential gain curves are shown in fig. 20. The SMPM power levels are linearly increasing, but the QD excitation at $t_{\mathrm{bc}} = 0$ is obviously not. This is a clear indicator for the saturation of the QD population. An application and detailed discussion of this signature will follow in section 10.2. The signature of TPA can also be easily identified: TPA creates carriers in high energy bulk states that relax down to the probed spectral range on the timescale of tens of picoseconds. As TPA scales with the square of power, the presence for high power and the simultaneous absence for low power is an unambiguous indicator.

6. Multiband detection for sideband pump–probe

So far, a single heterodyne frequency has been tracked. By tracking multiple frequencies in multiple demodulator units, one can overcome different limitations of the single lock–in setups presented in chapter 5. Similar usage of parallel lock–in amplifiers has been demonstrated for FWM[89] as well as PP experiments[90]. However, the setups presented in the following add several new aspects to this concept.

6.1. Separation of multiple frequencies

In our experiments, we use two methods to filter electrical signals. The final isolation of bands is performed by a lock–in amplifier. Before that, we are able to filter the electrical detector signal by high, low, and band pass filters. Although both methods are conceptually closely related, there are some noteworthy differences.

6.1.1. Isolation of bands by lock–in amplifiers

For a single frequency of interest the requirements to isolate the heterodyne frequency were easy to fulfill: After leaving the range of acoustic and line noise affected frequencies towards the megahertz range, there was merely white noise surrounding the desired peak. If two frequencies have to be observed by two lock-ins, the situation is fairly different because crosstalk has to be suppressed. The degree of isolation of two lock–in frequencies depends on the frequency spacing and the lock–in TC. For a narrow spacing, a large TC can be used to isolate the bands at the cost of long settling times resulting in reduced DAQ rates.

In modern digital lock–in amplifiers, the analog time signal is digitized after an initial amplifier stage. Typical modern devices provide 14 bit resolution.[24] This is usually not a limiting factor in our case as the separation of signals with a level ratio of more than 1000 would require very large TCs. The filtering in the lock–in amplifier is performed in the rotating frame of the reference signal: The signal is demodulated and subsequently filtered. In this context, it is as easy to distinguish for example 61 MHz from 60 MHz as it is to distinguish 1 MHz from 0 MHz. In the respective rotating frame, both cases have a separation of 1 MHz. The lock–in filtering therefore demands *absolute* frequency separation.

6.1.2. Analog signal pre–conditioning

Let us now compare the lock–in filtering to the analog signal filtering, especially to the important case of low pass filters. The low pass filter transfer function has already been discussed in section 1.3.2. An expample of two signals is given in fig. 21 with an initial level ratio of 100 (red curves). The strongest relative suppression is achieved in the range above the cut–off frequency (linear range in the log–log graph). The suppression of one band becomes more efficient when the ratio of the two frequencies is large. In contrast to the lock–in, the low–pass filtering demands

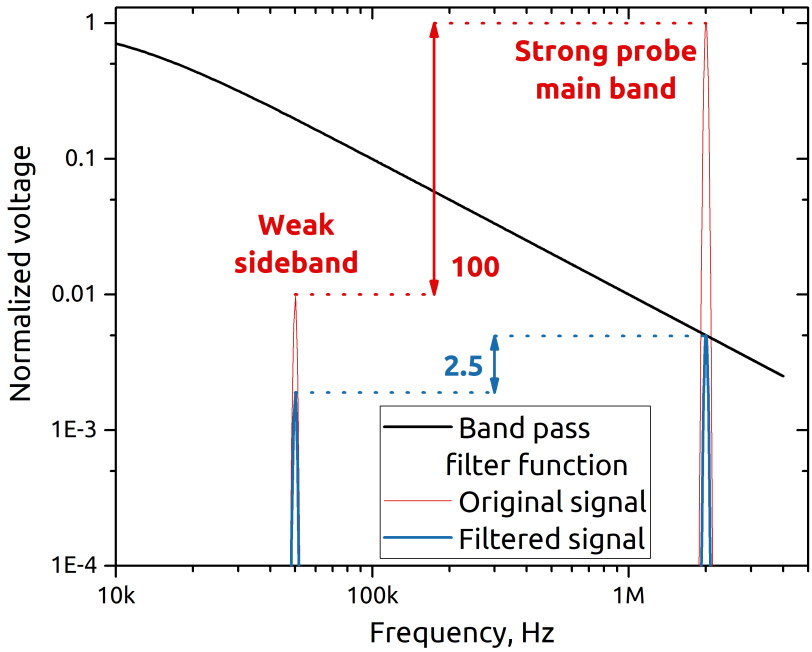

Figure 21: Analog signal pre–conditioning by a low–pass filter. The heterodyne band at 2 MHz is stronger than the sideband at 50 kHz by a factor of 100 on the detector (red curves). By a low–pass filter, this ratio can be reduced to 2.5 which increases the dynamic range of the lock–in amplifier.

relative frequency separation. This analog signal pre–conditioning will be one of the keys to detect low signals in multi–band experiments. It allows us to use lower lock–in TCs and take data much faster. In chapter 7, a band–pass filters will be applied. In that case, the argument of relative frequency separation is not valid anymore, but it will still be useful to look at the transfer function on a log scale.

6.2. The sideband setup for low signals in Austin

The main goal of my stay with the group of Professor Li at the University of Texas at Austin was to introduce heterodyne detection to an existing pump-probe setup in order to filter out artifacts efficiently. Our central research objective was a deeper understanding of exciton-trion dynamics in TMDs upon polarization selective pumping and probing. In earlier experiments[53] it was possible to filter the pump even in collinear geometry since it was cross-polarized with respect to the probe. For copolarized beams, however, probe-pump signals (section 4.2.2) obscured the pump-probe signal.

The first straightforward approach of copying the existing Berlin detection scheme (section 5.3) revealed its sensitivity limitations: For monolayer TMDs, signal levels with peak heights below 1 % were expected, which was impossible to retrieve as time–resolved signal. While heterodyne detection distinguishes pump and probe qualitatively, the measurement of a signal modification is not background-free and therefore lacks the sensitivity of chopping detection—loosely spoken, it is easier to distinguish 0.01 from 0 than 1.01 from 1. Here, the idea of a hybrid setup was born: A setup that relies on heterodyne detection and yet identifies signal modifications by continuous modulation rather than by defined switching. The clue in this approach is that the continuous

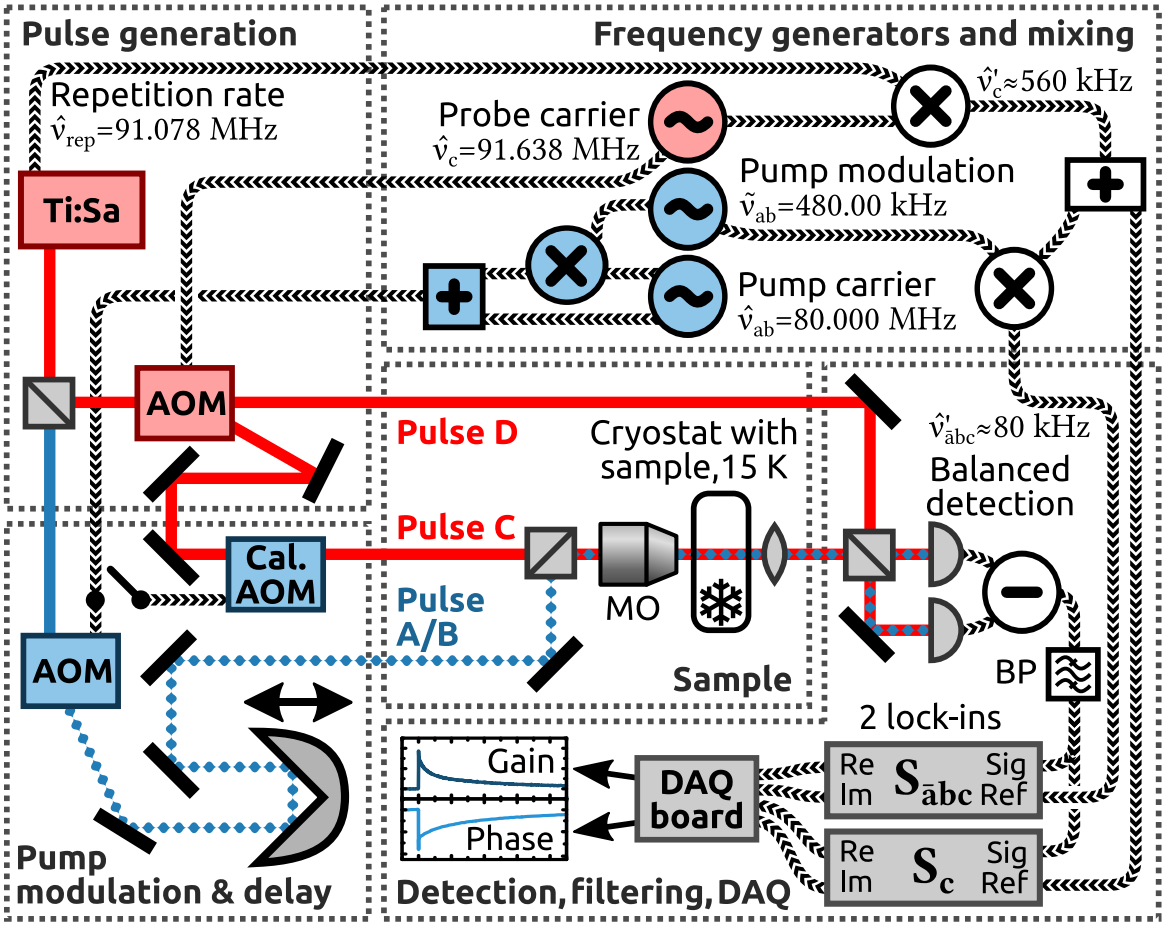

Figure 22: The Austin setup is a hybrid of heterodyne detection and the double–chop approach. A complicated analog frequency mixing scheme is necessary to create the modulation and to lock the lock–in amplifiers to the respective bands.

modulation of a signal shows up as a sideband in Fourier space. Whenever the probe beam is modified by a pump beam modulated at $\widetilde{\nu}$, the heterodyne signal oscillates at $\widetilde{\nu}$, i.e. sidebands appear at $\widehat{\nu}_c \pm \widetilde{\nu}$. By detecting a sideband using a second lock–in, the signal modification can be retrieved like it is illustrated in fig. 3.

The setup based on these considerations is shown in fig. 22. The titan-sapphire laser is a Griffin 5 from KMLabs with a repetition rate of $\widehat{\nu}_{rep} = 91.078\,\mathrm{MHz}$. The carrier frequencies of the AOMs are $\widehat{\nu}_{ab} = 80\,\mathrm{MHz}$ for the pump and $\widehat{\nu}_c = 91.638\,\mathrm{MHz}$ for the probe, respectively, so the heterodyne frequency is at $\widehat{\nu}'_c = 560\,\mathrm{kHz}$. To create the sideband, the pump carrier frequency is modulated by a further frequency generator at $\widetilde{\nu} = 480.00\,\mathrm{kHz}$. The modulation scheme is quite complicated and has been taken directly from the original double–chop scheme: The carrier signal is split, one part is mixed with $\widetilde{\nu}$ and afterwards recombined with the second part of the carrier signal. This implementation therefore creates the signal

$$\frac{1}{2}\left(1 + \sin(2\pi\widetilde{\nu}_{ab}t)\right)\sin(2\pi\widehat{\nu}_{ab}t), \tag{6.1}$$

which in fact has some drawbacks that will be discussed in section 6.3.

Figure 22 shows the setup in transmission geometry, but it has been successfully tested in reflection geometry as well. In both cases, a microscope objective is used to focus pump and probe

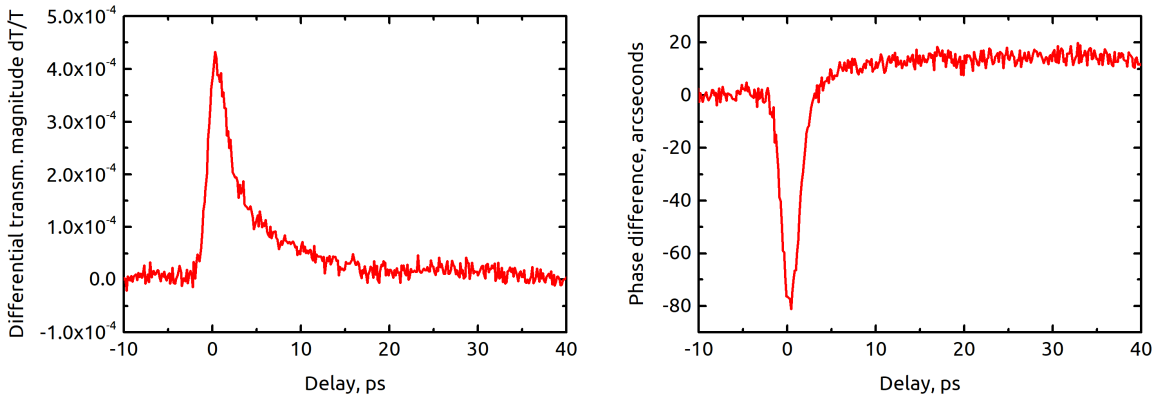

Figure 23: Proof of principle data taken with the setup shown in fig. 22. The pump and probe wavelengths are documented in the Austin lab book and therefore not available.

beam, respectively, onto a TMD flake that is mounted in a cryostat and kept at a temperature of 15 K. The transmitted (or reflected) beam is superposed with the reference on a New Focus 2107-FC balanced photoreceiver. The modulation sideband imprinted on the probe beam by the modulated pump beam is tiny compared to the heterodyne signal in general. To enable simultaneous detection, the low pass filter is set to the cut–off frequency 100 kHz, so the heterodyne signal at $\widehat{\nu}_{\mathrm{c}}' \approx 560\,\mathrm{kHz}$ is suppressed while the sideband at $\widehat{\nu}_{\bar{\mathrm{a}}\mathrm{bc}} \approx 80\,\mathrm{kHz}$ passes the filter with minor loss. This pre–filtered signal is analyzed by two lock-ins from Stanford Research, a model SR844 for signal S_{c} at the heterodyne frequency and a model SR830 for the sideband signal $S_{\bar{\mathrm{a}}\mathrm{bc}}$.

Analog to eq. (4.2), the differential gain and phase are

$$\frac{\ln 10}{10}\Delta G(t_{\mathrm{bc}}) + i\Delta\Phi(t_{\mathrm{bc}}) = \frac{\mathfrak{T}_{\mathrm{c}} S_{\bar{\mathrm{a}}\mathrm{bc}}(t_{\mathrm{bc}})}{\mathfrak{T}_{\bar{\mathrm{a}}\mathrm{bc}} S_{\mathrm{c}}} = G_0 \exp\left(i\varphi_0\right) \frac{S_{\bar{\mathrm{a}}\mathrm{bc}}(t_{\mathrm{bc}})}{S_{\mathrm{c}}}. \tag{6.2}$$

The TFs $\mathfrak{T}_{\mathrm{c}}$ and $\mathfrak{T}_{\bar{\mathrm{a}}\mathrm{bc}}$ take the differences in the signal propagation into account, especially the differences in the electrical filtering. Although the lock–in signals S_{c} and $S_{\bar{\mathrm{a}}\mathrm{bc}}$ have a defined phase relation, the phase φ_0 is unknown. A calibration measurement is necessary to determine φ_0 for the case $\Delta G > 0$ and $\Delta\Phi = 0$, i.e. a pure amplitude modulation. We used an additional calibration AOM that is placed in the pulse C beam. During the measurement, this AOM is not driven. For the calibration measurement, the pump beam is blocked and the pump AOM driving voltage is applied to the calibration AOM. This scenario resembles a perfect amplitude modulation of pulse C and the measured phase difference of S_{c} and $S_{\bar{\mathrm{a}}\mathrm{bc}}$ can be used to compensate for φ_0.

During my stay in Austin, we were able to demonstrate this novel approach and to acquire some preliminary data during the testing process. An exemplary set of test data on a WSe_2 monolayer sample is shown in fig. 23.

6.3. Modification of the Austin setup in Berlin

For the integration of the sideband PP scheme into the Berlin setup, several improvements have been applied. Instead of two independent lock–ins, the use of the ZI HF2LI lock–in allows to skip the complicated analog mixing. The necessary frequencies can be generated digitally. The setup shown in fig. 24 is the state of the development that was used to acquire the data for Ref. 4. It still incorporates independent AOM drivers, which will become unnecessary with the modifications introduced in section 7.2.2.

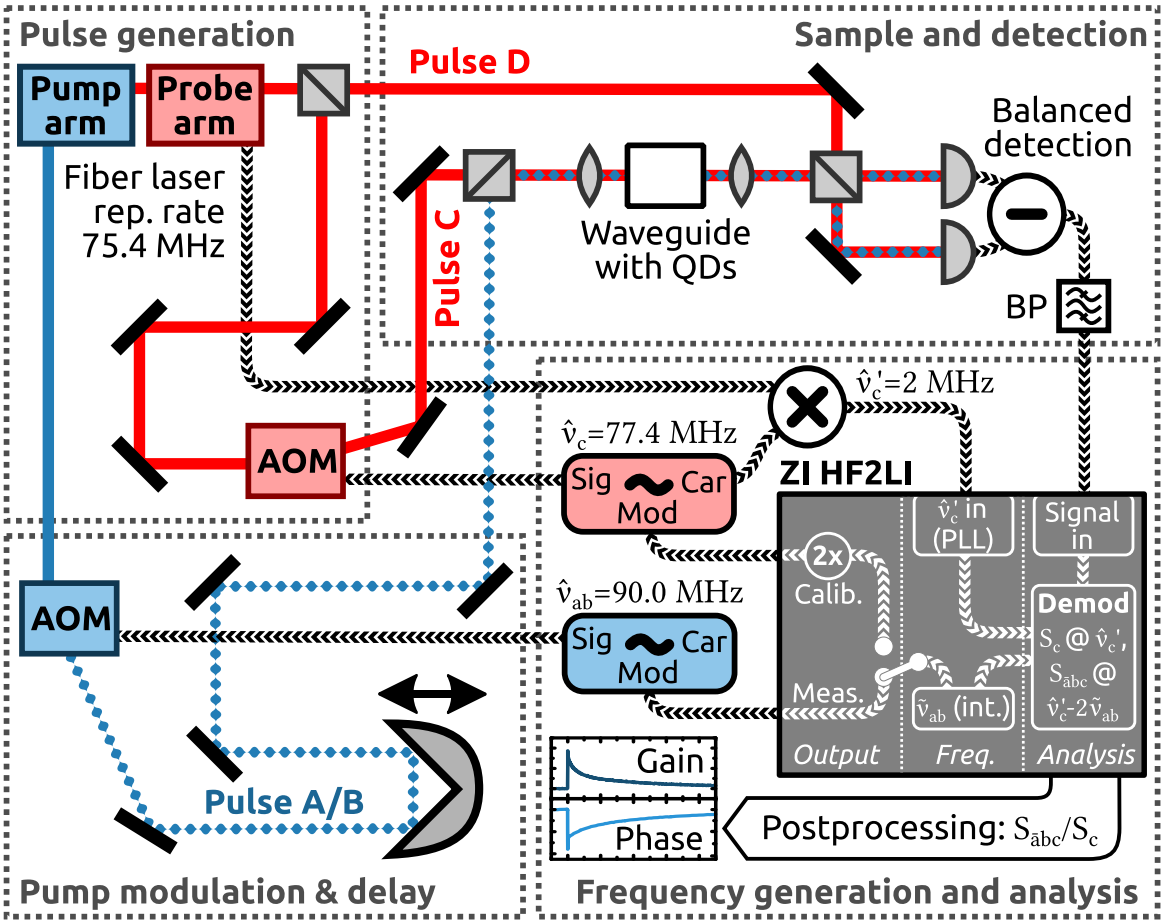

Figure 24: This setup is a modification of the setup developed in Austin (fig. 22). Here, the frequency generators provide internal modulation, so external mixing of AOM signals is not necessary. Instead of an additional calibration AOM the probe AOM is used directly to generate a calibration signal. Similarly published in Ref. 4.

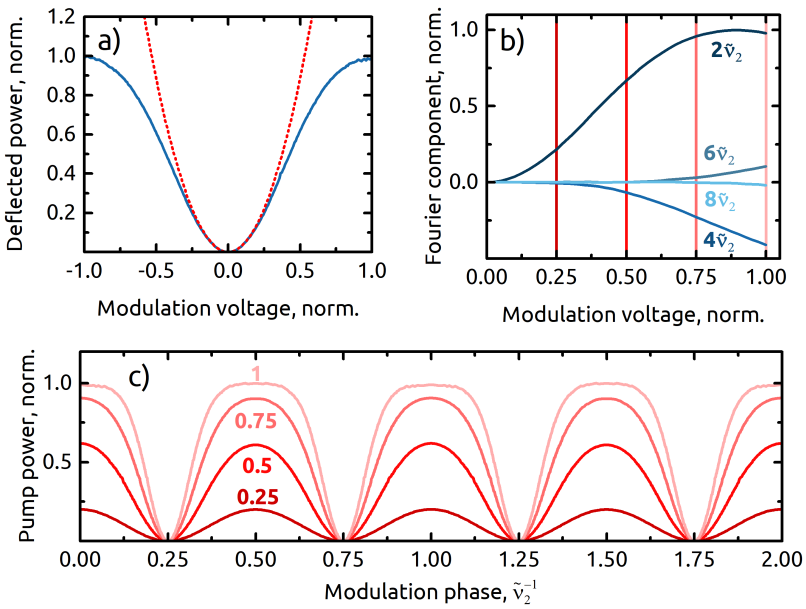

Figure 25: AOM characteristics: (a) The deflected power (solid blue) over the modulation voltage can be approximated by a parabola for low modulation levels. (b) The deviation from the parabola results in the generation of higher harmonics. (c) The higher harmonics result in a temporal signal that deviates from the ideal sinusoidal modulation for high modulation voltages. Similarly published in Ref. 4.

Unlike for the Austin setup in eq. (6.1), the modulated pump AOM signal in this case is

$$\sin(2\pi\widetilde{\nu}_{\mathrm{ab}}t)\sin(2\pi\widehat{\nu}_{\mathrm{ab}}t). \tag{6.3}$$

The envelope of this oscillation is $|\sin(2\pi\widetilde{\nu}_{\mathrm{ab}}t)|$, which seems to be a non–ideal choice to create a sinusoidal intensity modulation. If one takes into account the AOM deflection characteristics, however, this modulation becomes reasonable. Figure 25 shows the deflected intensity over AOM carrier level, i.e. the envelope of the modulation function. For low envelope levels this function is parabolic, so the envelope of the intensity is $|\sin(2\pi\widetilde{\nu}_{\mathrm{ab}}t)|^2 = (1+\sin(2\pi(2\widetilde{\nu}_{\mathrm{ab}})t))/2$. For low deflection levels—which are likely for example for samples with low damage threshold—this modulation shows superior shape compared to eq. (6.1). The mixing scheme in the original Austin setup results in an intensity modulation with strong contribution of higher harmonics.

The calibration measurement has also been simplified. Instead of using an additional calibration AOM, the artificial modulation is now directly applied to the probe AOM during the calibration measurement. Because this is only a slight modulation on top of the standard carrier level, the frequency is not doubled like at the minimum of the parabola. To achieve the same result, the frequency doubling needs to be performed digitally.

6.4. Biexciton decay in colloidal PbS/CdS quantum dots

The investigation of PbS/CdS QDs spin–coated on silicon nitride waveguides[37] was a collaboration with colleagues from the University of Ghent. The spin–coating fabrication technique is ideal for easy prototype preparation, but lacks the high mode overlap of waveguide and QDs achieved by embedding the QDs into the waveguide. The resulting modulation depth is therefore comparatively

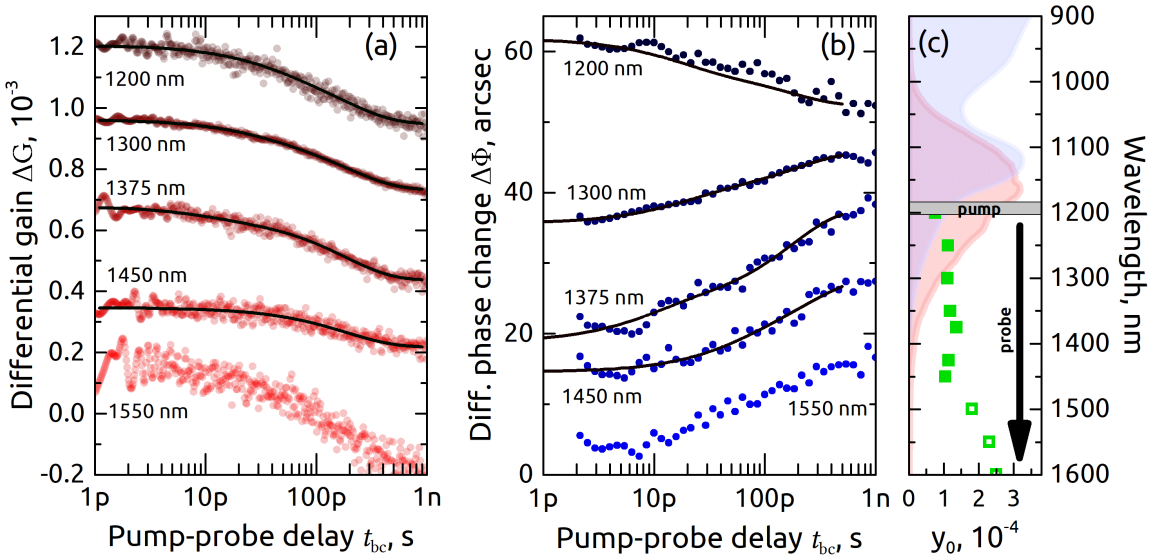

Figure 26: Variation of the probe photon energy with pump wavelength fixed at 1200 nm. Amplitude data in (a) and phase data in (b) are well described by a two–exponential fit (eq. (6.4)). (c) The distribution of pump (grey bar) and probe (green dots) wavelengths in the context of absorption (blue area) and emission (red area) spectra. Similarly published in Ref. 4.

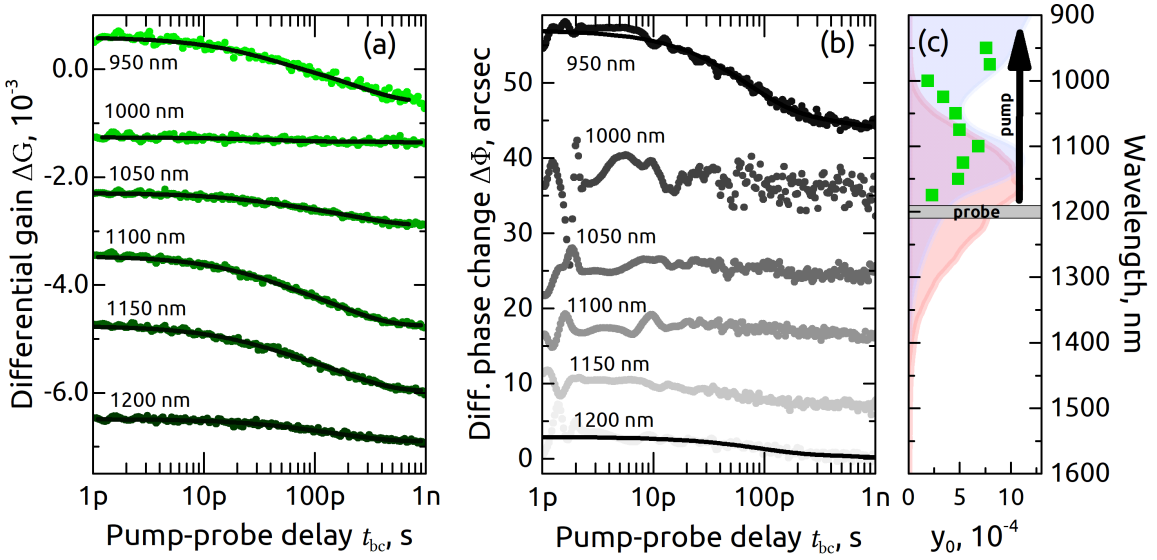

Figure 27: Variation of the pump photon energy analog to the data shown in fig. 26. Similarly published in Ref. 4.

low which made this set of experiments an ideal test field for the sideband PP technique. A detailed description of the sample and the results is given in ref. 4. These results are outside the context of the investigation of SOAs discussed in part III. They are therefore presented here as a proof–of–principle for the sideband PPtechnique. The experiments have been conducted primarily by Christian Ulbrich and Bastian Herzog.

Figure 26(a) and (b) show representative traces of the time-resolved differential transmission in amplitude and phase, respectively, detected by sideband PP spectroscopy with the pump close to the center of the QD luminescence at 1200 nm, and the probe tuned from 1200 nm to 1600 nm, well in the QD bandgap. The experimental data are shown as solid dots. Note that all PP traces are shown on a logarithmic time scale. For early times, oscillations arising from acoustic noise are visible and are not resolved for later times due to undersampling. The average laser power before the waveguide was 100 µW, with an incoupling efficiency of 10 % this equals 10 µW average power or an energy of 150 fJ per pulse. As the repetition rate of the laser exceeds the decay rate of the QD GS exciton of approximately 1 µs by far, we create a quasi-constant GS exciton population.[31] The transmission and refractive index changes induced by the pump pulse on the picosecond to nanosecond time scale thus reflect not the dynamics of a single GS exciton, but rather the interaction of multiple exictations in the system. Throughout the whole investigated range of probe wavelengths, we observe consistently a positive change of the differential transmission, caused by state filling created by the pump pulse on the quasi-static exciton background. The amplitude change is largest at a red detuning of about 50 nm to 75 nm from the pump pulse, consistent with the Stark shift expected in this kind of QDs. In the differential phase response, we observe a change in sign between 1200 nm and 1250 nm probe wavelength, indicative of the crossing of a resonance. This supports the assumption that carriers are created within the GS manifold of the PbS/CdS QDs rather than in an intraband process, as in this case no particular resonance feature is expected. The data taken at 1550 nm and 1600 nm probe wavelength show a larger noise and artificially higher amplitude, as the probe laser power had to be increased due to decreasing sensitivity of the detector and an exceedingly small diffraction efficiency of the AOM at these long wavelengths. The signature, however, is distinctly positive even at these wavelengths unlike for kHz excitation.[35] This does not exclude the presence of an intraband absorption process, however, this process is not modulated along with the pump modulation under our quasi-cw excitation conditions.

To extract more quantitative information, we fit the traces with a biexponential decay

$$y(t_{\mathrm{bc}}) = y_0 + A_1 \exp(-t_{\mathrm{bc}}/\tau_1) + A_2 \exp(-t_{\mathrm{bc}}/\tau_2), \tag{6.4}$$

which describes the experimental curves well over three orders of magnitude in time. It is important to mention that amplitude and phase data are required. Using only the amplitude data, a stretched exponential model would fit as well, not giving clear evidence of the presence of two distinct processes. The data at 1550 nm and 1600 nm probe wavelength are not fitted because of the signal-to-noise issues mentioned above. Also for the phase data taken at 1500 nm probe wavelength, a meaningful fitting was not possible. The fits are shown in the figure as solid lines. The fast and slow time constants are in the range of 30 ps to 40 ps, and 200 ps, respectively. We did not observe a significant offset in the phase data, while in the amplitude the quasi-static background amounted to up to one quarter of the total signal. The amplitude offset is displayed in fig. 26(c) together with absorption and emission spectra and the wavelength settings of pump and probe pulses.

Figure 27(a) and (b) show exemplary data obtained at pump wavelengths between 1200 nm and 950 nm for a fixed probe wavelength at the QD luminescence maximum at 1200 nm. Again, we observe a consistently positive signal with a maximal amplitude in the response at a blue detuning

of 50 nm to 75 nm of the pump wavelength with respect to the probe wavelength. At shorter pump wavelengths, the response decreases in amplitude, to reappear at wavelengths shorter than 1000 nm as the excited state continuum of the QDs is addressed. With the low number of carriers created, also the phase response is low between 1200 nm and 1000 nm excitation wavelength. This is also reflected by the variation in magnitude of the quasi-static amplitude offset y_0 displayed in fig. 27(c). Biexponential fits of the pump-probe traces are shown in fig. 27(a) and (b) as solid lines. For a range of phase traces, a meaningful fitting of the data was not possible due to an insufficient SNR at arcsecond phase amplitudes.

6.5. Pathways for future development

Multiband detection promises several experiment configurations and improvements to existing experiments that we have not yet implemented. To protect those ideas from being forgotten, I would like to add them here as suggestions for later experiments:

Temporal overlap determination in PP experiments. So far, we always determined the temporal overlap of PP experiments from the PP curve itself. This is not very accurate and might fail totally, if the probed state is not addressed by the pump and the scattering processes are slow. By additionally tracking the pump carrier band $\widehat{\nu}_{\mathrm{ab}}$ it would be easy to determine the temporal overlap exactly. Scanning the pump delay t_{bc} over the static reference delay $t_{\mathrm{cd}} \equiv 0$ resembles a MOLCH measurement. The amplitude maximum locates the temporal overlap.

AC bias induced sidebands. One interesting option might be the generation of sidebands via the electrical carrier injection. For example it would be interesting to combine the sideband and the FROSCH technique. Using a bias tee, it would be possible to supply a constant bias as usual and to combine it with an alternating voltage for sideband generation. In the sideband FROSCH signal, only those light modes would contribute that experience a population modification in the SOA upon a variation of the particular direct current (DC) level. With that experiment and under comparison with the respective ASE change, it might be possible to calculate the absolute DOS distribution.

7. Two–dimensional coherent spectroscopy with white pulses

The observation of FWM signals was an important aspect of the original heterodyne setup,[70] but it has not been used in the setups presented in the previous chapters. This will change at this point. Additional to the FWM observation, we have developed all the necessary "ingredients" to set up an MDCS which is actually nothing else but a phase–resolved FWM measurement under variation of multiple delays. These ingredients are:

- From the FROSCH concept we take the sub–wavelength resolution by interferometric position control.
- SMPM plays an important role for maintenance of phase stability.
- Multiband detection reaches a new level when up to four different bands in two input signals are observed simultaneously (up to six lock–in signals).
- We use a Toptica FemtoFiber pro SCIR fiber laser system with two independently tunable outputs. The white light pulses provided by this system are used without intentional spectral cutting, the spectral width of both pulses exceeds 200 nm.

The resulting 2DCS setup is presented in fig. 28. We refer to this method as Supercontinuum–based Two–dimensional Observation of Radiation Coherence by Heterodyning (STORCH), where the acronym is the German word for "stork". Considering that a STORCH measurement will dispatch up to six FROSCHs, this name seems highly suitable.

It is noteworthy that with the description giving in the following, the STORCH setup scheme in fig. 28 replaces all former ones, as all the former experiments can be performed without hardware changes.

7.1. Concept of the heterodyne 2D coherent spectroscopy

The preliminary goal of the development of this setup was to investigate SOAs under standard operation conditions, particularly at room temperature and above. In this scenario, any coherent signals will decay within hundreds of femtoseconds. The required scan widths of the delays will therefore not exceed 1 mm.

To understand the signal generation of the heterodyne 2DCS one should have the sketch in fig. 13 in mind. This scheme remains valid, but some restrictions need to be considered here compared to the general scheme. Our approach is so far restricted to two pulses that pass the sample, the former probe and pump pulse, respectively. Just like in the classical FWM,[70,77] we will use the self–diffraction scheme given in fig. 12. Like in that scheme, pulse C will also act as pulse B, but in general, the roles of the pulses can be swapped. The respective FWM bands will appear at $\widehat{\nu}_{\bar{\mathrm{a}}\mathrm{cc}} = 2\widehat{\nu}_{\mathrm{c}} - \widehat{\nu}_{\mathrm{a}}$ and $\widehat{\nu}_{\mathrm{ac}\bar{\mathrm{c}}} = 2\widehat{\nu}_{\mathrm{a}} - \widehat{\nu}_{\mathrm{c}}$. With respect to the white light nature of the laser it is, however, advisable to concentrate on $\widehat{\nu}_{\bar{\mathrm{a}}\mathrm{cc}}$. This frequency represents pulse C that has been diffracted by the transient grating induced by pulses A and C. For pulse C it is ensured that its

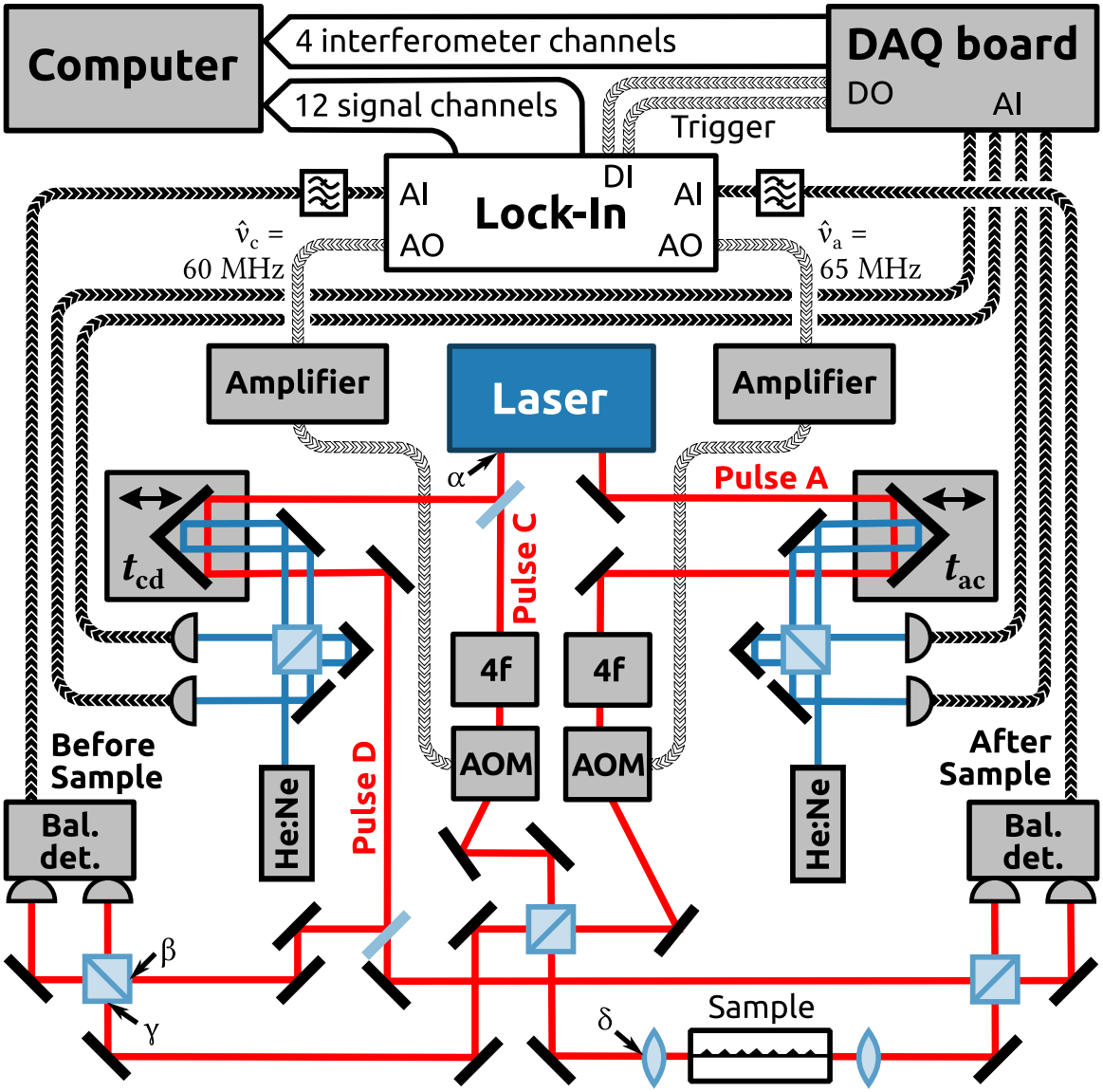

Figure 28: The STORCH setup for 2D coherent spectroscopy. The spots ($\alpha - \delta$) are equivalent with respect to the characterizing FROSCH measurement in front of the sample. Similarly published in Ref. 5.

constituent laser modes are present in the LO, as this has been split off from the same laser arm. The other arm (pulse A) could create modes that are not present in the LO and therefore would not be observable.

The calculation of the 2D spectrum requires the full scan of all combinations $(t_{\mathrm{cd}}|t_{\mathrm{ab}})$. In the present setup, the local oscillator delay t_{cd} is swept rapidly ($\approx 1\,\mathrm{mm/s}$) back and forth while the pump delay t_{ab} is scanned slowly ($< 1\,\mu\mathrm{m/s}$). In fact, every sweep of the reference resembles a single FROSCH measurement with four SMPM. The time axis correction for the 2D scan is, however, more complicated and will be explained in detail in section 7.2.3.

The STORCH measurements will require a comparatively detailed control of the used pulses. The detection capabilities have therefor been extended by a second balanced detection "before the sample". The second arm of the beam–splitter that unites pulses A and C in front of the sample is used to characterize the pulses that enter the sample by FROSCH. The necessary LO is split off from the existing LO beam path by a beam sampler. A careful look at fig. 28 shows, that there is something special about the beam path from spot α at the laser output to spot β on the beam–splitter in front of the new balanced detection: The beam has not passed a single piece of glass. The beam is either reflected by mirrors or by the glass surface of beam samplers. Therefore this beam has been exposed to the minimal amount of dispersion and can be referred to as "the perfect reference". From the perspective of the detector, the spot β where it enters the final beam–splitter is equivalent to spot γ where the characterized beams enter: the same amount of glass is passed subsequently which does not alter the FROSCH trace according to eq. (5.5). In the same way, the spot δ on the in–coupling lens of the sample is equivalent to spots γ from the perspective of the beam–splitter that unites pulses A and C. Thus, based on the relations $\alpha \equiv \beta$ and $\gamma \equiv \delta$, the FROSCH trace detected in the additional balanced detection is equivalent to a FROSCH trace of the pulse at the in–coupling lens referenced with the very original laser output. This FROSCH trace is used in particular to determine the chirp of pulses A and C with respect to the LO. Using the $4f$ pulse shapers, a linear chirp can be compensated efficiently.[91] Just like FROSCH, STORCH is insensitive to the initial pulse phase. At the moment, we do not have the capabilities to pre–characterize the original supercontinuum in amplitude and phase. We need to rely on the sufficiency of its quality.

7.2. Going digital: Changes enforced by the new HF2LI lock–in

The previous description focused on the optics arrangement. But STORCH is much more a matter of data acquisition and analysis. The heterodyne detection scheme in our lab changed tremendously when we were able to purchase the Zurich Instruments (ZI) HF2LI lock–in and some of its add–ons: The "Multi–frequency option", the "AM/FM Modulation option", and the "Real–time option".

7.2.1. Data acquisition and synchronization

With the HF2LI it is not longer necessary to acquire lock–in data via the DAQ board even at high DAQ rates of up to 50 kHz. The HF2LI provides an efficient raw data exchange with the lab computer where a server application makes processed data available. The DAQ board remains, however, still necessary to track the interferometer channels and it offers the opportunity to track other analog signals in the future.

To synchronize the DAQ card and the HF2LI, the DAQ card operates as the master device and generates a digital TTL trigger. The typical SMPM setting of the STORCH measurement has four states. For reasons that will be discussed in section 7.2.3, it turned out to ease the experiment

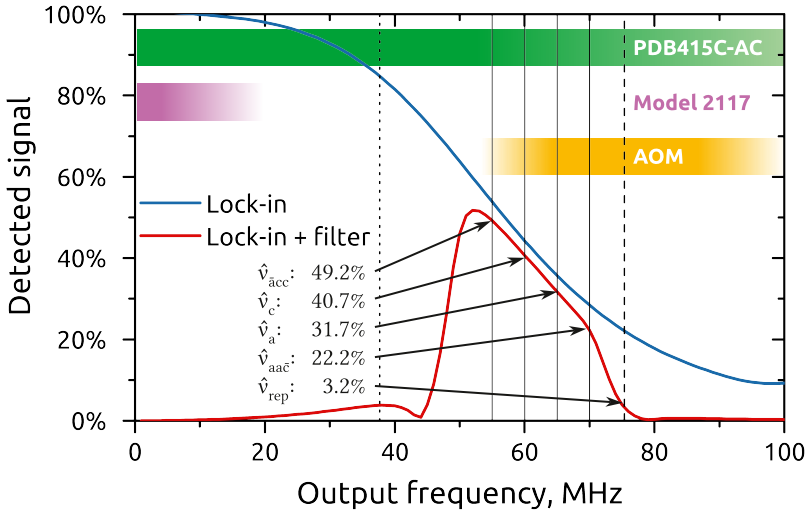

Figure 29: The frequencies used in the 2DCS experiment and the filter transfer functions. The ZI HF2LI has an internal 50 MHz low–pass filter (solid blue). The filter transfer function is determined by directly connecting the lock–in frequency output to the signal input. An additional band–bass filter (solid red) restricts the signal transmission from the detector to the band of used frequencies. The color bars on top indicate the bandwidth of used instruments: The AOMs restrict $\widehat{\nu}_{\mathrm{a}}$ and $\widehat{\nu}_{\mathrm{c}}$, respectively, the PDB415C-AC detector covers the full frequency range and replaced the Model 2117 detector.

control to use two digital triggers that provide four states in binary logic. So the two trigger outputs of the DAQ board are connected to two digital inputs of the HF2LI.

Even though a synchronization of the data acquisition is ensured this way, the data processing is still challenging. In general, large amounts of data are handled (typically at least 320 kB/s) that need to be sorted, stored, and evaluated at run–time. One should avoid to create too many copies of these data, which can easily happen in badly programmed Labview code. Labview *data references* (defined memory space that is writable and readable from different access points) turned out to be an efficient way to deal with this problem. A limited set of such data references are used to sort the data: The lock–in data are requested from the HF2LI server application, but there is, of course, a small latency compared to the DAQ card data points that do not need USB transfer. The first data reference stores the newly acquired data channel by channel. In a next step, the program evaluates how many full SMPM sets (all four data points in all channels) are available in the first stage. These data are transferred from the first to the second data reference and used for the further evaluation.

7.2.2. Lock–in–driven AOMs and frequency choice

Following our traditional heterodyne detection scheme, the simultaneous tracking of $\widehat{\nu}_{\mathrm{c}}$, $\widehat{\nu}_{\mathrm{a}}$, $\widehat{\nu}_{\bar{\mathrm{a}}\mathrm{cc}}$, and $\widehat{\nu}_{\mathrm{ac}\bar{\mathrm{c}}}$ would require at least two reference inputs to lock to $\widehat{\nu}_{\mathrm{c}} - \widehat{\nu}_{\mathrm{rep}}$ and $\widehat{\nu}_{\mathrm{a}} - \widehat{\nu}_{\mathrm{rep}}$. The ZI HF2LI lock–in, however, does not provide more than two fast analog inputs that in our setup are occupied by signal channels. The effective frequency range would therefore be restricted to less than 2 MHz, which on the other hand would restrict the sampling rate and the according delay stage speed.

To overcome this restriction, the ZI HF2LI itself is used as the frequency generator to drive the AOMs. Locking to an external frequency is not necessary in this case, but the frequencies need

to be chosen within the AOM bandwidth (60 MHz to 100 MHz with a steep deflection efficiency drop–off below 60 MHz). The demodulated frequency is now no longer the beating of a shifted mode superposed with its neighboring mode ν', but with its original mode ν instead. The New Focus Model 2117 balanced detectors (bandwidth 10 MHz) used so far were replaced by Thorlabs PDB415C-AC (bandwidth 100 MHz). As the ZI HF2LI is a 50 MHz lock–in (210 MS/s), this forces us to operate the device beyond its specification. We chose $\widehat{\nu}_{\mathrm{c}} = 60\,\mathrm{MHz}$ and $\widehat{\nu}_{\mathrm{a}} = 65\,\mathrm{MHz}$ as a trade-off and under consideration of the two FWM bands appearing at $\widehat{\nu}_{\bar{\mathrm{a}}\mathrm{cc}} = 55\,\mathrm{MHz}$ and $\widehat{\nu}_{\mathrm{ac}\bar{\mathrm{c}}} = 70\,\mathrm{MHz}$, respectively. This choice will favor the desired $\widehat{\nu}_{\bar{\mathrm{a}}\mathrm{cc}}$ band.

Despite undersampling, the driving of the AOMs works well by using a 1.5 W amplifier (Becker Nachrichtentechnik AMP5220031-T). On the detection side, however, both fast inputs are equipped with an internal 50 MHz low–pass filter, so the chosen frequencies are already strongly suppressed. To reduce the analog signal transmission to the used spectral window, an additional band–pass filter (Minicircuits BBP-60+) is placed between detector and lock–in, that particularly suppresses the residual signal of $\widehat{\nu}_{\mathrm{rep}}$. The lock–in TF as well as the combined lock–in and band–pass filter TF are shown in fig. 29.

As one can see, the STORCH setup works at the moment at the very technical limit and in some respect beyond the specifications of the instruments. This implies that there is a wide range of further quality gain whenever better instruments are available.

7.2.3. Phase stability: SMPM implemented by ZI HF2LI Real–Time option

The main challenge of MDCS is the stable tracking of the FWM signal with sub–wavelength resolution over the entire measurement. In the FROSCH setup it was sufficient to use a Michelson interferometer as a time–reference because a single measurement does only take a few seconds and the scan is linear. Thermal drifts of the beam pathways are therefore negligible. In 2D spectroscopy, however, a single measurement takes several minutes. More than that, some kind of zig–zag pattern is necessary to explore the two–dimensional time–area and a consistent data pattern requires the reliable phase relation between nearby points. With respect to the passive stability in our lab, simple Michelson interferometers are not sufficient.

The problem is solved by using pulses A and C itself as additional time–references that are used to eliminate temporal drifts of the pulses. Similar approaches have recently also been chosen by other groups.[92] Of course, a time–reference needs to be constant over the entire 2D pattern, which is not the case when pump and probe pulse are both switched on—coherent as well as incoherent interactions of both pulses would inhibit the use of these signals. Here, the concept of SMPM becomes important: In an SMPM sequence of four points, between two data points with both pulses on, we alternately switch one of the pulses off to retrieve an undisturbed reference for the switched on pulse. For the power configuration $(P_{\mathrm{a}}|P_{\mathrm{c}})$ ($P_{\mathrm{a/c}}$ denote the normalized deflected power level at the respective AOM) we use a repeating sequence $\{(1|1),(0|1),(1|1),(1|0)\}$ to acquire a corresponding signal sequence $\left\{S_k^{(1|1)},S_k^{(0|1)},S_k^{(1|1)},S_k^{(1|0)}\right\}$ ($k \in \{(\mathrm{a},\mathrm{in}),(\mathrm{c},\mathrm{in}),(\mathrm{a},\mathrm{out}),(\mathrm{c},\mathrm{out}),\bar{\mathrm{a}}\mathrm{cc}\}$) at a switching rate of 20 kHz. This rate limits the TC of the lock–in to $\leq 5\,\mu\mathrm{s}$ as the sequentially acquired values need to be completely independent.

The analog implementation of SMPM has been described in section 5.3.1. The ZI HF2LI does not provide an analog scaling input for the frequency outputs, so a fully digital setting of the output levels driving the AOMs is required. The standard version of the ZI HF2LI does not provide the functionality to switch the output signal level upon every data acquisition step. This requires an instrument add–on, the "Real–time option", which enables an onboard processor that is programmable and is able to execute a large number of operations without communication to the

Signal	Acquired by	Det.	Freq.	Demod.	Trigger	Description
$S^{(1\|1)}_{\bar{\mathrm{a}}\mathrm{cc}}$	HF2LI	after	55 MHz	2	1r, 1f	FWM signal channel
$S^{(0\|1)}_{\mathrm{c,out}}$	HF2LI	after	60 MHz	1	2r	Undisturbed pulse C FROSCH signal for t_{cd} calculation
$S^{(1\|0)}_{\mathrm{a,out}}$	HF2LI	after	65 MHz	4	2f	Undisturbed pulse A FROSCH signal for t_{ab} calculation
$S^{(0\|1)}_{\mathrm{c,in}}$	HF2LI	before	60 MHz	3	2r	Pulse C FROSCH signal before sample (for alignment)
$S^{(1\|0)}_{\mathrm{a,in}}$	HF2LI	before	65 MHz	6	2f	Pulse A FROSCH signal before sample (for alignment)
$I^{(\mathrm{inter})}_{\mathrm{LO}}$	DAQ card	interferometer			all	sin/cos signals from reference stage interferometer
$I^{(\mathrm{inter})}_{\mathrm{ac}}$	DAQ card	interferometer			all	sin/cos signals from pump stage interferometer

Table 2: Overview of the data channels. The lock–in channels analyze a certain combination of input detector signals (Det.) and frequencies (Freq.). The demodulator occupation is restricted by the "AM/FM Modulation option". The last demodulator (number 5) is used to track $S_{\mathrm{aa\bar{c}}}$, which is not evaluated at the moment. A trigger "1r" refers to "trigger 1 rising", "2f" to "trigger 2 falling", and so on.

main computer. This makes these operations extremly fast. Typical latencies are in the range of 5 µs to 10 µs. The processor is programmed in C and the compiled program is uploaded to the instrument.

The "Real–time option" is able to execute commands upon the occurrence of defined events. It took us a while to understand that this event is not the digital trigger itself, but the acquisition of a data point. The triggering has in fact two stages: The digital signal from the DAQ card triggers the acquisition of a data point. Subsequently, this acquisition triggers the processor action. In the first stage, the triggering of the acquisition, it is important to trigger only the demodulators that are really necessary. For example, it does not make sense to acquire a data point $S^{(1|0)}_{\bar{\mathrm{a}}\mathrm{cc}}$ which corresponds to a FWM signal with pulse C switched off. Here, the two trigger channels provided by the DAQ card are important. The triggers rise and fall alternating at every DAQ card acquisition event, which results in a sequence: 1r, 2r, 1f, 2f. Here, "1r" is for "trigger **1 r**ising", for example. The complete acquisition sequence is displayed in table 2.

7.2.4. Scanning procedure and Fourier transformation

As a first time base, the interferometer data are analyzed and every data set gets a corresponding time stamp $(t^{(0)}_{\mathrm{cd}}|t^{(0)}_{\mathrm{ab}})$. Based on this time basis we interpolate $S^{(1|0)}_1$ and $S^{(0|1)}_2$ for every FROSCH scan, Fourier transform the interpolated trace, and derive temporal drifts of Δt_{cd} from $S^{(1|0)}_{\mathrm{c}}$ by comparing the phase of the spectral maximum with the respective values of the previous scan. Taking Δt_{cd} into account, Δt_{ab} is calculated in the same manner from $S^{(0|1)}_{\mathrm{a}}$. These drift values are used to correct the time basis $(t^{(0)}_{\mathrm{cd}}|t^{(0)}_{\mathrm{ab}})$ to create the final time basis $(t_{\mathrm{cd}}|t_{\mathrm{ab}})$.

After the correction of the time information, the one–dimensional chain of data is binned into a two–dimensional matrix. The matrix size is chosen as a power of 2 (according to the FFT algorithm) with a spatial bin width of $< 400\,\mathrm{nm}$. For typical measurements, the matrix size is 512×512

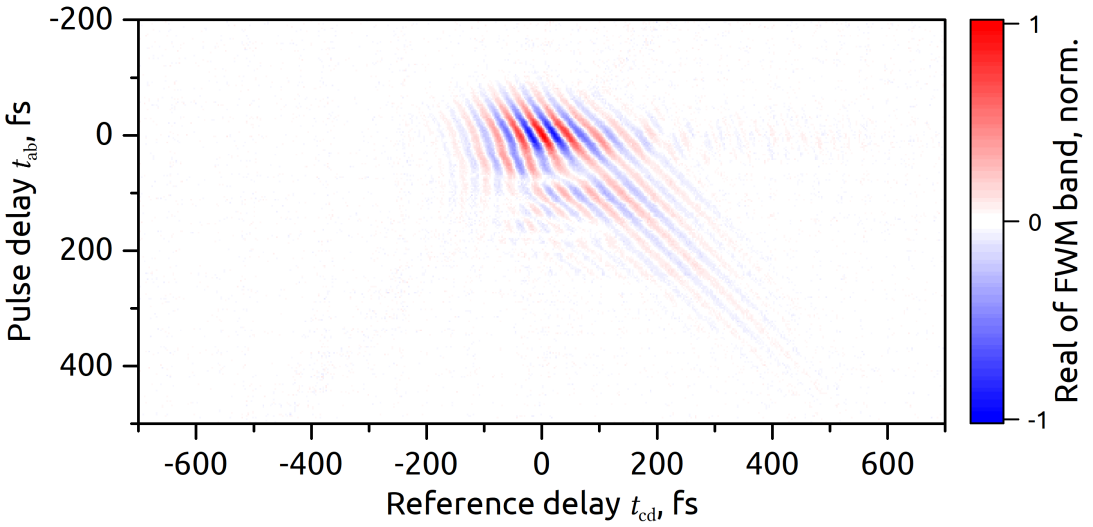

Figure 30: Typical temporal data (real part). The data are presented in a rotating frame of 1200 nm. The relevant data are restricted to a range of < 1 ps around the pump–probe overlap. The FFT of this particular data set is shown in fig. 43.

or 1024×1024. To improve the averaging, the data points are transformed to a rotating frame according to the central wavelength before the binning. An example of the temporal matrix is shown in fig. 30. The standard 2D FFT is applied to the temporal matrix to retrieve the spectra that will be discussed in detail in chapter 11.

One final issue is the phase of the data. According to the coherent nature of the FWM generation, one expects a fixed phase relation between the bands $S_{\bar{\mathrm{a}}\mathrm{cc}}$, S_{a}, and S_{c}. Although this is true, it is hard to determine. For example, not all spectral modes of pulse A might be detectable, as we will discuss in section 11.1.1. In this case, the signal cannot be phase–normalized to this corresponding mode. It turned out to be a reasonable solution to interpret

$$\mathcal{E}_{\mathrm{2D}}(\nu_{\mathrm{a}}, \nu_{\mathrm{c}}) = \mathcal{F}\left\{S_{\bar{\mathrm{a}}\mathrm{cc}}\right\}(\nu_{\mathrm{a}}, \nu_{\mathrm{c}}) \cdot \left(\frac{\mathcal{F}\left\{S_{\mathrm{c}}\right\}(\nu_{\mathrm{c}})}{\left|\mathcal{F}\left\{S_{\mathrm{c}}\right\}(\nu_{\mathrm{c}})\right|}\right)^{-1} \tag{7.1}$$

as the 2D spectrum. The 2D spectrum phase is here displayed with respect to the phase of the respective mode of pulse C. This makes sense, as the FWM beam is created when pulse C is diffracted by the transient grating in the SOA.

7.3. Pathways for future development

Some limitations imposed by the current instruments have already been discussed. Another limiting factor is, in general, the lock–in time constant. It requires from us to wait for several microseconds to acquire a new data point, which results in DAQ rates of $\widetilde{\nu}_{\mathrm{daq}} = 20\,\mathrm{kHz}$. Is it possible to overcome this limitation? And to push $\widetilde{\nu}_{\mathrm{daq}}$ maybe even to the MHz range?

It probably is. The time–constant can be reduced to zero, if a temporal rect-function is used instead of the Butterworth filter discussed in section 1.3.2. As we have seen in fig. 2 (c), this would result in a broad spectral response. However, we can here make use of the fact that the heterodyne bands are extremely narrow and equally spaced. The spectral sinc-function also has equally spaced

zeros—and nothing is better than a zero if you would like to filter a mode out. It is just necessary to establish a proper relation between $\widetilde{\nu}_{\mathrm{daq}}$ and the mode shift frequencies. Additionally, it is even possible to adjust $\widetilde{\nu}_{\mathrm{daq}}$ to the basic sampling rate of the digital instrument. Let us assume a instrument sampling rate of $\widetilde{\nu}_{\mathrm{samp}} = 500\,\mathrm{MHz}$ and a desired DAQ rate of $\widetilde{\nu}_{\mathrm{daq}} = 5\,\mathrm{MHz}$. One DAQ point will represent the FT of 100 original sampling points. We can now choose the AOM frequencies as $\widehat{\nu}_{\mathrm{c}} = 12\,\widetilde{\nu}_{\mathrm{daq}}$, $\widehat{\nu}_{\mathrm{a}} = 13\,\widetilde{\nu}_{\mathrm{daq}}$, and additionally detect at $\widehat{\nu}_{\bar{\mathrm{a}}\mathrm{cc}} = 11\,\widetilde{\nu}_{\mathrm{daq}}$. This results in exactly the same values as we used before. The demodulator at $\widehat{\nu}_{\mathrm{c}}$ would (theoretically) perfectly filter out the bands at $\widehat{\nu}_{\mathrm{a}}$ and $\widehat{\nu}_{\bar{\mathrm{a}}\mathrm{cc}}$ because of the corresponding zeros in the sinc-function.

This acquisition would be 250 times faster than the present one. Of course, this requires an integrated signal generation and analysis device which could fulfill these requirements. And it would bring new challenges to the delay generation, to the data processing, and several other aspects. From the perspective of physics, however, it would be possible to decrease the acquisition time of a full 2D spectrum from 4 min today down to about 1 s. In this case, 2D spectroscopy could even be used as an alignment tool.

Part III.

Investigation of subsystem coupling in the DWELL system

8. The sample

In this chapter, the sample is introduced briefly and some of it basic properties are collected. These are acquired by electrical and linear–optical methods. Several more detailed characteristics of the SOA will be derived from the experiments in the following chapters.

8.1. Sample structure and mounting

The structure used in our experiments is an In(Ga)As-based SOA. The active region contains 15 layers of self-assembled QDs grown by molecular beam epitaxy with a nominal QD density of $\rho_{\mathrm{QD}} = 10^{11}\,\mathrm{cm}^{-2}$. The QDs are immersed in an InGaAs QW in a DWELL structure. The QD layers are separated by 33-35 nm thick GaAs barriers to prevent vertical coupling. The active region is enclosed between p and n doped bulk GaAs (pin-structure). The lateral extension of the active region is 2 µm, the length of the waveguide is 1.5 mm.

The SOA is mounted in a cryostat to enable cooling, although this has not been done throughout this work to protect the SOA from damage. The SOA diode structure is bonded and contacted inside the cryostat. This enables the application of an external bias U and the injection of a current J. At a forward bias of $U_{\mathrm{th}} = 855\,\mathrm{mV}$, the injection threshold is reached. The $J(U)$ characteristics are displayed in fig. 45. In this work, only forward bias was applied. It has been varied from 0 V to 1.78 V, where a maximum injection current of 200 mA was reached. There is no active temperature control implemented, so the SOA is operated under standard operation conditions in all experiments. A shrinking band edge upon carrier injection needs to be considered according to eq. (2.4).

Light is coupled into and collected from the waveguide using aspheric lenses mounted outside the cryostat. The coupling is adjusted by positioning of the lenses in x, y, and z direction. Manually operated micrometer screws were sufficient for alignment throughout the experiments presented here. The waveguide of the shallow etched SOA provides gain guiding, i.e. the propagation of light is favored in the area with high carrier injection. This results in a modification of the waveguide properties upon variation of J. This does not pose a severe obstacle to our measurements. However, the alignment will always be optimized for a particular injection current and will get slightly worse when J is changed. This will be discussed in section 11.1.

8.2. Amplified spontaneous emission

The ASE of the SOA is shown in fig. 31. At low injection, a first peak centered at 1281 nm (967 meV) rises that can be attributed to the QD GS. It can be approximated by a Gaussian with a FWHM of 30 meV. From pump-probe experiments, the GS transparency current is determined to be $J_0 = 5\,\mathrm{mA}$ at 1280 nm. ASE data show that at injection currents above $16J_0 = 80\,\mathrm{mA}$ the GS reaches the maximal inversion and the GS luminescence intensity saturates. Above 40 mA, a second peak becomes visible that is attributed to the ES of the QDs.

Although the peak structure looks rather simple on the first sight, some features hint to a more complicated nature of the energy structure. Figure 31 is taken from Ref. 11, where Benjamin

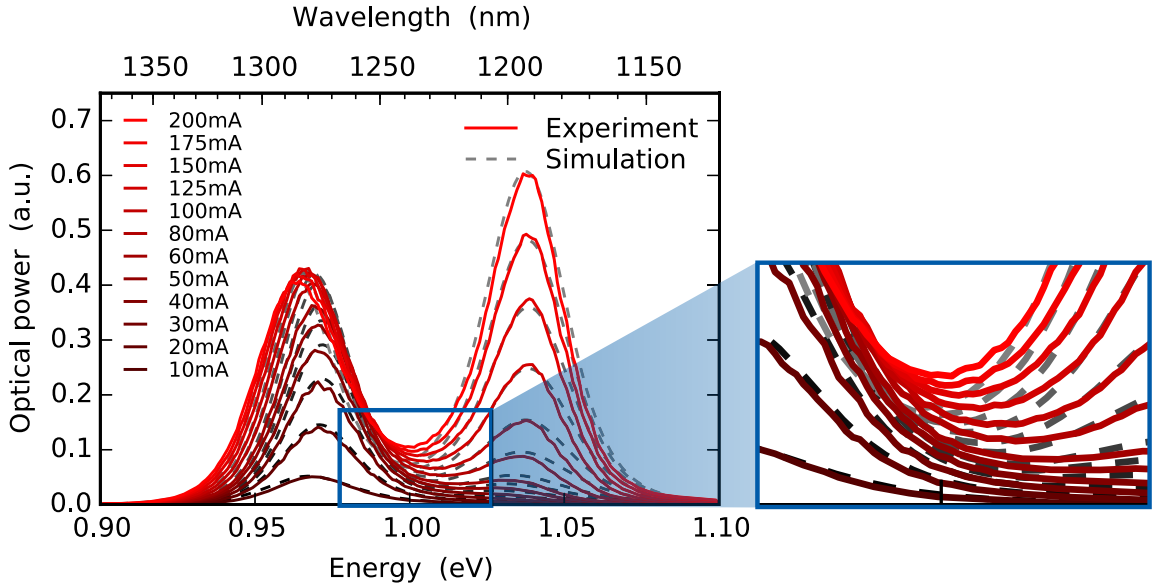

Figure 31: The measured ASE of the SOA (red, solid lines) compared to calculations (dashed gray) performed by Benjamin Lingnau based on Maxwell–Bloch equations.[11]

Lingnau presented a high quality calculation of the ASE based on their Maxwell–Bloch model. Such calculations are complicated, as different QD and QW states contribute to the dielectric function and the resulting radiation is influenced by the DOS as well as the propagation behavior. In fig. 31, a region between GS and ES is highlighted. The calculations always underestimate this particular part of the spectrum. This might be a hint to the presence of a CE, as we will discuss in detail in chapter 10. The ES cannot be approximated by a Gaussian as well as the GS. This might be due to the proximity to the QW, but might also be influenced by the presence of a large number of CEs in this energy range.

9. Rabi Oscillations at room temperature

The coherence time of self–assembled QDs has been extensively studied under various injection and temperature conditions.[78,93,94] At room temperature, the coherence time $T_2 \leq 300\,\mathrm{fs}$ limits the observation of coherent effects to a time range on the order of a single pulse length.[78] In contrast to low temperatures,[77] it is therefore not possible to observe Rabi oscillation in a pump–probe scheme at room temperature.

The modification of the shape of a single pulse caused by Rabi flops, however, has already been predicted in the early days of laser physics.[95] In parallel to our work, other groups also investigated the influence of Rabi oscillations on the pulse shape experimentally,[96] so this field still attracts substantial interest. For data processing applications, also the interaction of pulses in the strong coupling regime will be interesting.[97,98]

9.1. Pulse deformation caused by Rabi flops

From a technical point of view, the development of the FROSCH technique was a challenge on its own, coming along with the change to the fast data acquistion paradigm. While the first physical motivation was the pulse shape modification by ultrafast changes in the gain recovery by reservoir feeding, discussions with Julian Korn and Benjamin Lingnau drew our attention to the impact of Rabi oscillations.

In our lab, the field strength required to force a Rabi cycle below the pulse duration can only be achieved by the Ti:sapphire laser combined with the OPO. The most well–defined 2LS is found at the QD GS, so the OPO wavelength center was chosen resonant to the GS at 1280 nm. The OPO provides high quality Gaussian pulses with a spectral FWHM of 15 nm, which eases the interpretation of pulse shape modifications and the comparison to calculations. The pulse input power measured in front of the SOA in–coupling lens was varied from 1 mW to 12 mW.

The effect of the Rabi oscillations is mainly determined by two experimental parameters: the initial pulse power and the initial GS inversion. Any pulse modification caused by Rabi flops must vanish when the power is lowered and the Rabi cycles exceed the pulse duration. On the other hand, any effect should cancel out at zero inversion. An effective modification is only expected when the majority of QDs contribute from the same initial state (inverted or not inverted) and thereby with the same phase. To isolate the effect of Rabi oscillations from other pulse deformations, these two parameters need to be varied.

In fig. 32 a current series is presented in columns (b-e) and in column (a) the vanishing of the pulse shape modification effect for a low pulse intensity is demonstrated. The upper row contains the amplitude values of the FROSCH signal: Without injection current, in column (b) a significant deviation from the original Gaussian shape is observed. This “bump” disappears in the transparent case in column (c) and reappears for the inverted system in (d). For very high injection currents in column (e), the T_2 time is reduced and the pulse shape modification is less pronounced. The middle row contains the corresponding phase data. A dip in the amplitude is accompanied by a phase shift of π. This behavior is characteristic for any coupled oscillating system as it has been described in section 3.3.2. The GT shown in the lower row will be discussed in section 9.2.

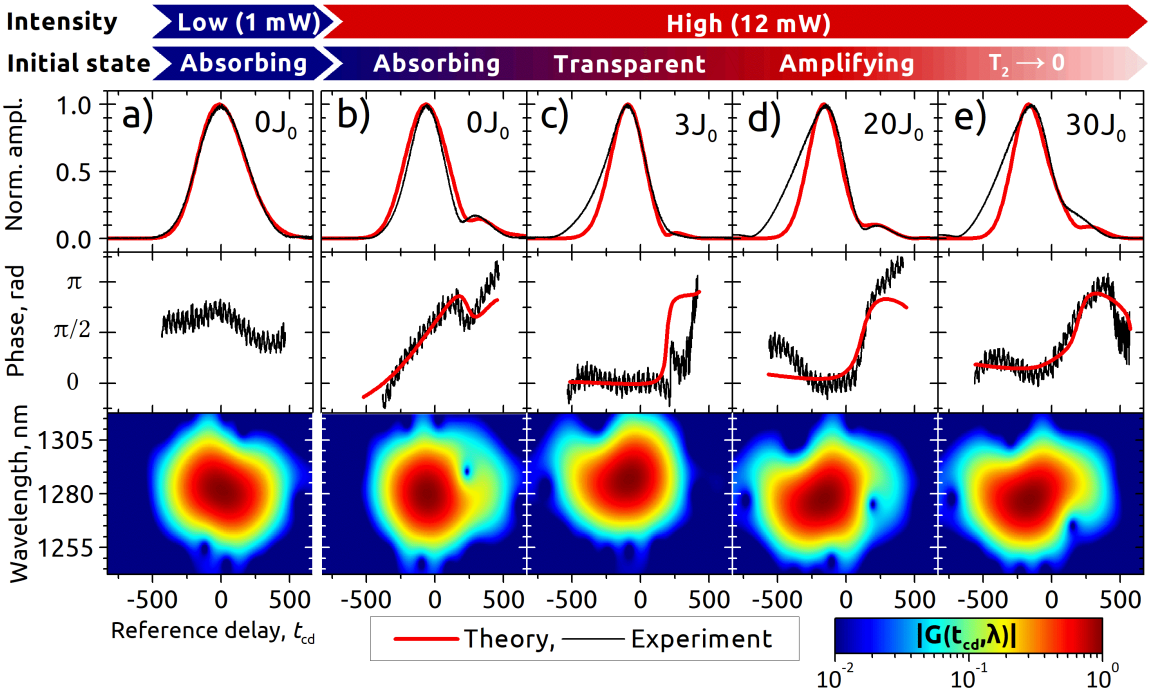

Figure 32: Pulse shape modifications caused by Rabi oscillations. In the upper panel, amplitude data are shown, with experimental data in black and theoretical calculations in red. The middle panel shows the corresponding signal phase. The lower panel displays a GT of the experimental data. The data show the expected behavior upon power and injection current variation: (a) For low pulse power, the Rabi cycle exceeds the pulse duration, no modification is observed. (b) For high power a pulse shape modification is observed in the case of a non–inverted system. (c) Near the transparency current level J_0, the contributions of inverted and non–inverted QDs cancel out. (d) For high injection current with a majority of inverted QDs, the modification reappears. (e) Further carrier injection reduces T_2, the signature fades. Similarly published in Ref. 1.

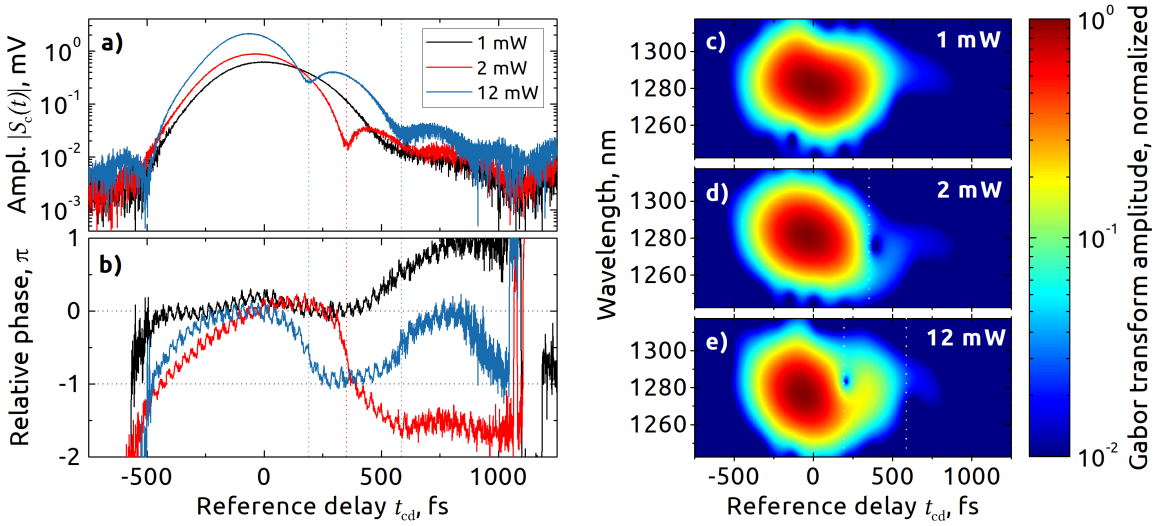

Figure 33: Power dependence of the pulse shape modification induced by Rabi oscillations. (a) The amplitude of the temporal signal on a logarithmic scale and (b) the corresponding phase show typical phase shifts indicating reversed energy flow. (c–e) Also in the GT, the dip moves to earlier times.

The theory values shown in the upper and middle row of fig. 32 as red solid curves are based on calculations performed by Julian Korn and Benjamin Lingnau using Maxwell–Bloch equations (section 3.3.1).[1] The calculations reproduce all the characteristic features and prove that the general statements of the picture of coupled pendula[1] remain valid in an inhomogeneously broadened ensemble and under consideration of propagation effects.[1,99]

In fig. 32 and Ref. 1 the power dependence is not discussed in detail. The original data series included more power steps. A corresponding power series is presented in fig. 33. Dashed lines indicate the phase shift positions. For increasing power, the flop events occur earlier, which is exactly the expected behavior. For the highest input power of 12 mW, even a second phase shift can be observed.

The quality of the phase data in figs. 32 and 33 is limited. In this very early experiment, an additonal plane mirror mounted to the delay stage was used to set up the FROSCH Michelson interferometer. The setup is described in Ref. 1. The velocity of the VT-80 delay stages varied about a factor of 3 upon continous movement. The oscillatory movement induces a relative oscillation of the plane mirror against the retro–reflector of the reference beam, which is read as an oscillation of the phase. In later experiments, the plane mirror was removed and the interferometer beam is now reflected by the same retro–reflector as the reference beam. This leads to much better phase data, see for example in fig. 34.

9.2. Temporal vs. spectral representation

In fig. 32, a GT is displayed in the lower panel. It shows the temporal as well as the spectral distribution of the resulting pulse. A dip in the GT amplitude can be read as an indicator of Rabi oscillations. However, there are some issues that need to be considered as drawbacks of this representation. The GT is not unambiguous, it depends on the choice of the window function as it has been shown in section 1.1.1. This also means that there is no defined position of the dip and

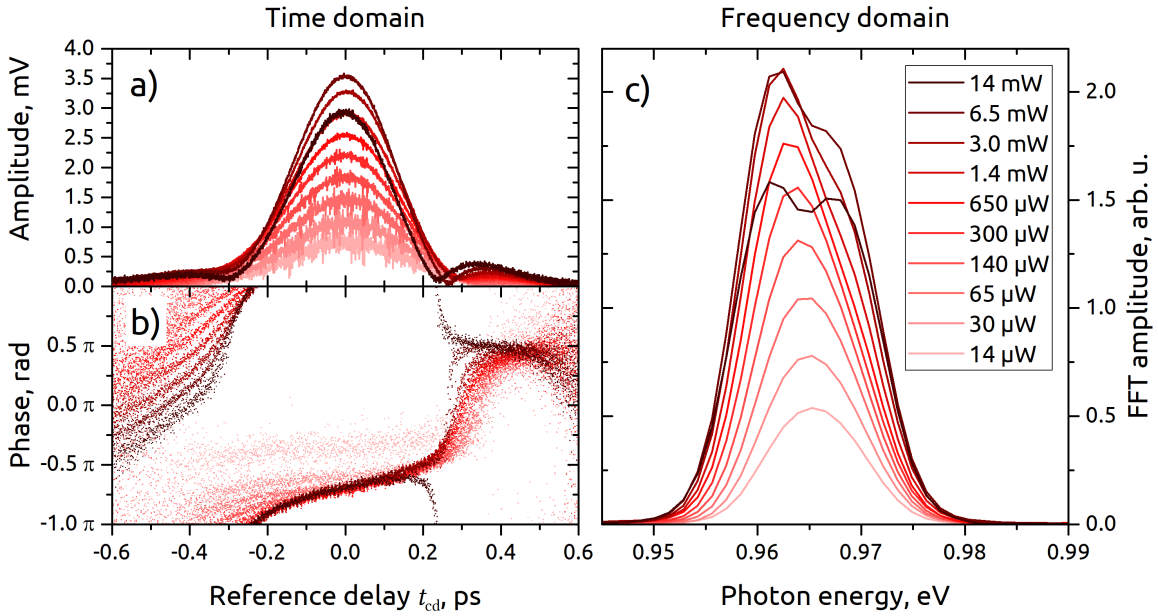

Figure 34: A SMPM measurement of FROSCH traces spanning three orders of magnitude in pulse input power.

therefore one cannot derive physical information from it. And finally, the shown amplitude representation neglects the phase information of the GT, which is in fact hard to interpret. In conclusion, the GT provides the interesting combination of spectral and temporal information, but is limited in providing unchallengeable arguments.

Alternatively, it is also possible to restrict the discussion of FROSCH data either to the temporal data (with the phase indicating qualitative changes as shown above) or to the pure spectral FT data. An example for the spectral interpretation is shown in fig. 34: It is the demonstration of a FROSCH SMPM measurement reproducing some of the results of Ref. 1. The data are acquired in a single scan at an SOA injection current of $J = 80\,\mathrm{mA}$, i.e. at the GS inversion saturation. The SMPM spans a power range of three orders of magnitude, from 14 µW to 14 mW, which—by the way—impressively demonstrates the advantages of field based measurements. A temporal pulse modification can be observed in fig. 34 (a). The interpretation of the modification, however, is not as straightforward as in the data set of Ref. 1 due to a slightly different chirp of the input pulses. The FFT of the FROSCH data shown in panel (b) is much more elucidating. Two effects can be identified if one has in mind that the original pulse is slightly red–shifted with respect to the GS: For low power pulses, the SOA amplification profile dominates the spectral position. With increasing power, the resulting pulse shifts to the red, because the ratio between original power and amplified spectrum increases. When the strong coupling regime is reached, the Rabi splitting[65,100] sets in and becomes dominant for the maximum power of 14 mW.

10. Evidence of Crossed Excitons in pump–probe experiments

Crossed Excitons have been described as a bound state of carriers of mixed dimensionality in section 2.3.4.[62,63] In the DWELL system there are in general two types of CEs that might be observed within the spectral window of our laser system: QD–bulk and QD–QW combinations. For both of them we found experimental evidence, which motivated the further development of the experiments following in chapter 11.

10.1. Crossed Excitons revealed by gain excitation spectroscopy

The original question of the experimental sets presented in this chapter was: How exactly does the QD couple to the QW? Can carriers be captured directly by the QD GS or is a cascading process via the ES[101] necessary? To clarify this, we chose the two-color pump-probe (2cPP) approach with the pump tuned to the QW and the probe tuned to the GS. While the probe was fixed at a wavelength of 1280 nm (0.969 eV), a series of curves is taken with the pump wavelength tuned from 1200 nm (1.033 eV) up to 1070 nm (1.159 eV) in steps of 10 nm. The injection current is varied for each pump wavelength from 0 mA to 200 mA. The original plan was to compare this set of data to an alternative case with the probe tuned to the ES. If the response of the ES would be substantially faster than the response of the GS, this would be a proof of a cascading transfer mechanism.

A selection of PP traces is shown in fig. 35(a). Surprisingly, the response of the GS was already faster than the temporal resolution of the experiment. Looking for a faster ES response in a second measurement series was therefore futile. At this point, one of the tremendous benefits of the fast data acquisition approach that we used here for the first time[†] came into play: the ability to acquire a large number of traces. All the conclusions following in this section are not derived from a single curve, but from the comparison of many curves.

10.1.1. Complexity reduction by linear fitting

The simultaneous handling of many curves enforces the reduction of the traces to appropriate figures of merit characterizing their behavior. For the data in fig. 35(a), two properties of the curves are of special interest: Firstly, the initial change of ΔG, and secondly, whether the traces fall or rise in the subsequent time range. For low injection currents, the rising/falling behavior is characterized by a linear fit in the temporal range of 1 ps to 5 ps. The fit slope is depicted in fig. 35(b) as dots and stars. A change of sign indicates a qualitative change that can be attributed

[†]The actual setup deviated from that shown in fig. 19. In this very early stage, a mechanical chopper replaced the AOM fast switching (this was due to a very slow amplifier in the inherited setup that was removed later on), thus SMPM was not possible. A noteworthy fun fact: This highly important measurement series at the very end of a lab time has almost been devastated by a server malfunction. Just in time we were able to emulate the lost control software by a "Notfallprogramm" (emergency program). This was one experience that motivated the GIT system with local and remote copies.

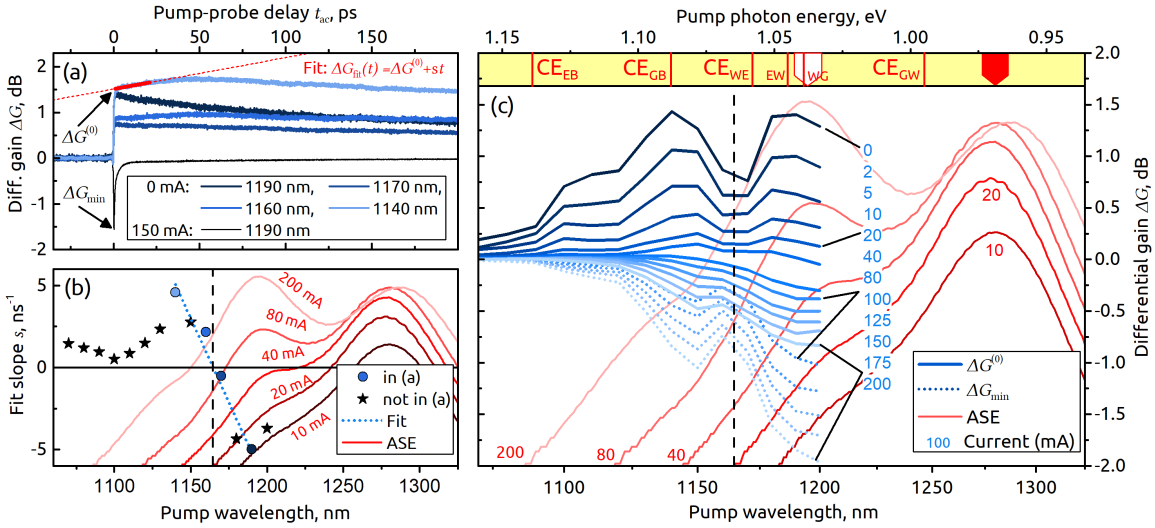

Figure 35: (a) A set of pump–probe traces at pump wavelengths around the QW band edge. (b) The PP trace slope in the range of 1 ps to 5 ps (shown for clarity in the range 1 ps to 20 ps) revealing the QW band edge by a change of sign. (c) Gain excitation spectra (solid bold blue) for varying injection currents. Similarly published in Ref. 2.

to the crossing of the band edge. Pumping above the QW band edge leads to a reservoir filling and a subsequent carrier capture, leading to a rising differential gain in the QD GS in this early time range. Pumping below the band edge only addresses QD related states, so the reservoir is not filled and an immediate decay sets in. The exact determination of the QW band edge to 1164 nm ($E_W = 1.065\,\mathrm{eV}$) according to the zero crossing of the fit of the PP trace slopes is an important step in the characterization of the SOA that could not be extracted from the ASE spectrum.

Besides the fit slope, also the fit intercept $\Delta G^{(0)}$ provides important information. It represents the differential gain excited immediately in the GS. As we were able to resolve this excitation spectrally by means of the large number of pump wavelengths, we referred to the analysis method as *gain excitation spectroscopy*. The result is shown in fig. 35(c) for all injection currents*, together with the ASE and the QW band edge determined before. For low injection currents, there is a positive excited gain, for high injection currents this changes to a gain depletion. The change of sign, however, does not correspond to the GS transparency current of 5 mA but does rather occur around 50 mA. Two peaks can be determined above the QW band edge especially for low injection currents. These peaks remain visible for higher currents and show a well–explainable current dependence: They shift to lower energies for high injection currents according to the sample heating and the lower energy peak changes its sign at a lower current than the higher energy peak. Below the band edge, a peak is visible that corresponds well to the ES ASE. $\Delta G^{(0)}(0\,\mathrm{mA})$ is slightly shifted to higher energies with respect to the ASE at 200 mA, which excellently agrees with the Varshni shift caused by the heating of the SOA under current injection. These dependencies are an indicator for the high quality of the data.

Indicated in fig. 35 (a) and displayed in fig. 35 (c) as dotted lines, there is a second quantity that shows a similar pattern: the minimum value ΔG_{min} of the differential gain at the pump–probe overlap. The minimal value can be determined by two factors. Firstly, a real gain depletion and

*As the "Notfallprogramm" lacked automization, the planned measurement at 60 mA has simply been forgotten in the manual setting routine.

Symbols					Energy, eV				
	$E_{\mathrm{G,e}}$	$E_{\mathrm{E,e}}$	$E_{\mathrm{W,e}}$	$E_{\mathrm{B,e}}$		0.707	0.757	0.777	1.029
$E_{\mathrm{G,h}}$	E_{G}		E_{WG}	E_{BG}	-0.262	0.969	1.019	1.039	1.291
$E_{\mathrm{E,h}}$		E_{E}	E_{WE}	E_{BE}	-0.281	0.988	1.038	1.058	1.309
$E_{\mathrm{W,h}}$	E_{GW}	E_{EW}	E_{W}		-0.288	0.995	1.045	1.065	1.317
$E_{\mathrm{B,h}}$	E_{GB}	E_{EB}		E_{B}	-0.381	1.088	1.139	1.158	1.410

Table 3: First approximation of Crossed Exciton energies according to eq. (10.2).

a subsequent re–filling of the depleted states. Secondly, there might be also a contribution of coherent interaction effects, often referred to as "coherent artifact". The latter contribution cannot be identified using a static reference delay t_{cd}. The analysis of such contributions will be done in the 2DCS experiments in chapter 11. Here, however, the similarity of the patterns of $\Delta G^{(0)}$ and ΔG_{min} is another indicator for the consistency of the measurements.

10.1.2. Crossed Excitons or Upper State?

The hypothesis of transitions from QD states to continuum states has already been extensively discussed in my diploma thesis.[102] An alternative explanation, however, would be the existence of an "upper state" as it is assumed in several rate equation models.[103,104] In this picture, the found structure would be solely related to quantum dot states. In a first interpretation of the peak shapes in fig. 35, this approach seemed plausible: The line width roughly mimics the inhomogeneous broadening of the ASE. This contrasted our expectation of a continuous gain excitation, as the involved bulk or QW states have a continuous DOS.

Calculations performed by Sandra Kuhn, however, convinced us to return to the interpretation of bound–to–continuum transitions and CEs.[105] These calculations are performed for intraband–correlations of carriers and the exact calculation of the interband analog is much more complicated, but one central argument applies also to this case: Although the DOS is continuous, the momentum selction rules favor $k = 0$ and therefore the Γ point. This results in a sharp peak in the absorption spectrum. Of course, the resulting peak widths in fig. 35(c) are determined by the homogeneous and inhomogeneous broadening as well as the pump and probe pulse spectral widths.

This does not negate the existence of an upper state. Quite in contrary, our interpretation provides an explanation for the formation of an upper state that is often useful to describe the electron dynamics. The effect is actually the same, which will become more evident in section 10.2.

10.1.3. Approximation of Crossed Exciton energies

The calculation of exact CE energies is beyond the scope of our experimental work. A first approximation of the expected CE energies is based on a strongly simplified picture according to section 2.1.2. We assume a fixed effective mass ratio for electrons and holes of

$$\mathfrak{r} = m_{\mathrm{h}}^*/m_{\mathrm{e}}^* = 2.7, \tag{10.1}$$

neglecting any differences between the subsystems. This value is based on literature values for InGaAs QWs of $m_{\mathrm{e}}^* = 0.071 m_0$ for electrons[106] and $m_{\mathrm{h}}^* = 0.191 m_0$ for holes[107], respectively. We assume a very simple DOS with carrier energies derived from the transition energies of the GS ($E_{\mathrm{G}} = 0.969\,\mathrm{eV}$), the ES ($E_{\mathrm{E}} = 1.038\,\mathrm{eV}$), the QW band edge ($E_{\mathrm{W}} = 1.065\,\mathrm{eV}$), and the

gallium arsenide (GaAs) bulk band edge ($E_{\mathrm{B}} = 1.41\,\mathrm{eV}$ which corresponds to eq. (2.4) and table 1 at $T = 328\,\mathrm{K}$). Single carrier energies are calculated according to

$$E_{i,\mathrm{h}} = -\frac{E_i}{1+\mathfrak{r}} = -\frac{E_i}{3.7} \tag{10.2a}$$

$$E_{i,\mathrm{e}} = E_i - E_{i,\mathrm{h}} \tag{10.2b}$$

and CE energies are given by the energy difference

$$E_{ij} = E_{i,\mathrm{e}} - E_{j,\mathrm{h}} \tag{10.3}$$

with $i, j \in \{\mathrm{B}, \mathrm{W}, \mathrm{E}, \mathrm{G}\}$. The respective energies and the resulting CE energies are summarized in table 3. Eight CE energies are calculated for combinations of 0D and 2D/3D states. Six of them are in the observation range of our presented gain excitation spectroscopy (only E_{BG} and E_{BE} exceed this range). In general, all of them would be in the spectral range of the FemtoFiber pro SCIR laser. A large spectral separation between pump and probe pulse, however, complicates the alignment (the SOA is strongly absorptive for higher QW energies, even under maximum carrier injection) and worsens the simultaneous in–coupling due to chromatic aberration.

These energies and this derivation will serve for the energetic localization of CEs throughout the following chapters. Several aspects are completely neglected, e.g. the influence of semiconductor doping on the relative shift of subsystem band edges. Moreover, as the two projects developed independently, the calculations following in section 10.2 are partially based on different literature values.[3,108] This is, however, not very important. The real challenge of understanding the complex system without feeding in parameters will be tackled in chapter 11.

Attributing Crossed Excitons to the gain excitation spectra

The CE energies are depicted in fig. 35(c). The two dominant peaks at energies above the QW band edge can be attributed to $\mathrm{CE_{GB}}$ and $\mathrm{CE_{EB}}$, respectively. In the context of our work, this is the first experimental evidence of optical transitions of mixed dimensionality, in this case pumping an electron from the GaAs VB to the QD CB in the non–inverted case. Although this might seem very unlikely, one needs to consider that there is only a very limited set of allowed transitions in that specific energy range that affect the QD immediately. Without electrical injection, no intra–band absorption is possible, and even with injection current it would contribute only gain depletion.

Right below the band edge, a large number of possible transitions is found. The direct QD ES is accompanied by $\mathrm{CE_{WG}}$, $\mathrm{CE_{EW}}$, and $\mathrm{CE_{WE}}$. This large number of potential configurations and the rapidly changing spectral gain profile caused by the proximity of the QW band edge raise the question, how purely the ASE ES peak can be attributed to the QD ES transition. If the above–band–edge CEs have such an impact on the gain excitation spectra, do the below–band–edge CEs not need to contribute in a similar way to the luminescence? Actually, this question will not be answered in the following. But it needs to be kept in mind whenever thinking about the interpretation of ASE spectra.

10.2. Carrier dynamics in a DWELL system

The existence of CEs will change the mechanisms of electron dynamics tremendously. The question might not only be the one raised in the very beginning of section 10.1: Are the subsystems coupled via a cascading process or via a direct capturing? The question is also: Are correlated carriers captured simultaneously or do CEs offer an intermediate pathway that allows a stepwise

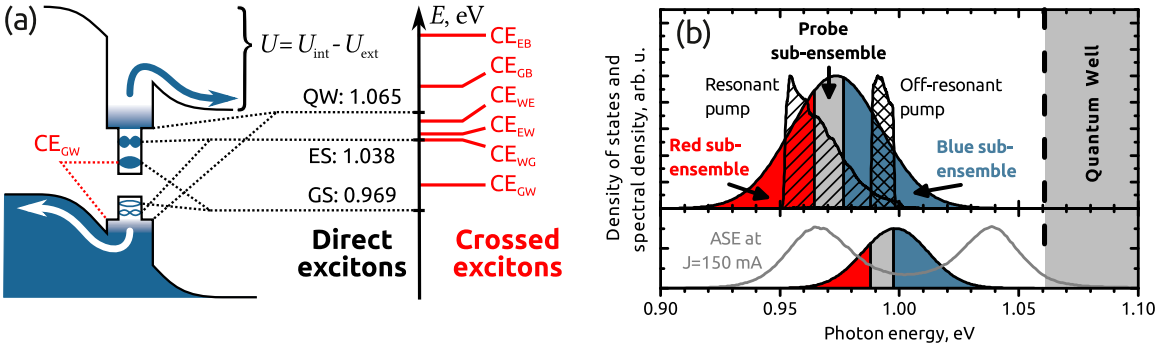

Figure 36: Concept of the diffusion experiments. (a) All experiments are performed for low forward bias below the carrier injection threshold. Carriers are created in the QDs, thermally activated, and extracted by the band bending potential. (b) The GS ensemble is split in three subensembles with respect to the probe pulse spectral width: A resonant subensemble, a lower energy subensemble ("red subensemble"), and a higher energy subensemble ("blue subensemble"). Similarly published in Ref. 3.

Parameter	Resonant	Off-resonant
Maximum power $P_{\max}$	1.35 mW	128 µW
Probe spectrum red limit	964 meV	965 meV
Probe spectrum blue limit	977 meV	975 meV
Pump spectrum red limit	951 meV	988 meV
Pump spectrum blue limit	998 meV	998 meV
Number of bias levels	18	22
Number of SMPM power levels	5	4
Total number of curves	90	88

Table 4: Parameters of the two experimental series, resonant and off-resonant, respectively. Spectrum limits denote energies at which the spectral density drops below 5 % of the maximum value. The spectral distribution of pump pulses is illustrated in fig. 36 (b).

capturing—maybe even without breaking the carrier correlation? In this context we designed an experimental setting that addresses two main aspects: How do CEs in general modify the inter–dot diffusion and how do CEs in the GS spectral range contribute to the optical excitability?

The diffusion dynamics is directly related to the spatial localization of carriers around the QDs. Considering CEs, there is a much larger number of localized states beyond the six exciton states of GS and ES. The observation of localization requires isolated carriers. This excludes electrical carrier injection that creates a random non–equilibrium distribution of carriers. The experiments in this section are therefore performed at forward bias, but below the carrier injection threshold. The corresponding potential scheme is shown in fig. 36 (a). This is the solar–cell configuration of the *pin*–structure, so the results will be of particular interest for photovoltaic applications.[109]

The question of optical excitability governs the spectral choice of pump and probe pulses. These considerations are sketched in fig. 36 (b). The probe is centered to the ASE GS maximum and defines the "probe sub–ensemble". The QDs with lower GS transition energy form the "red subensemble", those with higher energy the "blue subensemble". The experiments comprise two series with respect to the pump pulse spectrum: The resonant series addresses the probe subensemble directly.

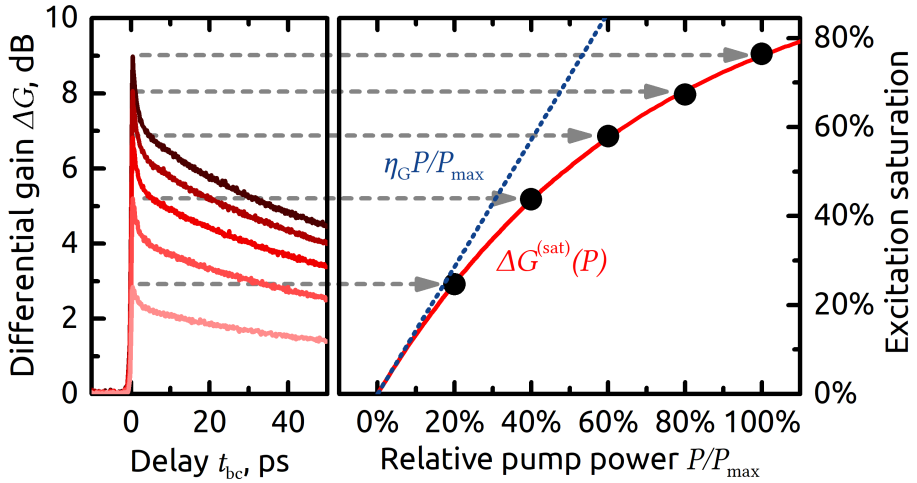

Figure 37: Left: An exemplary set of data, taken from the resonant series at $U = 750\,\mathrm{mV}$. Right: A plot of peak amplitude versus pump power (level visualized by dashed arrows) shows a saturation well described by eq. (10.4). Similarly published in Ref. 3.

For the off–resonant series, the pump spectrum is tuned to the spectral range where $\mathrm{CE_{GW}}$, the lowest energy CE, is expected. So the off–resonant series addresses the blue subensemble as well as the $\mathrm{CE_{GW}}$ of the probe subensemble. To identify the degree of saturation, which is necessary to determine the ratio of GS and CE excitation, the SMPM technique is applied. In fig. 37 the excitation saturation of GS pumping is shown for an exemplary set from the resonant series. With linearly increasing pump power, the data show a clear saturation behavior that is well-described by the function

$$\Delta G^{(\mathrm{sat})}(P) = \Delta G^{(\mathrm{max})} \left(1 - \exp\left(-\left(\frac{\eta_\mathrm{G}}{\Delta G^{(\mathrm{max})}}\right) P/P_{\mathrm{max}}\right)\right) \tag{10.4}$$

with $\Delta G^{(\mathrm{max})} = (11.8 \pm 0.3)\,\mathrm{dB}$, $\eta_\mathrm{G}/\Delta G_{\mathrm{max}} = 1.43 \pm 0.06$ and the maximum power $P_{\mathrm{max}} = 1.35\,\mathrm{mW}$ $(18.0\,\mathrm{pJ/pulse})$ for this particular experiment. If we compare fig. 37 to fig. 20, we do not observe a significant contribution of TPA in fig. 37.

10.2.1. Numerical model

For a quantitative analysis of the data, we construct a rate equation model composed of the QD and a surrounding 2D continuum. A direct comparison in Refs. 110 and 111 of QDs with surrounding QW and such without even a wetting layer showed the decisive role of the QW in the inter-dot coupling. The qualitative change of decay behavior upon variation of the extraction potential

$$U_{\mathrm{extr}}(U) = U_{\mathrm{th}} - U \tag{10.5}$$

observed in fig. 38 (b) can be displayed in terms of an instantaneous time constant analog to eq. (2.10):

$$\tau_G(t_{\mathrm{bc}}) = -\frac{\Delta G(t_{\mathrm{bc}})}{\partial_{t_{\mathrm{bc}}} \Delta G(t_{\mathrm{bc}})}. \tag{10.6}$$

The instantaneous time constants for respective ranges of 15 ps are displayed in fig. 39 (a). It shows a constant decay rate for high U_{extr} and a linear growth of the time constant for low extraction.

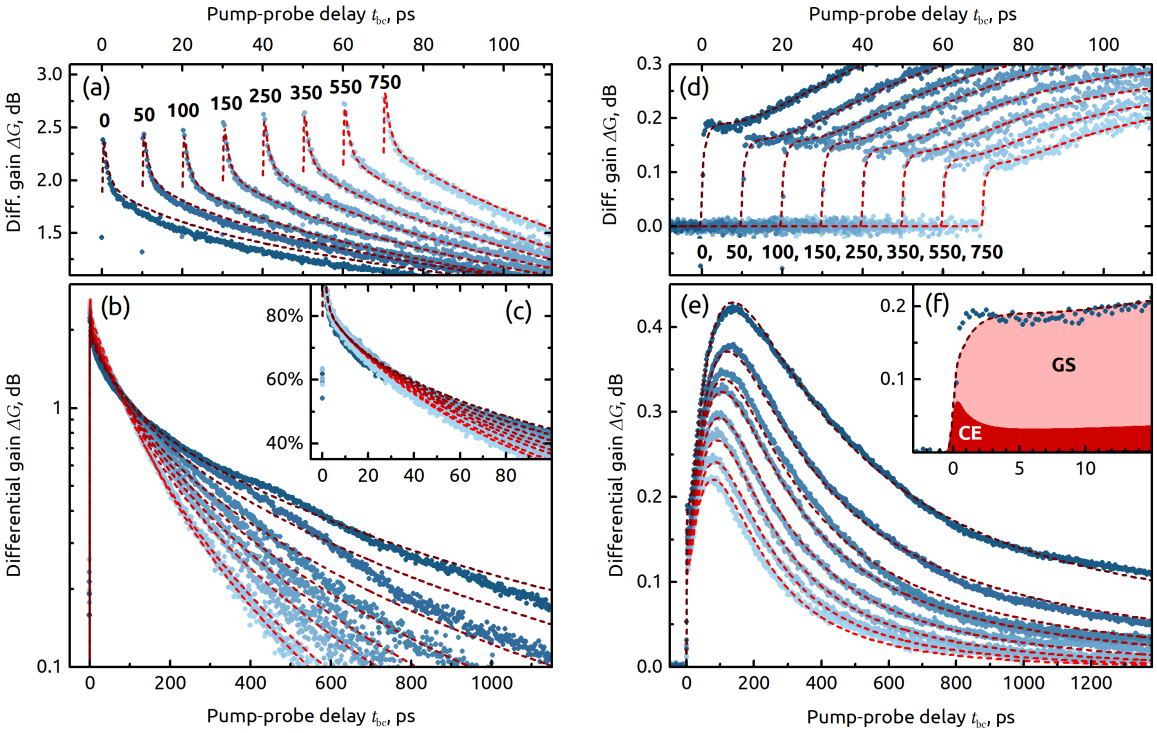

Figure 38: Pump–probe data sets demonstrating carrier diffusion. Experimental data are shown as blue dots, calculations based on rate equations according to section 10.2.1 as red dashed lines. Light colors indicate high extraction potential (full band bending), dark colors low extraction potential (compensated band bending). Bold numerals indicate the extraction potential U_{extr}. The resonant series is shown in the left panel (a-c), the off–resonant series in the right panel (d-f), respectively. Similarly published in Ref. 3.

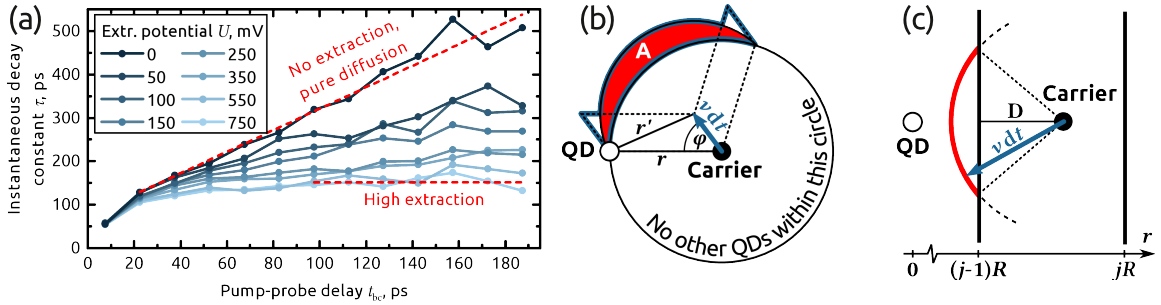

Figure 39: Identification of diffusive carrier transport and implementation in the model. (a) Instantaneous decay constants $\tau_{\mathrm{G}}(\tau)$ according to eq. (10.6) for the resonant pump-probe series at different extraction potentials, calculated from linear fits for 15 ps time ranges. The dashed (red) lines represent linear fits of the limiting cases of zero and high extraction. (b) The transition probability to other QDs is proportional to the number of QDs in area A, which is approximated in eq. (10.17) as the area with bold (blue) contour. (c) Inward diffusion probability within one sub-ensemble is proportional to the solid (red) fraction of the circle.

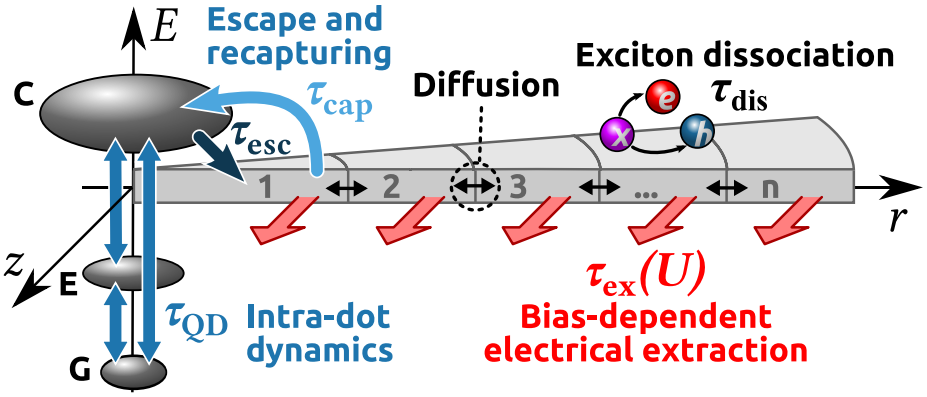

Figure 40: The basic scheme of states for the rate equation model. Each QD is represented by three states: The GS (G), the ES (E), and an averaging CE state (C). The QW continuum is represented by a chain of bins ($1 \ldots n$), each of them representing a ring centered at the QD. Several transitions, feeding, and extraction processes are implemented by time constants. Similarly published in Ref. 3.

This linear growth is expected for diffusive processes. We assume, without knowing the particular transfer mechanism, that the effective mathematical form of the carrier motion in 2D is the one of a diffusion process (section 2.3.3). We thus model the QD as a three-level system, and for the QW we assume an unstructured continuum in which we implement a random walk process for the particles with Boltzmann-distributed thermal velocities.

We use a linear differential equation system according to eq. (2.6) and the description in section 2.3.3. While this approach would not be sufficient to describe a QD-SOA in general, the specific experimental conditions described above make it applicable: Here, every excitation is created in the GS of a spatially isolated QD, for most quantum dots a single exciton or no exciton at all is created (random biexcitons will be neglected). In this case, excitations are very dilute and exciton-exciton interactions can be neglected. Most of all, the absence of other carriers allows to treat fermions like bosons, without concerns about state filling. The calculations are carried out using Scilab 5.5.1.

States

The fundamental scheme of the rate equation model and the allowed transitions between the states are illustrated in fig. 40. The scheme is designed to take into account the spectral distribution of the states within the inhomogeneously broadened QD ensemble, different behavior of paired and unpaired carriers as well as different degrees of confinement. Instead of consecutive numbering we will use a triplet (jkl) to identify these three features, respectively, and to address the elements $N_{jkl,\xi}$ of $\boldsymbol{N}$, which is nevertheless a column vector. The fourth index $\xi \in \{\mathrm{res}, \mathrm{off}\}$ for resonant and off-resonant experiment will only appear if it is necessary to distinguish between the two experimental series, and will be omitted otherwise for simplicity. For the elements of transition matrix Γ we use the notation $\Gamma^{jkl}_{\iota\kappa\lambda}$ for the element in column (jkl) and row $(\iota\kappa\lambda)$, i.e. a transition from (jkl) to $(\iota\kappa\lambda)$ for positive entries. All elements of Γ not mentioned explicitly below are zero.

Confinement

By the first index $j \in \{\mathrm{G}, \mathrm{E}, \mathrm{C}, 1, \ldots, n\}$ the quantum dot or 2D continuum state is identified. The QD is represented by a three-level scheme, containing the QD GS (G), the QD ES (E), and a generalized CE state (C). Note that the manifold of CE states available for equilibration contains all possible CE states, while the only CE state energetically accessible for optical excitation is the lowest state ($\mathrm{CE_{GW}}$, see fig. 36). The numbered states represent the two-dimensional continuum into which the QD is embedded. In-plane radial symmetry allows to model the 2D continuum in a 1D representation: Each of the n continuum states represents a ring of width R and outer radius jR, $j \in \{1, ..., n\}$, centered at the QD. The model for the continuum dynamics is explained in detail in section 10.2.1. The different states of the system have different degeneracy: While the sizes of GS $N_{\mathrm{G}}^{(\max)} = 1$ and excited state $N_{\mathrm{E}}^{(\max)} = 2$ are fixed, the size of the crossed exciton state $N_{\mathrm{C}}^{(\max)}$ is determined as a fit parameter. No specific size is attributed to continuum states, as explained below.

Spectral ensemble

The second index $k \in \{\mathrm{r}, \mathrm{p}, \mathrm{b}\}$ identifies the relative energy of the spectral sub-ensemble. Relative to the experimental probe pulse spectra, the QD ensemble is split into three sub-ensembles (fig. 36(b), details in section 10.2.1). The central part of the QD ensemble is the probe sub-ensemble (p), it represents a fraction of d_{p} of the QDs. QDs with lower GS energies are represented by the red sub-ensemble (r) with size d_{r}, those with higher energies by the blue sub-ensemble (b) with size d_{b}, with $d_{\mathrm{r}} + d_{\mathrm{p}} + d_{\mathrm{b}} \equiv 1$. For the QD GS ensemble we assume a Gaussian distribution for the density of states:

$$D(E) = \exp\left(-\ln 2 \left(\frac{E - E_{\mathrm{G}})}{\sigma_{\mathrm{G}}/2}\right)^2\right) \tag{10.7}$$

centered at E_{G} and a FWHM of σ_{G} (see. fig. 36 (b)).

Particle type

Finally, the particle type is given by the third index $l \in \{\mathrm{x}, \mathrm{e}, \mathrm{h}\}$ for excitons (x), unpaired electrons (e) or unpaired holes (h). Of course, unpaired carriers cannot occupy CE states, so the state $j = \mathrm{C}$ does not exist for $l \in \{\mathrm{e}, \mathrm{h}\}$.

Transitions

Every state (jkl) is placed at a specific position E_{jkl} on the energy scale. The GS energies of excitons ($j = \mathrm{G}, l = \mathrm{x}$) are determined as weighted average of the Gaussian ensemble distribution in eq. (10.7). We assume $E_{\mathrm{E}k\mathrm{x}} = E_{\mathrm{G}k\mathrm{x}} + 70\,\mathrm{meV}$ which can be read directly from the ASE spectra (fig. 31) and

$$E_{\mathrm{C}k\mathrm{x}} = E_{\mathrm{G}k\mathrm{x}} + 100\,\mathrm{meV}. \tag{10.8}$$

Equation (10.8) reflects the estimation of a weighted average for all CEs based on the knowledge that E_{GB} and E_{EB} exist above QW band edge (chapter 10) and the assumption that all other CEs also provide states. All continuum states are located at $E_{\mathrm{W}} = 1.061\,\mathrm{eV}$. For electrons and holes, ground and excited state energies ($j \in \{G, E\}$) are set to fulfill the condition $E_{jk\mathrm{e}} = (\mathfrak{r} E_{jk\mathrm{x}} + E_{\mathrm{W}})/(\mathfrak{r} + 1)$ and $E_{jk\mathrm{h}} = (E_{jk\mathrm{x}} + \mathfrak{r} E_{\mathrm{W}})/(\mathfrak{r} + 1)$, respectively.

In our model, the probability for upward transitions ($E_{\iota\kappa\lambda} > E_{jkl}$) is reduced by the Boltzmann factor

$$\Theta_{\iota\kappa\lambda}^{jkl} = \exp\left(\frac{E_{jkl} - E_{\iota\kappa\lambda}}{k_\mathrm{B}T}\right) \tag{10.9}$$

with Boltzmann constant k_B and temperature $T = 300\,\mathrm{K}$. Downward transitions are not modified ($\Theta_{\iota\kappa\lambda}^{jkl} \equiv 1$ for $E_{\iota\kappa\lambda} \leq E_{jkl}$).
For intra-dot transitions between the states G, E, and C, we assume a time constant of $\tau_\mathrm{QD} = 2\,\mathrm{ps}$.[112,113] The matrix elements for intra-dot transitions are under consideration of degeneracy:

$$\Gamma_{\iota lm}^{jlm} = N_\iota^{(\max)}\Theta_{\iota lm}^{jlm}/\tau_\mathrm{QD} \tag{10.10}$$

for $j, \iota \in \{\mathrm{G}, \mathrm{E}, \mathrm{C}\}, j \neq \iota$.
Transitions are allowed between the QD and continuum state 1. An exciton transits between QD state C and continuum state 1, so escape from the QD and capturing into the QD can be considered as a stepwise process only applying to one of the constituent carriers at a time, similar to the carrier capture via indirect excitons observed at elevated temperatures in Ref. 114. A state size $N^{(\max)}$ is not introduced explicitly for the continuum and therefore the degeneracy is included in the time constants τ_esc for escape and τ_cap for capture, respectively. The matrix elements are given by

$$\Gamma_{\mathrm{C}k\mathrm{x}}^{1k\mathrm{x}} = \Theta_{\mathrm{C}k\mathrm{x}}^{1k\mathrm{x}}/\tau_\mathrm{cap}, \tag{10.11}$$

$$\Gamma_{1k\mathrm{x}}^{\mathrm{C}k\mathrm{x}} = \Theta_{1k\mathrm{x}}^{\mathrm{C}k\mathrm{x}}/\tau_\mathrm{esc}. \tag{10.12}$$

Since unpaired carriers $l \in \{\mathrm{e}, \mathrm{h}\}$ do not have a CE state, the continuum state 1 is coupled to states G and E with the same time constants:

$$\Gamma_{jkl}^{1kl} = \Theta_{jkl}^{1kl}\left(\frac{N_j^{(\max)}}{N_\mathrm{G}^{(\max)} + N_\mathrm{E}^{(\max)}}\right)/\tau_\mathrm{cap}, \tag{10.13}$$

$$\Gamma_{1kl}^{jkl} = \Theta_{1kl}^{jkl}/\tau_\mathrm{esc}. \tag{10.14}$$

for $j \in \{\mathrm{G}, \mathrm{E}\}$.

Diffusion

In our model, we picture the lateral inter-dot carrier transfer as a consecutive process involving thermal ejection from a QD, subsequent diffusion in the QW, and capture by a QD. Tunneling between dots or the formation of QD molecules is unlikely at the given dot density, which corresponds to an average inter-dot distance of 30 nm.[115,116] The diffusion of carriers in the 2D continuum and the transition from one spectral sub-ensemble to another is modeled in terms of simple geometrical considerations illustrated in fig. 39(c,d). Carriers are treated as particles with masses $m_\mathrm{e}^* = 0.041m_0$ for electrons and $m_\mathrm{h}^* = 0.465m_0$ for holes.[108] The exciton mass is simply considered to be $m_\mathrm{x}^* = m_\mathrm{e}^* + m_\mathrm{h}^*$. The particles move at thermal velocities given by the Boltzmann distribution

$$F_l(v)\mathrm{d}v\,\mathrm{d}\varphi = \frac{m_l^* v}{2\pi k_\mathrm{B}T}\exp\left(-\frac{m_l^* v^2}{2k_\mathrm{B}T}\right)\mathrm{d}v\,\mathrm{d}\varphi. \tag{10.15}$$

Every carrier is assigned to its nearest QD. Other QDs are assumed to be distributed homogeneously in the 2D continuum according to nominal QD density ρ_QD. A carrier transits from one QD to another if it is closer to a different QD after a motion of time interval dt (fig. 39 (b)). In this moment, the distance to new and old nearest QD is equal, so the ring number j is conserved. The

carrier starts at a distance r from its present QD in a direction given by angle φ to a new position at distance

$$\begin{aligned} r' &= \sqrt{(v\,\mathrm{d}t\,\sin\varphi)^2 + (r - v\,\mathrm{d}t\,\cos\varphi)^2} \\ &\approx \sqrt{r^2 - 2\,r\,v\,\mathrm{d}t\cos\varphi}, \end{aligned} \tag{10.16}$$

where we used $v\,\mathrm{d}t \ll r$. The transition probability is equal to the number of QDs in the (red) filled area A, which can be approximated as

$$\begin{aligned} A(r, v, \varphi) &= |\varphi|(r'^2 - r^2) + 2\,r\,v\,\mathrm{d}t\,|\sin\varphi| \\ &= 2\,r\,v\,\mathrm{d}t(|\sin\varphi| - |\varphi|\cos\varphi) \end{aligned} \tag{10.17}$$

with $\varphi \in [-\pi, \pi]$. By integrating over all directions and velocities, the transition matrix element becomes

$$\begin{aligned} \Gamma^{jkl}_{j\kappa l} &= d_\kappa \rho_{\mathrm{QD}} \int_{v=0}^{\infty}\int_{\varphi=-\pi}^{\pi} \mathrm{d}v\,\mathrm{d}\varphi\,F_l(v)\frac{A(r, v, \varphi)}{\mathrm{d}t} \\ &= d_\kappa \rho_{\mathrm{QD}} \sqrt{\frac{32\,k_{\mathrm{B}}T}{\pi m_l^*}}\,r \end{aligned} \tag{10.18}$$

with $k, \kappa \in \{\mathrm{r}, \mathrm{p}, \mathrm{b}\}, k \neq \kappa$ under consideration of sub-ensemble size d_k.

To derive the probability to move inward from ring $j \in \{2, ..., n\}$ to the next inner ring $j - 1$ within the same sub-ensemble, we consider a carrier at distance D from the ring border (fig. 39 (c)). The probability to cross the border is given by $p(v, D) = (\arccos\frac{D}{v\mathrm{d}t})/\pi$ for $D \leq v\,\mathrm{d}t$, and $p(v, D) \equiv 0$ otherwise. Integration over all velocities and points of the ring yields

$$\begin{aligned} \Gamma^{jkl}_{(j-1)kl} &= \frac{2(j-1)}{(2j-1)R\mathrm{d}t}\int_{v=0}^{\infty}\mathrm{d}v\,F_l(v)\int_{D=0}^{R}\mathrm{d}D\,p(v, D) \\ &= \frac{2(j-1)}{(2j-1)R}\sqrt{\frac{2\,k_{\mathrm{B}}T}{\pi m_l^*}} \end{aligned} \tag{10.19}$$

where we used that the carrier distance from the QD is approximately constant at $(j-1)R$.

An analogous calculation yields the outward diffusion matrix element for $j \in \{1, ..., (n-1)\}$. Moving away from the nearest QD also increases the probability to reach the area of another QD. Since outward movement becomes inward movement from the viewpoint of the new QD in this case, we assume that a carrier that changes the sub-ensemble actually does not diffuse outward any more, therefore we reduce the matrix element by the result from eq. (10.18):

$$\Gamma^{jkl}_{(j+1)kl} = \frac{2j}{(2j-1)R}\sqrt{\frac{2\,k_{\mathrm{B}}T}{\pi m_l^*}} - \sum_{\kappa\neq k}\Gamma^{jkl}_{j\kappa l}. \tag{10.20}$$

This matrix element also determines the necessary number of rings n that is given by $\Gamma^{nkl}_{(n+1)kl} \leq 0$.

Extraction and decay

So far, only off-diagonal elements of Γ have been discussed. All the processes described above conserve the number of particles in the system. Additionally, we included several decay processes into the numerical model, which annihilate particles or dissociate excitons into unpaired carriers. First,

excitons in all states are subject to recombination determined by an average recombination time constant τ_{rec}. Furthermore, excitons in the 2D continuum dissociate with a time constant τ_{dis} and create an unpaired electron and hole. In the continuum states, also the extraction potential U_{extr} extracts unpaired carriers from the system and single carriers from excitons with a time constant τ_{ex}, the latter meaning the annihilation of an exciton and simultaneous creation of an unpaired carrier. Therefore we find another off-diagonal element for $l \in \{\mathrm{e}, \mathrm{h}\}$ that represents intrinsic and potential-induced exciton dissociation, respectively, for continuum states $j \in \{1, \ldots, n\}$:

$$\Gamma^{jk\mathrm{x}}_{jkl} = \tau^{-1}_{\mathrm{dis}} + \tau^{-1}_{\mathrm{ex}}(U). \tag{10.21}$$

Thus, the diagonal-elements of exciton continuum states become

$$\Gamma^{jk\mathrm{x}}_{jk\mathrm{x}} = -\left(\sum_{(\iota\kappa\lambda)\neq(jk\mathrm{x})} \Gamma^{jk\mathrm{x}}_{\iota\kappa\lambda} \right) - \tau^{-1}_{\mathrm{rec}} + \tau^{-1}_{\mathrm{dis}}, \tag{10.22}$$

where the term in parentheses sums the corresponding off-diagonal elements for particle number conservation and the last term compensates the double appearance of the first term of eq. (10.21) in this sum (two unpaired carriers are created by dissociation, but only one exciton is annihilated). For excitons $l = \mathrm{x}$ in quantum dot states $j \in \{\mathrm{G}, \mathrm{E}, \mathrm{C}\}$ only recombination applies:

$$\Gamma^{jk\mathrm{x}}_{jk\mathrm{x}} = -\left(\sum_{(\iota\kappa\lambda)\neq(jk\mathrm{x})} \Gamma^{jk\mathrm{x}}_{\iota\kappa\lambda} \right) - \tau^{-1}_{\mathrm{rec}}. \tag{10.23}$$

Unpaired carriers $l \in \{\mathrm{e}, \mathrm{h}\}$ cannot recombine, so extraction is the only decay channel in the continuum $j \in \{1, \ldots, n\}$

$$\Gamma^{jkl}_{jkl} = -\left(\sum_{(\iota\kappa\lambda)\neq(jkl)} \Gamma^{jkl}_{\iota\kappa\lambda} \right) - \tau^{-1}_{\mathrm{ex}}(U) \tag{10.24}$$

and no decay channels apply for the quantum dot states $j \in \{\mathrm{G}, \mathrm{E}, \mathrm{C}\}$:

$$\Gamma^{jkl}_{jkl} = -\left(\sum_{(\iota\kappa\lambda)\neq(jkl)} \Gamma^{jkl}_{\iota\kappa\lambda} \right). \tag{10.25}$$

Optical interaction

As a last step, optical pumping and probing have to be implemented, where pumping means setting an initial state $\boldsymbol{N}^{(0)}_{\xi UP} = \boldsymbol{N}_{\xi UP}(t = 0)$ and probing means the derivation of a gain curve $G_{\xi UP}(t)$ from the solution $\boldsymbol{N}_{\xi UP}(t)$ of eq. (2.6) for every experimental series $\xi \in \{\mathrm{res}, \mathrm{off}\}$, extraction potential U_{extr} and optical pump power P. The calculation is based on two parameters, the optical GS response η_{G} and the optical $\mathrm{CE_{GW}}$ response η_{C}, respectively. Both parameters are allowed to depend on U, η_{C} additionally depends on P, to reproduce dependencies in experimental transition probabilities. Table 5 summarizes the subsets of data used to determine η_{G} and η_{C}. If one of them is not determined explicitly for a curve, it is interpolated from the parameters of other curves.

The optical GS response η_{G} governs the peak height in the resonant experiment series (fig. 37). According to eq. (10.4), we determine $\Delta G^{(\max)}_U$ and $\eta_{\mathrm{G},U}/\Delta G^{(\max)}_U$ from the SMPM power dependence of the resonant experiment series for every U_{extr}. Since these fit parameters are strongly interdependent, we will discuss the product $\eta_{\mathrm{G},U}$ as the optical GS response.

The model for the conversion of light to population follows the spectra shown in fig. 36(b). The spectral limits of the probe sub-ensemble, $\nu_{\mathrm{Gp},\xi}^{(\mathrm{min})}$ and $\nu_{\mathrm{Gp},\xi}^{(\mathrm{max})}$, are set where the spectral density of the probe pulse drops below 5% of the maximum value (see table 4). From the measured pump spectra we derive the spectral photon density $\Phi_\xi(\nu)$. According to this distribution, the initial population is set to

$$N_{\mathrm{G}k\mathrm{x},\xi UP}^{(0)} = \Delta G_U^{(\mathrm{max})} \int_{\nu_{\mathrm{G}k,\xi}^{(\mathrm{min})}}^{\nu_{\mathrm{G}k,\xi}^{(\mathrm{max})}} \left(1 - \exp\left(-\left(\frac{\eta_{\mathrm{G},U}}{\Delta G_U^{(\mathrm{max})}}\right) P\Phi_\xi(\nu)\right)\right) D(h\nu)\mathrm{d}\nu, \tag{10.26}$$

$$N_{\mathrm{C}k\mathrm{x},\xi UP}^{(0)} = \eta_{\mathrm{C},UP} \int_{\nu_{\mathrm{C}k,\xi}^{(\mathrm{min})}}^{\nu_{\mathrm{C}k,\xi}^{(\mathrm{max})}} P\Phi_\xi(\nu) D\left(\frac{(\mathfrak{r}+1)h\nu - E_{\mathrm{W}}}{\mathfrak{r}}\right) \mathrm{d}\nu. \tag{10.27}$$

The differential gain for GS probing is calculated as a weighted sum of states from the solution $\boldsymbol{N}(t)$ of eq. (2.6). Only carriers in the probe sub-ensemble contribute to the weighting vector $\boldsymbol{W}$, the marginal overlap with $\mathrm{CE}_{\mathrm{GW}}$ of the red sub-ensemble (fig. 36(b)) is neglected. Unpaired carriers in state G switch a QD in the probe sub-ensemble from absorbing to transparency, this contribution is set to $W_{\mathrm{Gpe}} = W_{\mathrm{Gph}} = 1$. Also crossed excitons in state C of the probe sub-ensemble may switch the GS transition to transparency, if one carrier of the CE is in a QD GS state. Here we assume that 80% of CEs are related to a conduction or valence band GS (20% related to ES are not probed experimentally), so $W_{\mathrm{Cpx}} = 0.8$. An exciton in state G switches a QD from absorbing to amplifying, so it contributes with $W_{\mathrm{Gpx}} = 2$. Considering the bias-dependent optical GS response, the differential gain becomes

$$G_{\xi UP}(t) = \eta_{\mathrm{G},U} \left(\boldsymbol{W} \cdot \boldsymbol{N}_{\xi UP}(t)\right). \tag{10.28}$$

For comparison with experimental data, all simulated curves are convoluted with a Gaussian of 500 fs FWHM to take temporal resolution into account. The model parameters are summarized in table 5. They were fitted to the data by an iterative minimization of squares if not depicted otherwise in the table.

10.2.2. Interpretation of the fit parameters

The numerical model now allows a more detailed discussion of the physical processes in the coupled system. In the resonant case, the excitation decays in three stages. Within the first 3 ps, the exciton distribution relaxes from the GS to a quasi thermal equilibrium (fig. 38 (a)). This proceeds predominantly by intra–dot transitions to the ES and CE state governed by the time constant τ_{QD}. In the intermediate time regime (3 ps to 300 ps) we observe a strong dependence of the population decay on extraction potential. For strong extraction the decay becomes nearly single-exponential since the return probability for excitons that escaped from QDs is strongly reduced. For low extraction, the resulting decay rate decreases due to an increasing probability of re-capture from the continuum. Finally, for $t_{\mathrm{bc}} > 300\,\mathrm{ps}$, the excitation is spatially equilibrated over the entire system and decays at a potential-dependent average rate. Nevertheless, we see a slight reduction of this rate for later times, especially in the high extraction case. As experiment and model agree very well in this aspect, this can be attributed to unpaired carriers that cannot recombine any more. Generally, in our observations, the dynamics is well described by carriers relaxing and diffusing as excitons, rather than as unpaired electrons and holes. In case of fast dissociation and diffusion of unpaired carriers one would expect a strong dependence of the long time behavior on the initial carrier density increasing with the SMPM power level, as re-pairing is necessary for recombination. However, this is not observed. These findings are in contrast to results obtained in PL

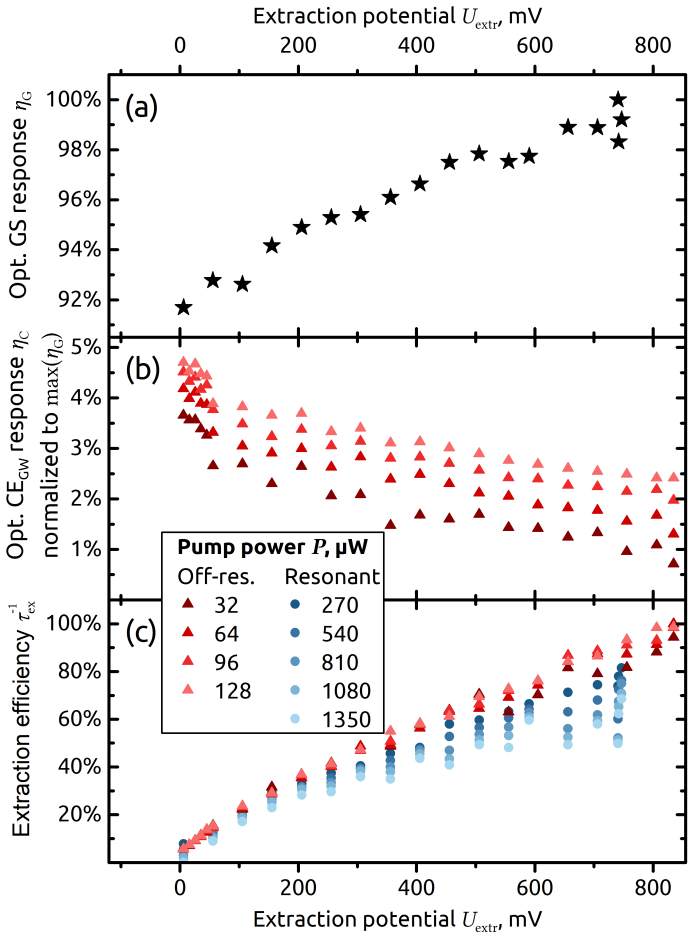

Figure 41: Parameters with potential and power dependence. (a) Normalized optical GS response η_G. (b) Optical CE$_{GW}$ response η_C, also normalized to the maximum of η_G. (c) Extraction efficiency τ_{ex}^{-1}. Efficiency reduction for high pump power can be attributed to compensating fields caused by a large number of extracted carriers. Similarly published in Ref. 3.

Parameter	Value	Source	$t_{\min}$	$t_{\max}$	Lower limit	Upper limit
GS ensemble center E_{G}	973.5 meV	Both	0 ps	∞	(971 meV)	(974.5 meV)
GS ensemble width σ_{G}	44.1 meV	Both	0 ps	∞	44.1 meV	(55.8 meV)
Ring width R	3 nm	(Fixed)				
CE state size $N_{\mathrm{C}}^{(\max)}$	25.9	Resonant	5 ps	15 ps	(0)	
Intra-dot time τ_{QD}	2 ps	(Fixed)				
Escape time τ_{esc}	16.5 ps	(Ref. 3)	50 ps	200 ps	(0 ps)	
Capture time τ_{cap}	49.2 fs	Both	0 ps	100 ps	(0 ps)	
Recombination time τ_{rec}	752 ps	Both	0 ps	∞	(0 ps)	
Dissociation time τ_{dis}	2500 ps	Both	0 ps	∞	(0 ps)	2500 ps
Optical GS response η_{G}	fig. 41(a)	Resonant	0 ps	1.5 ps	(0)	
Optical $\mathrm{CE_{GW}}$ resp. η_{C}	fig. 41(b)	Off-res.	0 ps	10 ps	(0)	
Extraction time τ_{ex}	fig. 41(c)	Both	0 ps	∞	(0 ps)	

Table 5: Overview of model parameters. Except for the last three rows (explained in detail in fig. 41), these parameters are used by all curves. The right hand side of the table depicts fitting details: The fitting routine can be restricted to a certain subset of curves, to a time range $t_{\min} \leq t \leq t_{\max}$, and to upper and lower value limits. For values in parentheses, this limit has not been reached. For τ_{esc}, τ_{cap}, R, and τ_{dis}, a detailed discussion is given in Ref. 3 (fig. 7).

spectroscopy[117] with excitation into the bulk, where carriers were found to behave as independent electrons and holes. Creating carriers with no excess energy in our case maintains the Coulomb correlation, and leads to a dominating excitonic behavior.

The off-resonant experiment yields complementary information from the viewpoint of a spectrally—and as well spatially—different QD sub-ensemble. An immediate response observed for short times indicates absorption by $\mathrm{CE_{GW}}$, as it was intended by the choice of the off–resonant spectral excitation range. Figure 38 (f) visualizes the relative contributions of QD GS and all CEs according to eq. (10.28). At longer times, diffusing excitons arrive in the probed sub-ensemble and start filling the GS in the intermediate time regime. The population maximum is reached after 137 ps for $U_{\mathrm{extr}} = 0\,\mathrm{V}$. In the long time regime, the off-resonant experiment behaves like the resonant one due to spatial equilibration.

A deeper insight into the nature of the contributing transitions is gained from the dependence of the parameters presented in fig. 41 on the extraction potential U_{extr} and the pump power P. Of particular interest is the comparison of the optical GS response η_{G} (fig. 41 (a)) and the optical $\mathrm{CE_{GW}}$ response η_{C} (fig. 41 (b)) obtained from the numerical fits to the data. Remarkably, these transitions exhibit an opposite dependence on the extraction potential: While η_{G} is smallest for low U_{extr} and increases continuously for increasing potential, the optical $\mathrm{CE_{GW}}$ response η_{C} is largest for compensated band bending and decreases for increasing U_{extr}. This is a strong indication that GS and $\mathrm{CE_{GW}}$ are indeed different states, as the natural polarization of the QD-QW CE is shown in the literature[62] to be perpendicular to the QD GS transition, hence the opposite response to a polarizing electric field. The observed pump power dependence in fig. 41 (b) could be caused by an excitation-power dependent linewidth broadening of the GS transition,[118] resulting in an increased spectral overlap of pump and probe pulse that becomes non-negligible compared to $\mathrm{CE_{GW}}$ for high power. The vertical offset thus can be attributed to unintended GS pumping.

The efficiency of carrier extraction is an important figure of merit for detectors and solar cells. We quantify it for our system through the parameter τ_{ex}^{-1}, which we determine for every curve

(fig. 41 (c)). The efficiency of extraction increases as the extraction potential aids the charge separation. Strong band bending thus means strong extraction. Interestingly, the extraction efficiency we observe shows at high U_{extr} (low forward bias) also a pump power dependence. For increasing pump power, the data show a reduction of extraction efficiency. Two processes might contribute to this behavior: On one hand, two-photon absorption occurs for high optical power that dominates in the case of low electrical carrier injection (fig. 20), but is present also below threshold. The additional carriers relaxing from higher states would compensate the extraction partially. On the other hand, and more important in our opinion, the larger number of created carriers for higher pump powers will intrinsically compensate the band bending and screen the extraction potential.[119]

11. Direct observation of Crossed Excitons in two-dimensional coherent spectroscopy

The evidence of the existence of CEs collected by PP spectroscopy in chapter 10 seem convincing, but some doubts may remain. For example, the separation of the exciton and CE transitions in fig. 38 (f) does rely on the assumption that the exciton transition is not addressed by the pump pulse. This is a simplification that neglects the homogeneous linewidth of the transitions and several other aspects. As our knowledge on these aspects is limited so far, this simplification was necessary to avoid unfounded speculation.

The primary purpose of the development of the STORCH setup (chapter 7) was to get access to that information. We want to observe the complex interplay of the coupled states and the spectral distribution of optical transitions under operating conditions of the SOA—if possible by white light in a single experiment.

11.1. Alignment and measurement series

Although the fiber laser system provides a broad spectrum that covers much more than the necessary spectral range, there are several restrictions that need to be considered. Firstly, coupling white light into a wave guide will never be easy. Chromatic aberrations of the coupling optics as well as the dispersion of the waveguide are hard to control or to compensate. Secondly, the transmittance of the SOA changes upon variation of the injection current, so a universal alignment might be impossible. Thirdly, we are not able to measure the chirp of the pulses that leave the laser system. Our FROSCH system is able to track the relative chirp accumulated on the table, but the initial chirp remains unknown.

The alignment procedure is based on the maximization of the FWM band $\widehat{\nu}_{\bar{\mathrm{a}}\mathrm{cc}}$. Both pulses, A and C, are coupled into the SOA at the temporal overlap $t_{\mathrm{bc}} = 0$. The pulse bands $\widehat{\nu}_{\mathrm{a}}$ and $\widehat{\nu}_{\mathrm{c}}$, respectively, are monitored before and after the SOA in rapid FROSCH measurements (two scans per second). $\widehat{\nu}_{\bar{\mathrm{a}}\mathrm{cc}}$is additionally monitored after the sample. These five parallel live–mode FROSCH measurements are used for the alignment. The spectral composition of the FWM signal is immediately revealed and the goal of the alignment is usually to create a spectrally broad FWM signal. The FROSCH also reveals the relative chirp with respect to the original laser pulse (section 7.1) and allows a compensation by the respective $4f$ pulse shaper. While the original idea was to minimize the chirp that is detected before the sample, it turned out that a minimization of the output chirp provided better results. In general, there is an enormous number of degrees of freedom for the alignment. We finally focussed on a high and broad FWM level and a minimized output chirp.

11.1.1. Spectral visibility due to sample transmittance

We were not able to find a single alignment that fulfilled all the desires. This resulted in two independently aligned current series: One that was aligned at $J = 0\,\mathrm{mA}$ and the other one at

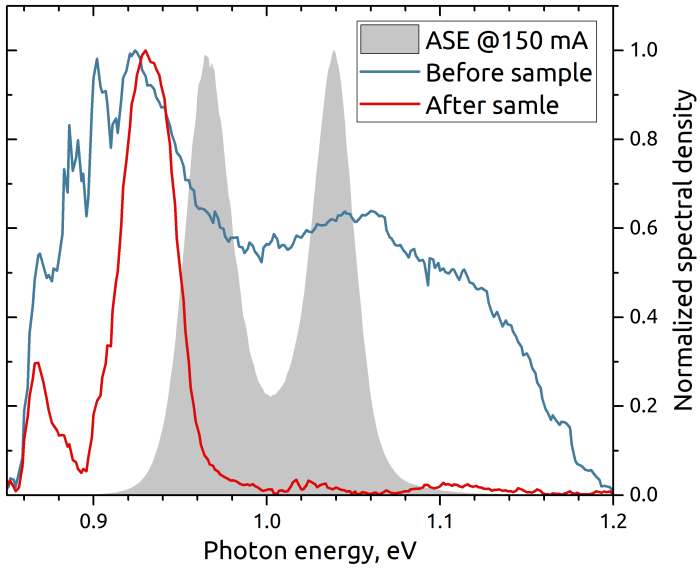

Figure 42: FROSCH spectra of $S_{\mathrm{c}}^{(0|1)}$ before the sample (blue line) and after the sample (red line) in relation to the SOA ASE (grey area). The data correspond to the 2D spectrum in fig. 44 at $J = 0\,\mathrm{mA}$. The QD/QW states are highly absorptive, so the pulse is only transmitted in the band gap spectral range.

$J = 200\,\mathrm{mA}$. In both cases, 2D spectra have been measured under variation of J in the range from 0 mA to 200 mA, with decreasing spectrum quality upon increasing deviation from the alignment value. Although a quantitative comparison of distant features in the 2D spectra is not possible yet, the qualitative distribution of peaks appeared to be static and reliable as far as it is discussed in the following.

In the case of $J = 0\,\mathrm{mA}$, the SOA states are highly absorptive and the transmittance spectrum favors the band gap region. The corresponding FROSCH traces, before (blue) and after (red) the SOA, are displayed for this series in fig. 42. The resulting 2D spectrum for $J = 0\,\mathrm{mA}$ and $U = 0\,\mathrm{V}$ is presented in fig. 43 (detailed discussion in section 11.2). For its interpretation, it is very important to have the transmittance spectrum of the SOA in mind: If the light carrier frequency ν_{c} is not transmitted, there is no resulting signal, neither for the pulse band $\widehat{\nu}_{\mathrm{c}}$ nor for the FWM band $\widehat{\nu}_{\bar{\mathrm{a}}\mathrm{cc}}$. Therefore the 2D spectrum is restricted on the emission axis to the range that is indicated by the red curve in fig. 42. There is no corresponding restriction for the absorption axis. Even though the pulse A might be completely absorbed during the propagation, it might have written its information to pulse C (in the band $\widehat{\nu}_{\bar{\mathrm{a}}\mathrm{cc}}$) in the very first section of the SOA waveguide. So the signal is visible as long as the corresponding light carrier mode ν_{c} is transmitted.

The series aligned at $J = 200\,\mathrm{mA}$ focuses on the range of the QD GS and ES that is entirely amplifying in this current range. For $J < 10\,\mathrm{mA}$, i.e. still above the GS transparency, this alignment did not provide FWM signals above the noise level. The 2D spectrum that corresponds to the alignment current is displayed in fig. 44. Signatures of QD GS and ES are clearly visible along the diagonal. Coupling between GS and ES is indicated by corresponding off–diagonal elements. The coupling appears aligned to the cross–diagonal. This could be a hint to a volume conserving QD growth, i.e. a reciprocal relation of lateral an vertical QD size (section 2.3.2). However, the quality of the off–diagonal feature is not yet fully convincing. This could be clarified by an experiment that reduces the respective spectra to the off–diagonal area.

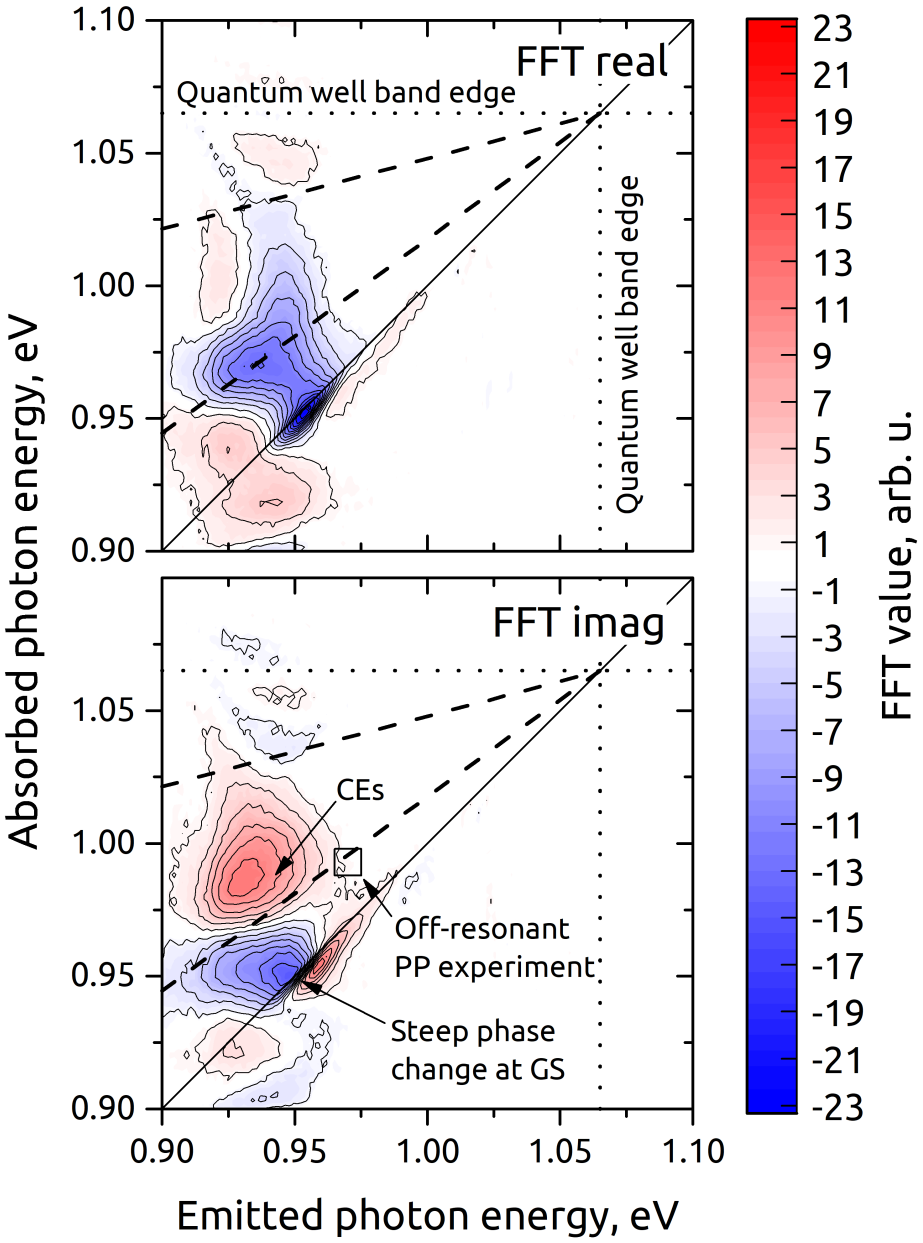

Figure 43: 2D spectrum of the unbiased SOA ($U = 0\,\mathrm{V}$) measured and aligned at $J = 0\,\mathrm{mA}$. On the emission axis, the signal is only visible where the DOS is low, in particular at energies below the GS ensemble center. The dashed lines represent the expected CE energies of the GS, $\mathrm{CE}_{\mathrm{GW}}$ (lower energy) and $\mathrm{CE}_{\mathrm{WG}}$ (higher energy), respectively.

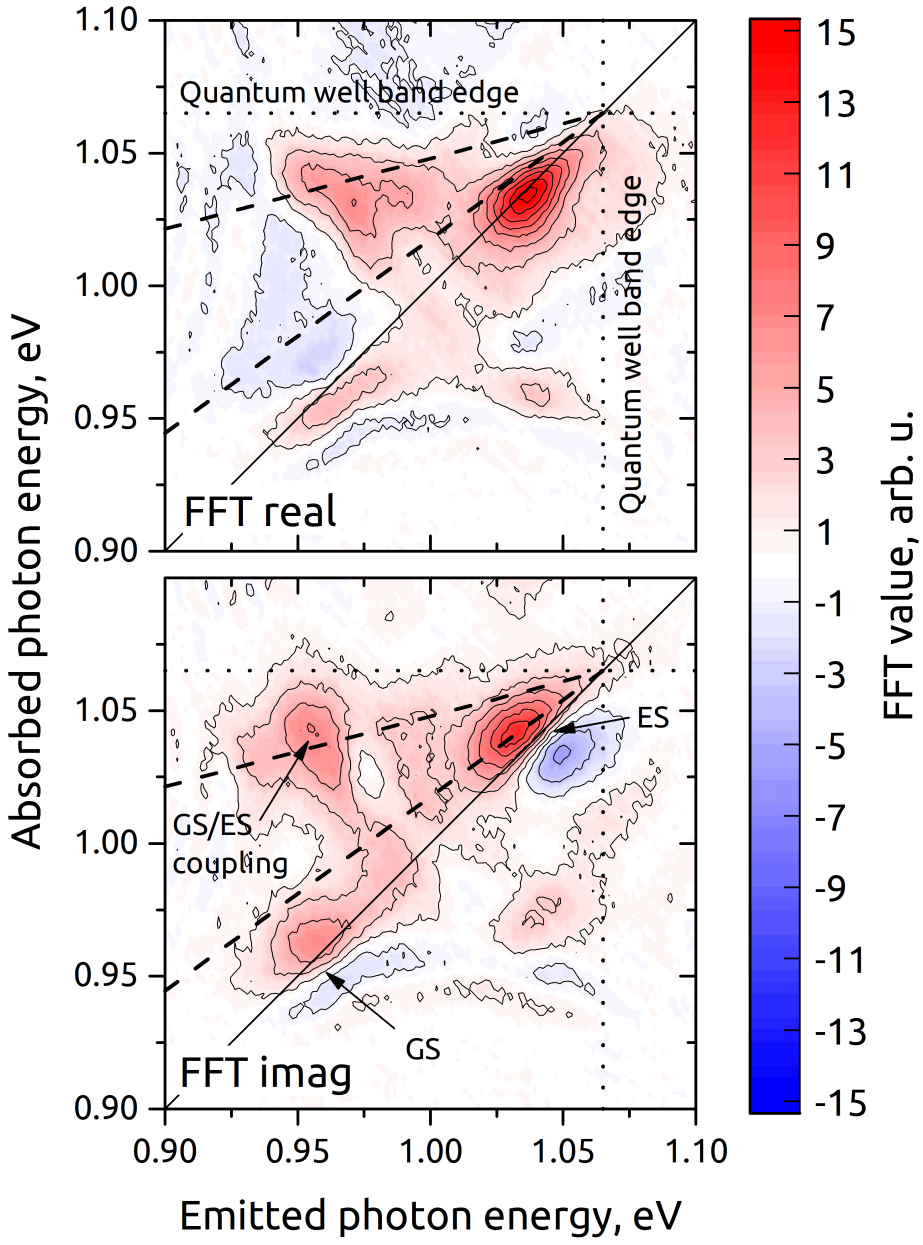

Figure 44: 2D spectrum of the SOA measured and aligned at an injection current of $J = 200\,\mathrm{mA}$. GS and ES signatures are clearly visible along the diagonal. Off–diagonal areas above and below the diagonal indicate coherent coupling between GS and ES.

11.2. Crossed Exciton signatures

From the perspective of the pure QD theory, the most intriguing feature is the wide range of off–diagonal signal in fig. 43. However, this observation is in excellent agreement with our previous assumption of CEs. The spectrum for $J = 0\,\mathrm{mA}$ resembles exactly the scenario of the PP experiments in section 10.2. In the imaginary panel, a small square indicates the energy range that has been addressed by the off–resonant PP experiment according to table 4. While it was still an open question in the PP experiment whether there was a real spectral separation of pump and probe pulse or not, the STORCH measurement provides the proof: There is coherent coupling between these two energy ranges. And more than this, it provides a much more detailed insight into the energetic structure because it covers the entire energy range.

At the moment, we are not able to fully explain the exact structure of the coupling mechanisms. This would probably require calculations of the multi–body problem of an extended number of carriers bound by the QD and for the SOA a Maxwell–Bloch approach to account for propagation effects. Today, we restrain our interpretation to a phenomenological level to motivate future applications of the STORCH technique. The pattern of the off–diagonal area can be explained by the effective mass ratio approach (section 10.1.3). Dashed lines in fig. 43 indicate the corresponding CE distribution. The 2D spectrum shows excellent agreement with this prediction. STORCH might therefore become a valuable tool to measure effective masses in the context of nanostructured devices.

11.3. Extraction of dephasing times from 2D spectra

In both cases, fig. 43 and fig. 44, the diagonal peaks exhibit a change of sign upon crossing the diagonal in the imaginary part, while the real part has a maximum. This corresponds to a phase change of π, which is in excellent agreement with the theoretical prediction for a Lorentzian (section 3.2.1). According to eq. (4.3), this allows us to extract the coherence time T_2 from the phase slope of the cross–diagonal cut. This is easier than fitting complex Lorentzians to the 2D data, because numerous features might overlap. The phase change, however, is dominated by the resonance at the diagonal, especially for large T_2 times that correspond to a steep phase slope. Be aware that this method becomes erroneous for small T_2 times and large background signals.

To extract the T_2 times for the GS as well as the ES, respective energy ranges are set. In both cases we assume a width of 40 meV. The GS area is centered at 0.97 eV, the ES area at 1.04 eV. To get an average value for these areas, 20 homogeneously distributed cross–diagonal cuts are analyzed. In a range of 2 meV, the phase slope is determined by linear fitting. The mean value and the standard deviation of these fit parameters are plotted in fig. 45.

These mean values are in excellent agreement with the results in Ref. 78 on a similar DWELL structure. This is a first proof of quality of the STORCH data with respect to the phase resolution. For low carrier injection below the GS transparency, we observe a slight increase of the dephasing time. Although the variation does not exceed the error range, this might be a hint that screening effects and a modified formation of CEs play a role in case of the presence of only a few carriers. In the high injection regime we find similar T_2 times for GS and ES. This contradicts the assumption that the GS is more isolated from the continuum states than the ES. The coupling mechanisms to the continuum seem to be more or less the same. From this perspective, there seems to be no reason why the carrier transfer between QW and QD should require a cascading process.

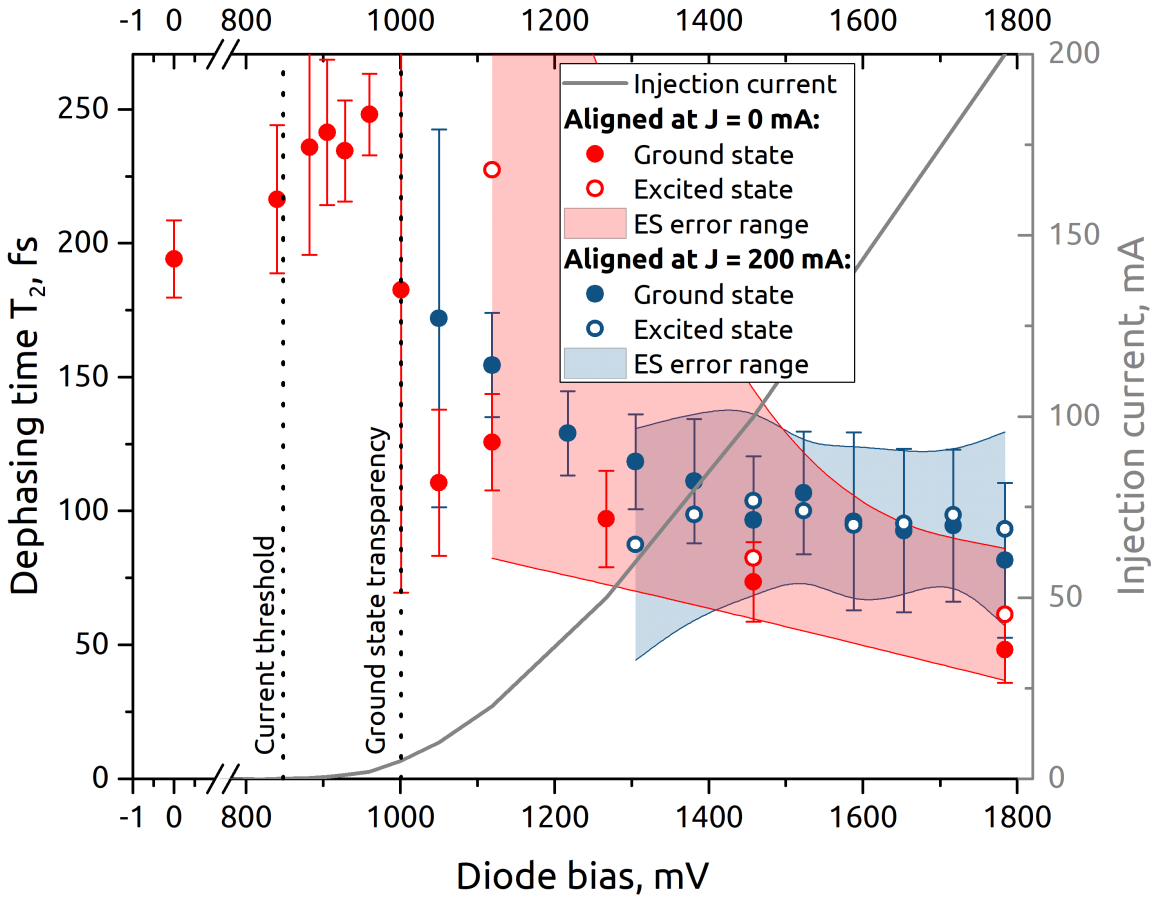

Figure 45: Coherence time T_2 over voltage. The color indicates the measurement series, solid dots represent GS data, open dots ES data. The UJ-characteristics of the SOA indicates different regimes. For low injection current, only the GS is visible. A slight rise of the T_2 time for increasing current below the transparency level might be caused by screening effects. In the high injection regime, T_2 times for GS and ES do not differ significantly, indicating similar coupling mechanisms to the environment.

Part IV.

Summary

12. A summarizing outlook

To begin a summary and a conclusion, let us start with a review of the three major sources of progress. Firstly, there is the discovery of CEs that has extended the view on QDs embedded in a continuum of states. Secondly, the improvement of the data acquisition and the development of novel experimental configurations like FROSCH and STORCH has opened new avenues. Thirdly and last—not least—the increased amount of data changed the way we analyze our data and how we plan our next steps in the lab. This last point is essential to me and I would like to add a report on software development in the following section, which can be seen as a conclusion on its own. It concludes first steps gone so far and necessary next steps to improve the cycle of experiment planning, data acquisition, data storage, data analysis, and repeated experiment planning.

12.1. The LabControl system: A versatile software concept for the optics lab

During the course of my work, I spent a large amount of time on the development of a general concept of control and storage software. The improvements to the measurement concept presented in part II revealed that the bottleneck of our experimental work is no longer the pure alignment and measurement duration, but the lacking ability to switch rapidly between experiments and to cross–evaluate different experimental data sets. Although the work presented in this section has not been finished—it has been postponed when the completion of the STORCH setup was of highest priority—I would like to give a sketch of the basic ideas. Most of them have been worked out in a test environment, but they have not yet been merged to a real *system*.

12.1.1. A little bit of dreaming

But let us start from the very end, from the picture of an ideal lab software. Think of a lab that offers a multitude of experimental configurations as soon as it is once aligned. In an ideal lab, you can easily switch between those configurations. You can use alignment tools whenever you need a little readjustment. You switch between live–mode and measurement–mode as you please. And as soon as you notice that an injection current dependence is much more interesting than the time dependence, you just switch to the variable of choice—it is not much more than a click in your user interface.

During your work on the optical table, the software supports you. All information stored on your lab computer is also available on a hand-held device. It is no longer necessary to bow down or stretch high to have a look at the lab computer monitor 5 m away—acquired data are available on your tablet PC. And every parameter that can be set via the lab computer is also adjustable via your tablet PC, of course. Two or more colleagues are working in the lab? No problem! Working with multiple tablets or other access points is supported as a matter of course. It is just a question of a few flexible access right limitations for security reasons.

After successfully taking your new data you would love to compare them to your previous data. As the system has stored all your (and your colleagues) data including all and really all parameters,

it is just a data base request to get the last years' data with the matching wavelength range and injection current setting. And as easy as the raw data, you get all your subsequent data evaluation. Of course, some things on the table have changed, some mirrors and filters have been added—but that is all documented in the software system. The computer simply compensates for the respective transfer functions and this way it is easy to compare your new data to the old one even quantitatively. So just go ahead and directly apply your prepared analysis routine. Why should you wait? An immediate evaluation might bring up new ideas, right now, right while you are able to acquire some complimentary data. And it is really astonishing how people did science before that was possible, you might think once in a while…

12.1.2. Basic software concepts

But back to reality and to what has been implemented so far. As a first step towards this ideal lab, it is necessary to set up a central control unit. This central unit is the *LabControl* system that controls all the instruments attached to its computer. The centralization is necessary to avoid conflicts between programs that run in parallel, because those conflicts often cause instrument communication failures. The LabControl system takes care of all variable parameters. The present state is always stored in an extended markup language (XML) file that literally represents the entire parameter space. This parameter space can easily have more than hundred dimensions and it would improve the long–time data reliability tremendously to always keep track of the entire space, rather than writing some seemingly important parameters to a notebook.

Besides the LabControl system, there is a completely independent user interface which is called LabCARS. It was conceptually and graphically inspired by the Library Access and Retrieval System (LCARS), the user interface of the Enterprise D in the famous TV show "Star Trek—The Next Generation". LabCARS connects to LabControl via TCP/IP and can therefore be executed on any computer within the lab network. It is quite easy to set up a local WiFi network, but for the future an integration into the university WiFi will be preferable. LabCARS is designed for mobile devices and to be used with touchscreens. Any LabCARS instance has its own copy of the LabControl XML file that is updated by the central system whenever necessary. The other way round, it is also possible to modify the central system via LabCARS. Any modification is sent as a command to LabControl which executes the command and delivers the updated state to the connected LabCARS instances.

In the present state, National Instruments (NI) LabView (LV) has been chosen as a general software platform to create both systems. While its capabilities in lab instrument interfacing are unparalleled, also mathematics and data processing provides a sufficient background to make use of its orientation towards a haptic user interface and programming style. LabControl will also in the future be based on LV, while for LabCARS a solution based on HTML and Javascript that is executed in a web browser seems preferable. The interlink will, however, still be implemente via the LabControl XML.

12.1.3. Object–oriented instrument and experiment programming

The desired flexibility is not compatible with a traditional, procedurally programmed experiment flow. In contrary, it is necessary to execute a certain type of experiment, for instance a PP experiment, with an arbitrary combination of compatible instruments (for example with another delay stage). To achieve this flexibility, we need to change our programming paradigm to object–oriented programming: Experiments as well as instruments are represented by objects and can be combined freely within defined boundaries. The state of an object is defined by its *properties* and

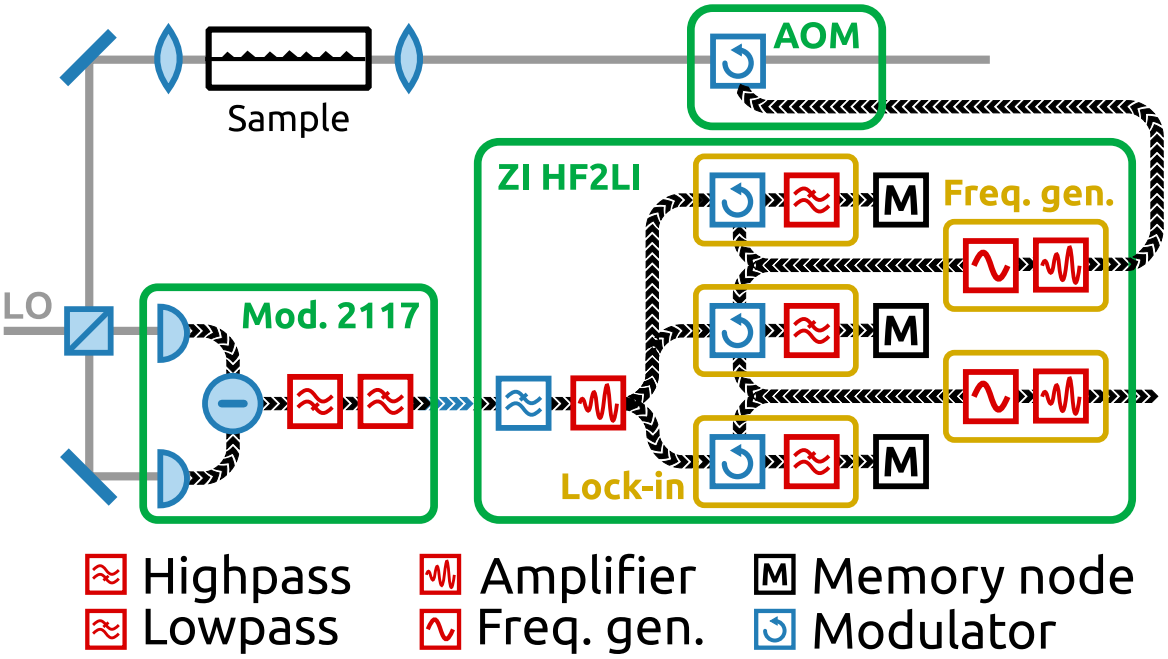

Figure 46: Scheme of a part of a heterodyne experiment split into basic elements. Some of these basic elements can be controlled by the operator (red elements), some others have fixed properties (blue elements). Often used collections of elements can be handled as *functional groups* (orange boxes). The real world instruments are represented by large collections of basic elements and functional groups (green boxes). Data are read at the memory nodes (M).

the object acts via its *methods*. This is quite exactly what we need to define a parameter space of our entire lab system (where every object defines a subspace of the lab parameter space) and to operate our lab based on these well–defined parameters.

LV offers a concept for object–oriented programming that is, however, quite limited and unhandy on first sight: Objects do no represent the state of something, but rather a blueprint of a state. It can be copied and modified without physical consequences. Within the LabControl context, I modified the LV object approach by usage of the LabControl XML file and LV *data references*. Object properties are no longer stored as variables within the object, but as entries in the XML file. Additionally, the data reference approach uses a single data memory for an object. Thereby it defines a state and not a blueprint anymore, although it is still virtual and not physical. The LabControl XML file is constructed by a simple paradigm: Every object is represented by a parent node. All object properties are stored as child nodes and the parameter value is stored as the node's text content. Any technical information that is necessary to handle the file and does not change the parameter state is stored as an attribute. This means that the full parameter space information is conserved even when all attributes are removed from the XML file.

An example of the LabControl XML file is given in appendix A. Figure 46 shows a typical experimental setting with several instruments. The scheme is constructed of certain blocks that represent software objects. Some of those object contain child objects, which corresponds to the typical tree structure of XML files. The instruments are constructed in three layers:

Basic elements are for example electrical filters or modulators, small entities that are defined by a very limited number of properties and that cannot be split into (meaningful) subentities. In fig. 46, basic elements are displayed as red and blue boxes, respectively.

Functional groups are groups of basic elements that can be interpreted as the minimal edition of a certain functionality. In fig. 46 the functional groups are surrounded by an orange box. One type of functional groups is the abstract "lock–in", a combination of a demodulator and a low–pass filter.

Physical instruments are surrounded by green boxes in fig. 46. This type of object represents a specific device, its methods typically handle the control software provided by the manufacturer.

Experiment programming is less modular because an experiment is still a procedure. Experiments are mainly based on functional groups: A sideband PP experiment, for instance, requires two abstract lock–ins, one abstract detector, two abstract AOMs, and one abstract delay line. For the experiment, it is not necessary to know which physical instrument is actually used. The experiment relies on the fact that any modification it performs on the functional group will be translated by the physical instrument according to its specific realization. In an sideband PPexperiment based on the scheme in fig. 46, the operator needs to determine which one of the lock–in functional groups is used for the sideband and which one for the main band. The LabControl system determines an appropriate memory node (block "M" in the diagram) to acquire the lock–in functional group output. The respective acquisition routine is, of course, determined in the physical instrument object class.

12.1.4. Data storage and analysis

For data storage, the LabControl system uses the NI Technical Data Management Streaming (TDMS) file format. This TDMS handling by LV is optimized to efficiently store continuous data streams to a hard-drive. The data storage has three levels: the file, channel groups, and channels. On every level, data can be labeled by user defined parameters. These parameters can later be used to browse the data storage via the LV "data finder engine". Typical labels in our experiments would be the injection current or the pump laser wavelength. With well–labeled data it would be easy to find all relevant data to compare, for instance in a defined wavelength range.

A key feature of future lab usability will be the accessibility of analysis tools. If the operator is able to apply complex analysis routines as well as individual mathematical procedures from a toolbox, the decision making during the experiment will be significantly improved. LabCARS is supposed to provide this access to analysis tools. Like many other tasks, data analysis can be split into a chain of sub–tasks. As an illustration, we can review the analysis routine that was used to create fig. 35 (c) from raw PP data:

1. Calculate the derivative of the complex PP data.
2. Smooth the derivative to eliminate outliers.
3. Set $t_{\mathrm{bc}} = 0$ at the maximum of the smoothed derivative.
4. Determine the average value of $t_{\mathrm{bc}} < -1\,\mathrm{ps}$ and subtract it from the raw data.
5. Perform a linear fit of the differential gain data in the range $1\,\mathrm{ps} \leq t_{\mathrm{bc}} \leq 5\,\mathrm{ps}$ and determine $\Delta G^{(0)}$.
6. Load the curves for all pump energies E with the same injection current J and repeat the procedure.
7. Plot $\Delta G^{(0)}$ over E.

One goal of the LabCARS development is to compose such complex analysis tasks of fundamental calculations and to make them available at lab runtime.

Experiment	Signal band	$\widehat{\nu}_\mathrm{a}$	$\widehat{\nu}_\mathrm{b}$	$\widehat{\nu}_\mathrm{c}$	t_ab	t_bc	t_cd
Traditional pump–probe	$\widehat{\nu}_\mathrm{c}$	$\widehat{\nu}_\mathrm{a}$	$\widehat{\nu}_\mathrm{a}$	$\widehat{\nu}_\mathrm{c}$	0	t_ac	0
Sideband pump–probe	$\widehat{\nu}_\mathrm{\bar{a}bc}$	$(\widehat{\nu}_\mathrm{ab} - \widetilde{\nu}_\mathrm{ab})$	$(\widehat{\nu}_\mathrm{ab} + \widetilde{\nu}_\mathrm{ab})$	$\widehat{\nu}_\mathrm{c}$	0	t_ac	0
FROSCH	$\widehat{\nu}_\mathrm{c}$			$\widehat{\nu}_\mathrm{c}$			t_cd
Pump–FROSCH	$\widehat{\nu}_\mathrm{c}$	$\widehat{\nu}_\mathrm{a}$	$\widehat{\nu}_\mathrm{a}$	$\widehat{\nu}_\mathrm{c}$	0	t_ac	t_cd
STORCH	$\widehat{\nu}_\mathrm{\bar{a}cc}$	$\widehat{\nu}_\mathrm{a}$	$\widehat{\nu}_\mathrm{c}$	$\widehat{\nu}_\mathrm{c}$	t_ac	0	t_cd

Table 6: The experiments developed in this thesis according to the A–C pulse scheme of 2DCS.

12.1.5. Transfer functions for quantitative measurements

If we look at a present FROSCH measurement, e.g. fig. 34, we are forced to display the amplitude in units of V. It is the unit that the lock–in provides, but it is not the entity that we are actually interested in. Interesting would be the field strength of the probe pulse inside the SOA, or at least as close to the SOA output facet as possible. Between the output facet and the lock–in output, there is also a chain of transfer functions:

1. Several lenses and mirrors, all with transmission/reflectance spectra $\mathfrak{T}(\nu)$ provided by the manufacturer.
2. The detector with a spectral sensitivity $\mathfrak{T}_\mathrm{det}(\nu)$, also provided by the manufacturer. If the local oscillator frequency is known, the relation between the light frequency ν and the resulting electrical $\widetilde{\nu}$ is given.
3. The low and high pass filters with $\mathfrak{T}(\widehat{\nu})$.
4. Even the coaxial cables connecting the instruments could be traced to determine signal reflections at impedance steps.
5. All the internal elements illustrated in fig. 46 also have their specific TFs.

The ultimate goal of the LabControl/LabCARS system is to image the entire setup, including every mirror and every lens. This would allow to automatically calculate the original quantities, for example the SOA output field strength from lock–in data. Such a quantitative tracing of the signal can not only improve the interpretation of data, but would also be helpful in the lab to identify for example defective components. In this context, it is very useful to think of the setup as a composite of TFs, which was the original motivation to introduce this term for all linear processes already in section 1.3.

12.2. Summary

12.2.1. Experiment development

The development of new types of heterodyne experiments was an essential part of this thesis. The results are described in part II. With FROSCH, sideband PP, and STORCH there are three novel experimental configurations. The speed of the existing traditional PP has been increased by a factor of more than 100 and SMPM has been introduced for the detailed investigation of non–linear behavior. Several minor tools like the MOLCH alignment tool improve the lab handling significantly. All these experimental configurations are based on the very same hardware and can be applied easily without realignment. The introduction of the four pulse scheme (4PS) unifies the

description of the different types of experiments. An overview of all experimental configurations is given in table 6. Beyond the unification, the 4PS forms a linguistic link to the 2DCS literature.

The STORCH setup (chapter 7) for 2DCS is at the moment the highest level of development. It merges all technical approaches developed before. After the preliminary FROSCH (section 5.2) and fast PP experiments (section 5.3) it took more than two years and several new instruments to put the setup in execution. The STORCH software analyzes a data stream of up to 16 real channels at a data acquisition rate of $\widetilde{\nu}_{\mathrm{daq}} = 20\,\mathrm{kHz}$. This allows to track temporal drifts and enables us to perform the coherent experiment over a time range of several minutes without active phase stabilization.

The technical basis of this experimental progress is the consequent exploitation of the entire frequency range displayed in fig. 1. The attosecond time range has been entered by the introduction of interferometric position control for sub–wavelength spatial resolution in the FROSCH configuration. The pico- and nanosecond time range is reserved for the physics under investigation. This range is limited by the laser repetition rate. The time range from 10 ps to 10 µs is used to perform the optical heterodyning by integration in a lock–in amplifier. Subsequently, the fDAQ range from 10 µs to 100 ms completes the time range only accessible by machinery. However, also the human time scales have been considered: The lab handling efficiency in the range of 100 ms to 1 day has been significantly increased by several live–mode applications. Finally, a development basis has been created in form of the LabControl system to store and categorize data on the time scale of months and years, which is a requirement for big data analysis.

12.2.2. Investigation of coupled nanostructures of mixed dimensionality

The new experimental capabilities allowed us to investigate the electron dynamics in the SOA on an extended scope. In a first experiment series, the 2LS nature of the QDs was demonstrated by FROSCH measurements. A characteristic pulse shape modification caused by Rabi flops was observed even at room temperature. The dependencies on injection current and pulse power were fully consistent with the expectations for this type of pulse shape modification. A theoretical description was given on a low level using a mechanical analog, and on a higher level by detailed calculations based on Maxwell–Bloch equations (calculations performed by Julian Korn and Benjamin Lingnau).

Additional optical transitions attributed to CEs were first observed in gain excitation spectroscopy. This meta–analysis of a large number of PP experiments also allowed a precise determination of the QW band edge. Two distinct peaks in the gain excitation over energy appeared above the QW band edge. These peaks can be attributed to CEs formed by an electron in the QD GS or ES, respectively, and a hole at the GaAs bulk band edge.

In a second large set of PP experiments, the diffusion dynamics in the QW as well as the excitation of the lowest energy CE have been investigated. The experiments were performed without injection current, but under variation of the diode bias. This variation had significant influence on the carrier extraction and accordingly on the decay rates of the PP traces. A total set of 178 PP traces was described by a linear rate equation model that incorporated several excitation channels and a detailed diffusion model. Fitting the model to the experimental data revealed that a large bound state of CEs is necessary to describe the diffusion behavior. The excitation efficiency of the QD GS and $\mathrm{CE}_{\mathrm{GW}}$ showed opposite bias dependence, which is an indicator for the qualitative different nature of these states.

Finally, the new STORCH setup was used to investigate the entire QD/QW energy range simultaneously by white pulses. For two measurement series—one optimized for low, the other for high injection current—the coherent coupling between the states and the coherence lifetime of GS and

ES were investigated. The extracted coherence lifetimes are in excellent agreement with literature values for similar samples, which proofs the quality of the newly developed method. Moreover, the current dependence of T_2 has been observed. There was no significant difference between GS and ES which hints to a similar coupling to the surrounding continuum. In the 2D spectra, we found distinct off–diagonal contributions that are in very good agreement with the assumption of the CE_{GW} made before. These very first findings promise a much more detailed insight into the nature of energetically widespread systems of coupled nanostructures by application of the STORCH technique.

A. LabControl XML file

The LabControl XML file defines the interplay of LabView objects within the LabControl system. A part of the LabControl class hierarchy is shown in fig. 47. Comments (red text) in the subsequent XML code explain the structure of the XML tree. Both, fig. 47 and the code, represent snapshots of the development process and do not represent a running system.

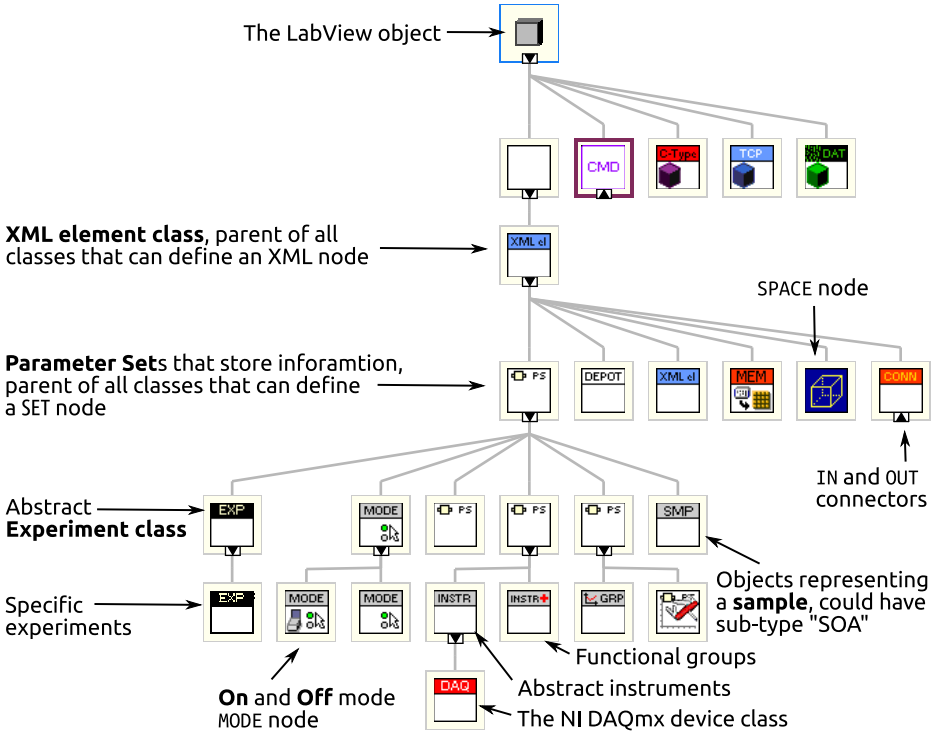

Figure 47: A part of the LabView class tree. Parent classes are shown on top, child classes that inherit properties and methods from their parent are shown below.

```
1  <?xml version="1.0" encoding="UTF-8" standalone="no" ?>
2  <LC version="1.0.0.0">
3    <!-- Begin of the library section. Holds information about publicly available classes
         ↪  and their hierarchy -->
4    <CLASS id="71C00000" label="LC XML element" lib="C:\Users\Mirco\Documents\LabVIEW
         ↪ Data\LabControl Development\Packed libraries\Basic\LabControl XML element\
         ↪ LabControl XML element.lvlibp" name="LabControl XML element">
5      <CLASS id="71D00001" label="Parameter Set" lib="C:\Users\Mirco\Documents\LabVIEW
           ↪ Data\LabControl Development\Packed libraries\Basic\Parameter Set\Parameter
           ↪ Set.lvlibp" name="Parameter Set">
6        <CLASS id="71E00002" label="Experiment" lib="C:\Users\Mirco\Documents\LabVIEW
             ↪ Data\LabControl Development\Packed libraries\Basic\Experiment\Experiment.
             ↪ lvlibp" name="Experiment">
7        </CLASS>
```

```
8       <CLASS id="71F00003" label="Functionality" lib="C:\Users\Mirco\Documents\LabVIEW
            ↪ Data\LabControl Development\Packed libraries\Basic\Functionality\
            ↪ Functionality.lvlibp" name="Functionality">
9       </CLASS>
10      <CLASS id="72000004" label="Mode" lib="C:\Users\Mirco\Documents\LabVIEW Data\
            ↪ LabControl Development\Packed libraries\Basic\Parameter Set\Parameter Set.
            ↪ lvlibp" name="Mode">
11        <CLASS id="72100005" label="FG off mode" lib="C:\Users\Mirco\Documents\LabVIEW
              ↪ Data\LabControl Development\Packed libraries\Basic\Functional group\
              ↪ Functional group.lvlibp" name="FG off mode">
12        </CLASS>
13        <CLASS id="72200006" label="FG on mode" lib="C:\Users\Mirco\Documents\LabVIEW
              ↪ Data\LabControl Development\Packed libraries\Basic\Functional group\
              ↪ Functional group.lvlibp" name="FG on mode">
14        </CLASS>
15      </CLASS>
16      <CLASS id="72300007" label="Parameter Set with Default.lvclass" lib="C:\Users\
            ↪ Mirco\Documents\LabVIEW Data\LabControl Development\Packed libraries\Basic
            ↪ \Parameter Set with Default\Parameter Set with Default.lvlibp" name="
            ↪ Parameter Set with Default">
17        <CLASS id="72400008" label="Graph" lib="C:\Users\Mirco\Documents\LabVIEW Data\
              ↪ LabControl Development\Packed libraries\Basic\Graph\Graph.lvlibp" name="
              ↪ Graph">
18        </CLASS>
19        <CLASS id="72500009" label="Graph axis" lib="C:\Users\Mirco\Documents\LabVIEW
              ↪ Data\LabControl Development\Packed libraries\Basic\Graph axis\Graph axis.
              ↪ lvlibp" name="Graph axis">
20        </CLASS>
21      </CLASS>
22      <CLASS id="7260000A" label="Sample.lvclass" lib="C:\Users\Mirco\Documents\LabVIEW
            ↪  Data\LabControl Development\Packed libraries\Basic\Sample\Sample.lvlibp"
            ↪ name="Sample">
23      </CLASS>
24      <CLASS id="7270000B" label="Spatial object" lib="C:\Users\Mirco\Documents\LabVIEW
            ↪  Data\LabControl Development\Packed libraries\Basic\Spatial object\Spatial
            ↪  object.lvlibp" name="Spatial object">
25        <CLASS id="7280000C" label="Func. group" lib="C:\Users\Mirco\Documents\LabVIEW
              ↪ Data\LabControl Development\Packed libraries\Basic\Functional group\
              ↪ Functional group.lvlibp" name="Functional group">
26          <CLASS id="7290000D" label="Frequency Generator" lib="C:\Users\Mirco\
                ↪ Documents\LabVIEW Data\LabControl Development\Packed libraries\
                ↪ Optional\Frequency generator\Frequency generator.lvlibp" name="
                ↪ Frequency generator">
27          </CLASS>
28          <CLASS id="72A0000E" label="Lock-In" lib="C:\Users\Mirco\Documents\LabVIEW
                ↪ Data\LabControl Development\Packed libraries\Optional\Lock in\Lock in.
                ↪ lvlibp" name="Lock in" refby="00000000">
29          </CLASS>
30        </CLASS>
31        <CLASS id="72B0000F" label="Instrument" lib="C:\Users\Mirco\Documents\LabVIEW
              ↪ Data\LabControl Development\Packed libraries\Basic\Instrument\Instrument.
              ↪ lvlibp" name="Instrument">
32          <CLASS id="72C00010" label="National Instruments" lib="C:\Users\Mirco\
                ↪ Documents\LabVIEW Data\LabControl Development\Packed libraries\
```

```
            ↪ Optional\National Instruments\National Instruments.lvlibp" name="
            ↪ National Instruments">
33          <CLASS id="72D00011" label="NI DAQmx device" lib="C:\Users\Mirco\Documents\
                ↪ LabVIEW Data\LabControl Development\Packed libraries\Optional\NI
                ↪ DAQmx device\NI DAQmx device.lvlibp" name="NI DAQmx device">
34          </CLASS>
35        </CLASS>
36        <CLASS id="72E00012" label="Zurich Instruments" lib="C:\Users\Mirco\Documents\
              ↪ LabVIEW Data\LabControl Development\Packed libraries\Optional\Zurich
              ↪ Instruments\Zurich Instruments.lvlibp" name="Zurich Instruments">
37          <CLASS id="72F00013" label="ZI HF2LI" lib="C:\Users\Mirco\Documents\LabVIEW
                ↪ Data\LabControl Development\Packed libraries\Optional\ZI HF2LI\ZI
                ↪ HF2LI.lvlibp" name="ZI HF2LI">
38          </CLASS>
39        </CLASS>
40      </CLASS>
41    </CLASS>
42  </CLASS>
43  <CLASS id="73000014" label="Depot.lvclass" lib="C:\Users\Mirco\Documents\LabVIEW
        ↪ Data\LabControl Development\Packed libraries\Basic\Parameter Set\Parameter
        ↪ Set.lvlibp" name="Depot">
44  </CLASS>
45  <CLASS id="73100015" label="Connector" lib="C:\Users\Mirco\Documents\LabVIEW Data\
        ↪ LabControl Development\Packed libraries\Basic\Spatial object\Spatial object.
        ↪ lvlibp" name="Connector">
46    <CLASS id="73200016" label="Input connector" lib="C:\Users\Mirco\Documents\
          ↪ LabVIEW Data\LabControl Development\Packed libraries\Basic\Spatial object\
          ↪ Spatial object.lvlibp" name="Input">
47    </CLASS>
48    <CLASS id="73300017" label="Output connector" lib="C:\Users\Mirco\Documents\
          ↪ LabVIEW Data\LabControl Development\Packed libraries\Basic\Spatial object\
          ↪ Spatial object.lvlibp" name="Output">
49    </CLASS>
50  </CLASS>
51  <CLASS id="73400018" label="Memory.lvclass" lib="C:\Users\Mirco\Documents\LabVIEW
        ↪ Data\LabControl Development\Packed libraries\Basic\Spatial object\Spatial
        ↪ object.lvlibp" name="Memory">
52  </CLASS>
53  <CLASS id="73500019" label="Space" lib="C:\Users\Mirco\Documents\LabVIEW Data\
        ↪ LabControl Development\Packed libraries\Basic\Spatial object\Spatial object.
        ↪ lvlibp" name="Space">
54  </CLASS>
55 </CLASS>
56 <!-- End of the library section, begin of the LabControl objects -->
57 <DEP depot="Functionality" id="7480002C" name="Functionalities">
58   <!-- The depot node DEP can be filled by the user with classes inheriting from the
         ↪ one defined in the "depot" attribute. The "id" value of any node is the
         ↪ reference number of the corresponding LabView data reference. -->
59   <SET class="Functionality" created_by_user="1" id="73B0001F" name="0">SBLI
60     <!-- SET nodes are "Parameter Sets" that define a certain entity in the setup.
           ↪ This one represents an object of class "Functionality". This class is used
           ↪  to attribute a certain functionality to a "Functional group". The
           ↪ functionality tag "SBLI" will be prepended to parameter names when they
```

```
        ↪ are saved to the TDMS file. This says, e.g., that the specific "functional
        ↪  group" played the role of a sideband lock-in -->
61      <PAR datatype="80" id="73A0001E" label="Description" name="description">
62        <!-- PAR nodes represent parameters that can be controlled by the user -->
63        <EL id="7390001D" name="0">0
64          <!-- To allow for array data types, the EL node represents an element of the
                ↪ array and the text content "0" determines the index of the element in
                ↪ the array. -->
65          <VAL id="7380001C" name="value">Sideband lock-in
66            <!-- Finally, the VAL node holds the value of the parameter element. In this
                  ↪  case, it is the description of the "Functionality" SET. -->
67          </VAL>
68        </EL>
69      </PAR>
70      <REF id="7360001A" name="class">
71        <!-- REF nodes are used to establish the cross-links within the XML file. While
              ↪  the PAR node defines a data value, the REF node represents a reference.
              ↪  -->
72        <VAL id="7370001B" name="0" options="/LC/CLASS//CLASS[@name='Functional group
              ↪ ']/CLASS[name(.)='CLASS']" refID="72A0000E">/LC/CLASS[@name='LabControl
              ↪ XML element']/CLASS[@name='Parameter Set']/CLASS[@name='Spatial object'
              ↪ ]/CLASS[@name='Functional group']/CLASS[@name='Lock in']
73          <!-- Also in this case, the VAL node holds the value of the reference, i.e.
                ↪ the XPath string (an XML query language) to the referenced node/object.
                ↪  Possible options are also defined as XPath in the "options" attribute.
                ↪  The "id" attribute of the referenced node will change upon a restart
                ↪ of LabControl, therefor the cross-link chosen by the user is saved as
                ↪ XPath. However, LabControl will directly after a restart translate
                ↪ this XPath to the corresponding "id" attribute and store it in the "
                ↪ refID" attribute. So it is not necessary to execute the XPath query
                ↪ every time the reference number is needed. -->
74        </VAL>
75      </REF>
76    </SET>
77    <SET class="Functionality" created_by_user="1" id="74100025" name="1">FUNCT1
78      <!-- repeating code skipped -->
79    </SET>
80    <SET class="Functionality" created_by_user="1" id="7470002B" name="2">FUNCT2
81      <!-- repeating code skipped -->
82    </SET>
83  </DEP>
84  <DEP depot="Instrument" id="82400108" name="Instruments">
85    <!-- Begin of the instrument depot -->
86    <SET class="ZI HF2LI" created_by_user="1" id="81C00100" name="1">ZI HF2LI
87      <!-- A large "Parameter Set" that defines the ZI HF2LI lock-in -->
88      <SPACE id="7490002D" name="spc">
89        <!-- Unlike the "Functionality" class, instruments define a space. Input and
              ↪ output connectors are always located on the virtual surface of such sub-
              ↪ spaces. In the far future, it might be useful to make "Instruments"
              ↪ child nodes of "Lab" nodes. -->
90      </SPACE>
91      <IN id="818000FC" male="0" name="input1" refID="" space="0" type="BNC">
92        <!-- The IN node defines an input connector. This one is a male BNC connector
              ↪ in space "0" (the outside world) and represents the "Input 1" of the
```

```
        ↪ HF2LI. The IN node is very much like the VAL child node of a REF node (
        ↪ see above): There is also a "refID" attribute that represents the output
        ↪  node that acts as the signal source. -->
93      <OUT id="819000FD" male="0" name="out" space="7490002D" type="ZI HF2LI input">
94        <!-- The output corresponding to its parent input node. It is located inside
            ↪ the HF2LI space ("space" attribute equals "id" attribute of the SPACE
            ↪ node) and has a private class type that can only be used inside the
            ↪ HF2LI. When connected, an input needs a unique source, while an output
            ↪  can serve as a source for multiple other inputs. Therefore the IN
            ↪ node has a "refNum" attribute while the OUT node does not. -->
95      </OUT>
96    </IN>
97    <IN id="81A000FE" male="0" name="input2" refID="" space="0" type="BNC">
98      <OUT id="81B000FF" male="0" name="out" space="7490002D" type="ZI HF2LI input">
99      </OUT>
100   </IN>
101   <!-- Memory nodes (MEM) for data readout are not implemented here, but they work
        ↪ just like IN nodes and thereby probe a certain OUT node -->
102   <SET class="Frequency unit" id="77400058" name="frequnit">Frequency unit
103     <!-- Because the HF2LI is a rather complex instrument, it brings some private
          ↪ classes (not found in the library section) to improve the structure.
          ↪ This one comprises the six frequency sources of the HF2LI. -->
104     <SET class="Frequency generator" id="75000034" name="freqgen1">Frequency
          ↪ generator
105       <SPACE id="74A0002E" name="spc">
106       </SPACE>
107       <MODES depot="" id="74B0002F" name="Modes" options="SET">
108         <!-- A frequency source might be switched "on" or "off" (note that "FG" is
              ↪ not for "Frequency Generator", but for "Functional Group"). Other
              ↪ modes might be defined if necessary. -->
109         <SET class="FG on mode" id="74C00030" name="on" short="?">FG on mode
110         </SET>
111         <SET class="FG off mode" id="74D00031" name="off" short="?">FG off mode
112         </SET>
113       </MODES>
114       <REF id="74E00032" name="functionality">
115         <!-- This is the attribution of the functionality. In fact, this solution of
              ↪  attributing the functionality to a functional group directly is
              ↪ deprecated and will be replaced. The attribution will be done in the
              ↪ experiment class and the functionality will also store blueprint
              ↪ settings that need to be set before the functional group can play a
              ↪ certain role in an experiment. -->
116         <VAL id="74F00033" name="0" options="/LC/DEP[@name='Functionalities']/SET[
              ↪ REF[@name='class']/VAL/@refID=/LC/CLASS//CLASS[@name='Frequency
              ↪ generator']/@id][name(.)='SET'][@class=/LC/CLASS/descendant-or-
              ↪ self::CLASS[@name='Functionality']/descendant-or-self::CLASS/@name]"
              ↪ refID="">
117         </VAL>
118       </REF>
119     </SET>
120     <SET class="Frequency generator" id="7570003B" name="freqgen2">Frequency
          ↪ generator
121       <!-- repeating code skipped -->
122     </SET>
```

```
123         <SET class="Frequency generator" id="75E00042" name="freqgen3">Frequency
                ↪ generator
124           <!-- repeating code skipped -->
125         </SET>
126         <SET class="Frequency generator" id="76500049" name="freqgen4">Frequency
                ↪ generator
127           <!-- repeating code skipped -->
128         </SET>
129         <SET class="Frequency generator" id="76C00050" name="freqgen5">Frequency
                ↪ generator
130           <!-- repeating code skipped -->
131         </SET>
132         <SET class="Frequency generator" id="77300057" name="freqgen6">Frequency
                ↪ generator
133           <!-- repeating code skipped -->
134         </SET>
135       </SET>
136       <SET class="Demodulation unit" id="817000FB" name="demodunit">Demodulation unit
137         <SET class="Lock in" id="78F00073" name="demod0">Lock in
138           <SPACE id="77500059" name="spc">
139           </SPACE>
140           <PAR datatype="43" id="7780005C" label="Time constant" name="timeconstant"
                  ↪ unit="00000000000100000000000000000000000000">
141             <EL id="7770005B" name="0">0
142               <VAL id="7760005A" name="value">3A83126F
143               </VAL>
144             </EL>
145           </PAR>
146           <PAR datatype="22" id="77B0005F" label="Slope" name="slope">
147             <OPTION id="77C00060" name="0000">
148             </OPTION>
149             <OPTION id="77D00061" name="0001">
150             </OPTION>
151             <OPTION id="77E00062" name="0002">
152             </OPTION>
153             <OPTION id="77F00063" name="0003">
154             </OPTION>
155             <OPTION id="78000064" name="0004">
156             </OPTION>
157             <OPTION id="78100065" name="0005">
158             </OPTION>
159             <OPTION id="78200066" name="0006">
160             </OPTION>
161             <OPTION id="78300067" name="0007">
162             </OPTION>
163             <EL id="77A0005E" name="0">0
164               <VAL id="7790005D" name="value" options="/LC/DEP[@name='Instruments']/SET[
                    ↪ @name='1']/SET[@name='demodunit']/SET[@name='demod0']/PAR[@name='
                    ↪ slope']/OPTION">0000
165               </VAL>
166             </EL>
167           </PAR>
168           <MODES depot="" id="78400068" name="Modes" options="SET">
169             <SET class="FG on mode" id="78500069" name="on" short="?">FG on mode
```

```
170           </SET>
171           <SET class="FG off mode" id="7860006A" name="off" short="?">FG off mode
172           </SET>
173         </MODES>
174         <REF id="7870006B" name="functionality">
175           <VAL id="7880006C" name="0" options="/LC/DEP[@name='Functionalities']/SET[
                  ↪ REF[@name='class']/VAL/@refID=/LC/CLASS//CLASS[@name='Lock in']/@id][
                  ↪ name(.)='SET'][@class=/LC/CLASS/descendant-or-self::CLASS[@name='
                  ↪ Functionality']/descendant-or-self::CLASS/@name]" refID="">
176           </VAL>
177         </REF>
178         <IN id="7890006D" name="sigout" refID="" space="77500059">
179           <OUT id="78A0006E" name="out" space="7490002D">
180           </OUT>
181         </IN>
182         <IN id="78B0006F" male="1" name="sigin" refID="" space="7490002D" type="ZI
              ↪ HF2LI input">
183           <OUT id="78C00070" name="out" space="77500059">
184           </OUT>
185         </IN>
186         <IN id="78D00071" name="freqin" refID="" space="7490002D">
187           <OUT id="78E00072" name="out" space="77500059">
188           </OUT>
189         </IN>
190       </SET>
191       <SET class="Lock in" id="7AA0008E" name="demod1">Lock in
192         <!-- repeating code skipped -->
193       </SET>
194       <SET class="Lock in" id="7C5000A9" name="demod2">Lock in
195         <!-- repeating code skipped -->
196       </SET>
197       <SET class="Lock in" id="7E0000C4" name="demod3">Lock in
198         <!-- repeating code skipped -->
199       </SET>
200       <SET class="Lock in" id="7FB000DF" name="demod4">Lock in
201         <!-- repeating code skipped -->
202       </SET>
203       <SET class="Lock in" id="816000FA" name="demod5">Lock in
204         <!-- repeating code skipped -->
205         <SPACE id="7FC000E0" name="spc">
206         </SPACE>
207         <PAR datatype="43" id="7FF000E3" label="Time constant" name="timeconstant"
              ↪ unit="00000000000100000000000000000000000000">
208         <EL id="7FE000E2" name="0">0
209         <VAL id="7FD000E1" name="value">3A83126F
210         </VAL>
211         </EL>
212         </PAR>
213         <PAR datatype="22" id="802000E6" label="Slope" name="slope">
214         <OPTION id="803000E7" name="0000">
215         </OPTION>
216         <OPTION id="804000E8" name="0001">
217         </OPTION>
218         <OPTION id="805000E9" name="0002">
```

```
219         </OPTION>
220         <OPTION id="806000EA" name="0003">
221         </OPTION>
222         <OPTION id="807000EB" name="0004">
223         </OPTION>
224         <OPTION id="808000EC" name="0005">
225         </OPTION>
226         <OPTION id="809000ED" name="0006">
227         </OPTION>
228         <OPTION id="80A000EE" name="0007">
229         </OPTION>
230         <EL id="801000E5" name="0">0
231         <VAL id="800000E4" name="value" options="/LC/DEP[@name='Instruments']/SET[
                ↪ @name='1']/SET[@name='demodunit']/SET[@name='demod5']/PAR[@name='slope
                ↪ ']/OPTION">0000
232         </VAL>
233         </EL>
234         </PAR>
235         <MODES depot="" id="80B000EF" name="Modes" options="SET">
236         <SET class="FG on mode" id="80C000F0" name="on" short="?">FG on mode
237         </SET>
238         <SET class="FG off mode" id="80D000F1" name="off" short="?">FG off mode
239         </SET>
240         </MODES>
241         <REF id="80E000F2" name="functionality">
242         <VAL id="80F000F3" name="0" options="/LC/DEP[@name='Functionalities']/SET[REF
                ↪ [@name='class']/VAL/@refID=/LC/CLASS//CLASS[@name='Lock in']/@id][name
                ↪ (.)='SET'][@class=/LC/CLASS/descendant-or-self::CLASS[@name='
                ↪ Functionality']/descendant-or-self::CLASS/@name]" refID="">
243         </VAL>
244         </REF>
245         <IN id="810000F4" name="sigout" refID="" space="7FC000E0">
246         <OUT id="811000F5" name="out" space="7490002D">
247         </OUT>
248         </IN>
249         <IN id="812000F6" male="1" name="sigin" refID="" space="7490002D" type="ZI
                ↪ HF2LI input">
250         <OUT id="813000F7" name="out" space="7FC000E0">
251         </OUT>
252         </IN>
253         <IN id="814000F8" name="freqin" refID="" space="7490002D">
254         <OUT id="815000F9" name="out" space="7FC000E0">
255         </OUT>
256         </IN>
257       </SET>
258     </SET>
259   </SET>
260   <SET class="NI DAQmx device" created_by_user="1" id="82300107" name="2">NI DAQmx
          ↪ device
261     <PAR datatype="80" id="82000104" label="Device" name="device">
262       <EL id="81F00103" name="0">0
263         <VAL id="81E00102" name="value" options="../../OPTION">
264         </VAL>
265       </EL>
```

```
        <OPTION id="82100105" name="Dev1">
        </OPTION>
        <OPTION id="82200106" name="Dev2">
        </OPTION>
      </PAR>
      <SPACE id="81D00101" name="spc">
      </SPACE>
    </SET>
  </DEP>
  <DEP depot="Experiment" id="82500109" name="Experiments">
  </DEP>
  <LIST name="VISA" ps="FALSE"/>
  <LIST name="DAQ analog inputs" ps="FALSE"/>
  <LIST name="DAQ analog outputs" ps="FALSE"/>
  <LIST name="Measurement series" ps="FALSE"/>
</LC>
```

Publications & Literature

Publications related to this work (chronological)

1. Kolarczik, M., Owschimikow, N., Korn, J., Lingnau, B., Kaptan, Y. I., Bimberg, D., Schöll, E., Lüdge, K. & Woggon, U. Quantum coherence induces pulse shape modification in a semiconductor optical amplifier at room temperature. *Nature Communications* **4,** 2953 (2013).
2. Owschimikow, N., Kolarczik, M., Kaptan, Y. I., Grosse, N. B. & Woggon, U. Crossed excitons in a semiconductor nanostructure of mixed dimensionality. *Applied Physics Letters* **105,** 101108 (2014).
3. Kolarczik, M., Owschimikow, N., Herzog, B., Buchholz, F., Kaptan, Y. I. & Woggon, U. Exciton dynamics probe the energy structure of a quantum dot-in-a-well system: The role of Coulomb attraction and dimensionality. *Physical Review B* **91,** 235310 (2015).
4. Kolarczik, M., Ulbrich, C., Geiregat, P., Zhu, Y., Sagar, L. K., Singh, A., Herzog, B., Achtstein, A. W., Li, X., van Thourhout, D., Hens, Z., Owschimikow, N. & Woggon, U. Sideband pump-probe technique resolves nonlinear modulation response of PbS/CdS quantum dots on a silicon nitride waveguide. *APL Photonics* **3,** 016101 (2018).
5. Kolarczik, M., Thommes, K., Herzog, B., Helmrich, S., Owschimikow, N. & Woggon, U. *Ultrafast photonics in coherently coupled III-V semiconductor nanostructures* in *Ultrafast Bandgap Photonics III* (ed Rafailov, M. K.) (SPIE, 2018), 17. ISBN: 9781510617872. (2018).

Publications with supporting contribution (chronological)

6. Kuhn, S. C., Knorr, A., Richter, M., Owschimikow, N., Kolarczik, M., Kaptan, Y. I. & Woggon, U. All-optical approach to determine the spatial shape of nanoscale electron wave functions using intraband spectroscopy. *Physical Review B* **89,** 201414(R) (2014).
7. Kaptan, Y. I., Schmeckebier, H., Herzog, B., Arsenijević, D., Kolarczik, M., Mikhelashvili, V., Owschimikow, N., Eisenstein, G., Bimberg, D. & Woggon, U. Gain dynamics of quantum dot devices for dual-state operation. *Applied Physics Letters* **104,** 261108 (2014).
8. Kaptan, Y. I., Röhm, A., Herzog, B., Lingnau, B., Schmeckebier, H., Arsenijević, D., Mikhelashvili, V., Schöps, O., Kolarczik, M., Eisenstein, G., Bimberg, D., Woggon, U., Owschimikow, N. & Lüdge, K. Stability of quantum-dot excited-state laser emission under simultaneous ground-state perturbation. *Applied Physics Letters* **105,** 191105 (2014).
9. Grosse, N. B., Owschimikow, N., Aust, R., Lingnau, B., Koltchanov, A., Kolarczik, M., Lüdge, K. & Woggon, U. Pump-probe quantum state tomography in a semiconductor optical amplifier. *Optics Express* **22,** 32520–32525 (2014).
10. Herzog, B., Owschimikow, N., Schulze, J.-H., Rosales, R., Kaptan, Y. I., Kolarczik, M., Switaiski, T., Strittmatter, A., Bimberg, D., Pohl, U. W. & Woggon, U. Fast gain and phase recovery of semiconductor optical amplifiers based on submonolayer quantum dots. *Applied Physics Letters* **107,** 201102 (2015).

11. Lingnau, B., Lüdge, K., Herzog, B., Kolarczik, M., Kaptan, Y. I., Woggon, U. & Owschimikow, N. Ultrafast gain recovery and large nonlinear optical response in submonolayer quantum dots. *Physical Review B* **94,** 014305 (2016).

12. Herzog, B., Lingnau, B., Kolarczik, M., Kaptan, Y. I., Bimberg, D., Maaßdorf, A., Pohl, U. W., Rosales, R., Schulze, J.-H., Strittmatter, A., Weyers, M., Woggon, U., Lüdge, K. & Owschimikow, N. Strong amplitude-phase coupling in submonolayer quantum dots. *Applied Physics Letters* **109,** 201102 (2016).

13. Singh, A., Tran, K., Kolarczik, M., Seifert, J., Wang, Y., Hao, K., Pleskot, D., Gabor, N. M., Helmrich, S., Owschimikow, N., Woggon, U. & Li, X. Long-Lived Valley Polarization of Intravalley Trions in Monolayer WSe_2. *Physical Review Letters* **117,** 257402 (2016).

14. Lingnau, B., Herzog, B., Kolarczik, M., Woggon, U., Lüdge, K. & Owschimikow, N. Dynamic phase response and amplitude-phase coupling of self-assembled semiconductor quantum dots. *Applied Physics Letters* **110,** 241102 (2017).

15. Böhm, F., Grosse, N. B., Kolarczik, M., Herzog, B., Achtstein, A., Owschimikow, N. & Woggon, U. *Quantum state reconstruction and photon number statistics for low dimensional semiconductor opto-electronic devices* in *Quantum Nanophotonics* (eds Dionne, J. A. & Lawrence, M.) (SPIE, Bellingham, Washington, USA, 2017), 5. ISBN: 9781510611757.

16. Helmrich, S., Schneider, R., Achtstein, A. W., Arora, A., Herzog, B., Vasconcellos, S. M. d., Kolarczik, M., Schöps, O., Bratschitsch, R., Woggon, U. & Owschimikow, N. Exciton–phonon coupling in mono- and bilayer $MoTe_2$. *2D Materials* **5,** 045007 (2018).

17. Steinhoff, A., Florian, M., Singh, A., Tran, K., Kolarczik, M., Helmrich, S., Achtstein, A. W., Woggon, U., Owschimikow, N., Jahnke, F. & Li, X. Biexciton fine structure in monolayer transition metal dichalcogenides. *Nature Physics,* 1199 (2018).

Literature

18. Davis, S. P., Abrams, M. C. & Brault, J. W. *Fourier transform spectrometry* ISBN: 0120425106 (Academic Press, San Diego, Calif., 2001).

19. Fatemi, F. K., Lou, J. W. & Carruthers, T. F. Frequency comb linewidth of an actively mode-locked fiber laser. *Optics Letters* **29,** 944 (2004).

20. Cundiff, S. T. & Mukamel, S. Optical multidimensional coherent spectroscopy. *Physics Today* **66,** 44–49 (2013).

21. Girod, B., Rabenstein, R. & Stenger, A. *Einführung in die Systemtheorie: Signale und Systeme in der Elektrotechnik und Informationstechnik ; mit 113 Beispielen sowie 200 Übungsaufgaben* 4., durchges. u. aktualisierte Aufl. ISBN: 978-3-8351-0176-0 (Teubner, Wiesbaden, 2007).

22. Butterworth, S. On the Theory of Filter Amplifiers. *Experimental Wireless & The Wireless Engineer,* 536–541 (1930).

23. Williams, A. B. & Taylor, F. J. *Electronic filter design handbook: LC, active, and digital filters* 2. ed. ISBN: 0-07-070434-1 (McGraw-Hill, New York, NY, 1988).

24. ed Zurich Instruments AG. *HF2 User Manual - LabOne Edition* ().

25. Haug, H. & Koch, S. W. *Quantum theory of the optical and electronic properties of semiconductors* 5th ed. ISBN: 9812838848 (World Scientific, New Jersey, op. 2009).

26. Bimberg, D., Grundmann, M. & Ledentsov, N. N. *Quantum dot heterostructures* ISBN: 0471973882 (Wiley, Chichester, 1999).
27. Tang, P. J. P., Pullin, M. J. & Phillips, C. C. Binding energy of the free exciton in indium arsenide. *Physical Review B* **55,** 4376–4381 (1997).
28. Nam, S. B., Reynolds, D. C., Litton, C. W., Almassy, R. J., Collins, T. C. & Wolfe, C. M. Free-exciton energy spectrum in GaAs. *Physical Review B* **13,** 761–767 (1976).
29. Rodt, S., Seguin, R., Schliwa, A., Guffarth, F., Pötschke, K., Pohl, U. W. & Bimberg, D. Size-dependent binding energies and fine-structure splitting of excitonic complexes in single InAs/GaAs quantum dots. *Journal of Luminescence* **122-123,** 735–739 (2007).
30. Reiss, P., Protière, M. & Li, L. Core/Shell semiconductor nanocrystals. *Small (Weinheim an der Bergstrasse, Germany)* **5,** 154–168 (2009).
31. Justo, Y., Geiregat, P., van Hoecke, K., Vanhaecke, F., de Mello Donega, C. & Hens, Z. Optical Properties of PbS/CdS Core/Shell Quantum Dots. *The Journal of Physical Chemistry C* **117,** 20171–20177 (2013).
32. Hendricks, M. P., Campos, M. P., Cleveland, G. T., Jen-La Plante, I. & Owen, J. S. A tunable library of substituted thiourea precursors to metal sulfide nanocrystals. *Science (New York, N.Y.)* **348,** 1226–1230 (2015).
33. Moreels, I., Lambert, K., Smeets, D., de Muynck, D., Nollet, T., Martins, J. C., Vanhaecke, F., Vantomme, A., Delerue, C., Allan, G. & Hens, Z. Size-dependent optical properties of colloidal PbS quantum dots. *ACS nano* **3,** 3023–3030 (2009).
34. Kambhampati, P. Multiexcitons in Semiconductor Nanocrystals: A Platform for Optoelectronics at High Carrier Concentration. *The Journal of Physical Chemistry Letters* **3,** 1182–1190 (2012).
35. Geiregat, P., Houtepen, A. J., van Thourhout, D. & Hens, Z. All-Optical Wavelength Conversion by Picosecond Burst Absorption in Colloidal PbS Quantum Dots. *ACS nano* **10,** 1265–1272 (2016).
36. De Geyter, B., Houtepen, A. J., Carrillo, S., Geiregat, P., Gao, Y., ten Cate, S., Schins, J. M., van Thourhout, D., Delerue, C., Siebbeles, L. D. A. & Hens, Z. Broadband and picosecond intraband absorption in lead-based colloidal quantum dots. *ACS nano* **6,** 6067–6074 (2012).
37. Romero-García, S., Merget, F., Zhong, F., Finkelstein, H. & Witzens, J. Silicon nitride CMOS-compatible platform for integrated photonics applications at visible wavelengths. *Optics Express* **21,** 14036–14046 (2013).
38. Melchiorri, M., Daldosso, N., Sbrana, F., Pavesi, L., Pucker, G., Kompocholis, C., Bellutti, P. & Lui, A. Propagation losses of silicon nitride waveguides in the near-infrared range. *Applied Physics Letters* **86,** 121111 (2005).
39. Bauters, J. F., Heck, M. J. R., John, D., Dai, D., Tien, M.-C., Barton, J. S., Leinse, A., Heideman, R. G., Blumenthal, D. J. & Bowers, J. E. Ultra-low-loss high-aspect-ratio Si_3N_4 waveguides. *Optics Express* **19,** 3163–3174 (2011).
40. McCutcheon, M. W. & Loncar, M. Design of a silicon nitride photonic crystal nanocavity with a Quality factor of one million for coupling to a diamond nanocrystal. *Optics Express* **16,** 19136 (2008).
41. Arango, F. B., Kwadrin, A. & Koenderink, A. F. Plasmonic antennas hybridized with dielectric waveguides. *ACS nano* **6,** 10156–10167 (2012).

42. Gruhler, N., Benz, C., Jang, H., Ahn, J.-H., Danneau, R. & Pernice, W. H. P. High-quality Si_3N_4 circuits as a platform for graphene-based nanophotonic devices. *Optics Express* **21,** 31678–31689 (2013).

43. Purnawirman, Sun, J., Adam, T. N., Leake, G., Coolbaugh, D., Bradley, J. D. B., Hosseini, E. S. & Watts, M. R. C- and L-band erbium-doped waveguide lasers with wafer-scale silicon nitride cavities. *Optics Letters* **38,** 1760 (2013).

44. Xie, W., Zhu, Y., Aubert, T., Verstuyft, S., Hens, Z. & van Thourhout, D. Low-loss silicon nitride waveguide hybridly integrated with colloidal quantum dots. *Optics Express* **23,** 12152–12160 (2015).

45. Murray, E., Ellis, D. J. P., Meany, T., Floether, F. F., Lee, J. P., Griffiths, J. P., Jones, G. A. C., Farrer, I., Ritchie, D. A., Bennett, A. J. & Shields, A. J. Quantum photonics hybrid integration platform. *Applied Physics Letters* **107,** 171108 (2015).

46. Xie, W., Stöferle, T., Rainò, G., Aubert, T., Bisschop, S., Zhu, Y., Mahrt, R. F., Geiregat, P., Brainis, E., Hens, Z. & van Thourhout, D. On-Chip Integrated Quantum-Dot-Silicon-Nitride Microdisk Lasers. *Advanced materials (Deerfield Beach, Fla.)* **29** (2017).

47. Ikeda, K., Saperstein, R. E., Alic, N. & Fainman, Y. Thermal and Kerr nonlinear properties of plasma-deposited silicon nitride/ silicon dioxide waveguides. *Optics Express* **16,** 12987 (2008).

48. Mak, K. F., Lee, C., Hone, J., Shan, J. & Heinz, T. F. Atomically thin MoS_2: a new direct-gap semiconductor. *Physical Review Letters* **105,** 136805 (2010).

49. Ruppert, C., Aslan, O. B. & Heinz, T. F. Optical properties and band gap of single- and few-layer $MoTe_2$ crystals. *Nano letters* **14,** 6231–6236 (2014).

50. He, K., Kumar, N., Zhao, L., Wang, Z., Mak, K. F., Zhao, H. & Shan, J. Tightly bound excitons in monolayer WSe_2. *Physical Review Letters* **113,** 026803 (2014).

51. Ye, Z., Cao, T., O'Brien, K., Zhu, H., Yin, X., Wang, Y., Louie, S. G. & Zhang, X. Probing excitonic dark states in single-layer tungsten disulphide. *Nature* **513,** 214 (2014).

52. Ross, J. S., Wu, S., Yu, H., Ghimire, N. J., Jones, A. M., Aivazian, G., Yan, J., Mandrus, D. G., Di Xiao, Yao, W. & Xu, X. Electrical control of neutral and charged excitons in a monolayer semiconductor. *Nature Communications* **4,** 1474 (2012).

53. Singh, A., Moody, G., Wu, S., Wu, Y., Ghimire, N. J., Yan, J., Mandrus, D. G., Xu, X. & Li, X. Coherent Electronic Coupling in Atomically Thin $MoSe_2$. *Physical Review Letters* **112** (2014).

54. Rivera, P., Schaibley, J. R., Jones, A. M., Ross, J. S., Wu, S., Aivazian, G., Klement, P., Seyler, K., Clark, G., Ghimire, N. J., Yan, J., Mandrus, D. G., Yao, W. & Xu, X. Observation of long-lived interlayer excitons in monolayer $MoSe_2$–WSe_2 heterostructures. *Nature Communications* **6,** 6242 (2015).

55. Bernardi, M., Palummo, M. & Grossman, J. C. Extraordinary sunlight absorption and one nanometer thick photovoltaics using two-dimensional monolayer materials. *Nano letters* **13,** 3664–3670 (2013).

56. Geim, A. K. & Grigorieva, I. V. Van der Waals heterostructures. *Nature* **499,** 419–425 (2013).

57. Grilli, E., Guzzi, M., Zamboni, R. & Pavesi, L. High-precision determination of the temperature dependence of the fundamental energy gap in gallium arsenide. *Physical Review B* **45,** 1638–1644 (1992).

58. Fang, Z. M., Ma, K. Y., Jaw, D. H., Cohen, R. M. & Stringfellow, G. B. Photoluminescence of InSb, InAs, and InAsSb grown by organometallic vapor phase epitaxy. *Journal of Applied Physics* **67,** 7034–7039 (1990).
59. Bryannt, G. W. Quantum dots in quantum well structures. *Journal of Luminescence* **70,** 108–119 (1996).
60. Kaiser, S., Mensing, T., Worschech, L., Klopf, F., Reithmaier, J. P. & Forchel, A. Optical spectroscopy of single InAs/InGaAs quantum dots in a quantum well. *Applied Physics Letters* **81,** 4898–4900 (2002).
61. Woggon, U. *Optical properties of semiconductor quantum dots* ISBN: 3-540-60906-7 (Springer, Berlin u.a., 1996).
62. Visimberga, G., Rainò, G., Salhi, A., Tasco, V., Todaro, M. T., Martiradonna, L., Giorgi, M. d., Passaseo, A., Cingolani, R. & Vittorio, M. d. Evidence of "crossed" transitions in dots-in-a-well structures through waveguide absorption measurements. *Applied Physics Letters* **93,** 151112 (2008).
63. Shih, C.-I., Lin, C.-H., Lin, S.-C., Lin, T.-C., Sun, K. W., Voskoboynikov, O. A., Lee, C.-P. & Suen, Y.-W. Effects of crossed states on photoluminescence excitation spectroscopy of InAs quantum dots. *Nanoscale research letters* **6,** 409 (2011).
64. Weber, M. J. *Handbook of laser wavelengths* ISBN: 0-8493-3508-6 (CRC Press, Boca Raton Fla. u.a., 1999).
65. Allen, L. & Eberly, J. H. *Optical Resonance and Two-Level Atoms* ISBN: 978-0-486-65533-8 (Dover Publications, New York, NY, 1987).
66. Ning, C. Z., Indik, R. A. & Moloney, J. V. Effective Bloch equations for semiconductor lasers and amplifiers. *IEEE Journal of Quantum Electronics* **33,** 1543–1550 (1997).
67. Bowden, C. M. & Agrawal, G. P. Generalized Bloch-Maxwell formulation for semiconductor lasers. *Optics Communications* **100,** 147–152 (1993).
68. Frimmer, M. & Novotny, L. The classical Bloch equations. *American Journal of Physics* **82,** 947 (2014).
69. Hall, K. L., Lenz, G., Ippen, E. P. & Raybon, G. Heterodyne pump–probe technique for time-domain studies of optical nonlinearities in waveguides. *Optics Letters* **17,** 874 (1992).
70. Borri, P., Langbein, W., Mørk, J. & Hvam, J. M. Heterodyne pump-probe and four-wave mixing in semiconductor optical amplifiers using balanced lock-in detection. *Optics Communications* **169,** 317–324 (1999).
71. Langbein, W. & Patton, B. Heterodyne spectral interferometry for multidimensional nonlinear spectroscopy of individual quantum systems. *Optics Letters* **31,** 1151 (2006).
72. Langbein, W. & Patton, B. Transient coherent nonlinear spectroscopy of single quantum dots. *Journal of physics. Condensed matter : an Institute of Physics journal* **19,** 295203 (2007).
73. Dyatlova, O. A., Köhler, C., Malic, E., Gomis-Bresco, J., Maultzsch, J., Tsagan-Mandzhiev, A., Watermann, T., Knorr, A. & Woggon, U. Ultrafast relaxation dynamics via acoustic phonons in carbon nanotubes. *Nano letters* **12,** 2249–2253 (2012).
74. Nighan, W. L., Gong, T., Liou, L. & Fauchet, P. M. Self-diffraction: A new method for characterization of ultrashort laser pulses. *Optics Communications* **69,** 339–344 (1989).

75. Hofmann, M., Brorson, S. D., Mørk, J. & Mecozzi, A. Time resolved four-wave mixing technique to measure the ultrafast coherent dynamics in semiconductor optical amplifiers. *Applied Physics Letters* **68,** 3236–3238 (1996).

76. Borri, P., Langbein, W., Mørk, J., Hvam, J. M., Heinrichsdorff, F., Mao, M.-H. & Bimberg, D. Dephasing in InAs/GaAs quantum dots. *Physical Review B* **60,** 7784–7787 (1999).

77. Borri, P., Langbein, W., Schneider, S., Woggon, U., Sellin, R., Ouyang, D. & Bimberg, D. Rabi oscillations in the excitonic ground-state transition of InGaAs quantum dots. *Physical Review B* **66,** 081306(R) (2002).

78. Borri, P., Schneider, S., Langbein, W., Woggon, U., Zhukov, A. E., Ustinov, V. M., Ledentsov, N. N., Alferov, Z. I., Ouyang, D. & Bimberg, D. Ultrafast carrier dynamics and dephasing in InAs quantum-dot amplifiers emitting near 1.3-μm-wavelength at room temperature. *Applied Physics Letters* **79,** 2633–2635 (2001).

79. Aue, W. P., Bartholdi, E. & Ernst, R. R. Two-dimensional spectroscopy. Application to nuclear magnetic resonance. *The Journal of Chemical Physics* **64,** 2229–2246 (1976).

80. Cundiff, S. T. Optical three dimensional coherent spectroscopy. *Physical chemistry chemical physics : PCCP* **16,** 8193–8200 (2014).

81. Cundiff, S. T. Coherent spectroscopy of semiconductors. *Optics Express* **16,** 4639 (2008).

82. Siemens, M. E., Moody, G., Li, H., Bristow, A. D. & Cundiff, S. T. Resonance lineshapes in two-dimensional Fourier transform spectroscopy. *Optics Express* **18,** 17699–17708 (2010).

83. Moody, G., Dass, C. K., Hao, K., Chen, C.-H., Li, L.-J., Singh, A., Tran, K., Clark, G., Xu, X., Berghäuser, G., Malic, E., Knorr, A. & Li, X. Intrinsic homogeneous linewidth and broadening mechanisms of excitons in monolayer transition metal dichalcogenides. *Nature Communications* **6,** 8315 (2015).

84. Kane, D. J. & Trebino, R. Characterization of arbitrary femtosecond pulses using frequency-resolved optical gating. *IEEE Journal of Quantum Electronics* **29,** 571–579 (1993).

85. Trebino, R., DeLong, K. W., Fittinghoff, D. N., Sweetser, J. N., Krumbügel, M. A., Richman, B. A. & Kane, D. J. Measuring ultrashort laser pulses in the time-frequency domain using frequency-resolved optical gating. *Review of Scientific Instruments* **68,** 3277–3295 (1997).

86. DeLong, K. W., Trebino, R., Hunter, J. & White, W. E. Frequency-resolved optical gating with the use of second-harmonic generation. *Journal of the Optical Society of America B* **11,** 2206 (1994).

87. Linden, S., Kuhl, J. & Giessen, H. in *Frequency-Resolved Optical Gating* (ed Trebino, R.) 313–322 (Springer, New York, 2000). ISBN: 978-1-4615-1181-6.

88. Nardin, G., Autry, T. M., Silverman, K. L. & Cundiff, S. T. Multidimensional coherent photocurrent spectroscopy of a semiconductor nanostructure. *Optics Express* **21,** 28617–28627 (2013).

89. Masia, F., Accanto, N., Langbein, W. & Borri, P. Spin-flip limited exciton dephasing in CdSe/ZnS colloidal quantum dots. *Physical Review Letters* **108,** 087401 (2012).

90. Suess, R. J., Jadidi, M. M., Kim, K. & Murphy, T. E. Characterization of optical nonlinearities in nanoporous silicon waveguides via pump-probe heterodyning technique. *Optics Express* **22,** 17466–17477 (2014).

91. Dommers, S. *Scattering processes in quantum dot devices with the example of an amplifier* PhD thesis (Technische Universität Dortmund, Dortmund, 2010).

92. Delmonte, V., Specht, J. F., Jakubczyk, T., Höfling, S., Kamp, M., Schneider, C., Langbein, W., Nogues, G., Richter, M. & Kasprzak, J. Coherent coupling of individual quantum dots measured with phase-referenced two-dimensional spectroscopy: Photon echo versus double quantum coherence. *Physical Review B* **96** (2017).

93. Borri, P., Langbein, W., Schneider, S., Woggon, U., Sellin, R., Ouyang, D. & Bimberg, D. Ultralong Dephasing Time in InGaAs Quantum Dots. *Physical Review Letters* **87** (2001).

94. Borri, P., Langbein, W., Hvam, J. M., Heinrichsdorff, F., Mao, M.-H. & Bimberg, D. Time-resolved four-wave mixing in InAs/InGaAs quantum-dot amplifiers under electrical injection. *Applied Physics Letters* **76,** 1380–1382 (2000).

95. Hopf, F. A. & Scully, M. O. Theory of an Inhomogeneously Broadened Laser Amplifier. *Physical Review* **179,** 399–416 (1969).

96. Karni, O., Capua, A., Eisenstein, G., Sichkovskyi, V., Ivanov, V. & Reithmaier, J. P. Rabi oscillations and self-induced transparency in InAs/InP quantum dot semiconductor optical amplifier operating at room temperature. *Optics Express* **21,** 26786–26796 (2013).

97. Capua, A., Karni, O., Eisenstein, G., Sichkovskyi, V., Ivanov, V. & Reithmaier, J. P. Coherent control in a semiconductor optical amplifier operating at room temperature. *Nature Communications* **5,** 5025 (2014).

98. Suzuki, T., Singh, R., Bayer, M., Ludzwig, A., Wieck, A. D. & Cundiff, S. T. Detuning dependence of Rabi oscillations in an InAs self-assembled quantum dot ensemble. *Physical Review B* **97** (2018).

99. Lingnau, B. C. O. *Nonlinear and nonequilibrium dynamics of quantum-dot optoelectronic devices* 2015.

100. Lingnau, B. & Lüdge, K. Rabi-oscillation-enhanced frequency conversion in quantum-dot semiconductor optical amplifiers. *Optical and Quantum Electronics* **50,** 1139 (2018).

101. Majer, N., Lüdge, K. & Schöll, E. Cascading enables ultrafast gain recovery dynamics of quantum dot semiconductor optical amplifiers. *Physical Review B* **82,** 829 (2010).

102. Kolarczik, M. *Zwei-Farben-Spektroskopie an Nanostrukturen: 0D-2D-Kopplung am Beispiel von DWELL-Strukturen* diploma thesis (Technische Universität Berlin, Berlin, 2012).

103. Kim, J., Laemmlin, M., Meuer, C., Bimberg, D. & Eisenstein, G. Theoretical and Experimental Study of High-Speed Small-Signal Cross-Gain Modulation of Quantum-Dot Semiconductor Optical Amplifiers. *IEEE Journal of Quantum Electronics* **45,** 240–248 (2009).

104. *Ultrafast Lasers Based on Quantum Dot Structures: Physics and Devices* 1. Aufl. (eds Rafailov, E. U., Cataluna, M. A. & Avrutin, E. A.) ISBN: 9783527634484 (Wiley-VCH, s.l., 2011).

105. Kuhn, S. C. & Richter, M. Excitonic effects in intraband quantum dot spectroscopy: Formation of bound continuum excitons. *Physical Review B* **90,** 125308 (2014).

106. Jones, E. D., Lyo, S. K., Fritz, I. J., Klem, J. F., Schirber, J. E., Tigges, C. P. & Drummond, T. J. Determination of energy-band dispersion curves in strained-layer structures. *Applied Physics Letters* **54,** 2227–2229 (1989).

107. Lee, K.-S., Lee, C.-D., Kim, Y. & Kyu Noh, S. Dependence of the heavy-hole exciton reduced mass on quantum-well size in InGaAs/GaAs heterostructures. *Solid State Communications* **128,** 177–180 (2003).

108. Alavi, K., Aggarwal, R. & Groves, S. Interband magnetoabsorption of $In_{0.53}Ga_{0.47}As$. *Physical Review B* **21,** 1311–1315 (1980).

109. Cedola, A., Cappelluti, F. & Gioannini, M. Dependence of quantum dot photocurrent on the carrier escape nature in InAs/GaAs quantum dot solar cells. *Semiconductor Science and Technology* **31,** 025018 (2016).

110. Sanguinetti, S., Henini, M., Grassi Alessi, M., Capizzi, M., Frigeri, P. & Franchi, S. Carrier thermal escape and retrapping in self-assembled quantum dots. *Physical Review B* **60,** 8276–8283 (1999).

111. Sanguinetti, S., Mano, T., Oshima, M., Tateno, T., Wakaki, M. & Koguchi, N. Temperature dependence of the photoluminescence of InGaAs/GaAs quantum dot structures without wetting layer. *Applied Physics Letters* **81,** 3067–3069 (2002).

112. Ferreira, R. & Bastard, G. Phonon-assisted capture and intradot Auger relaxation in quantum dots. *Applied Physics Letters* **74,** 2818–2820 (1999).

113. O'Driscoll, I., Piwonski, T., Schleussner, C.-F., Houlihan, J., Huyet, G. & Manning, R. J. Electron and hole dynamics of InAs/GaAs quantum dot semiconductor optical amplifiers. *Applied Physics Letters* **91,** 071111 (2007).

114. Mazur, Y. I., Liang, B. L., Wang, Z. M., Guzun, D., Salamo, G. J., Zhuchenko, Z. Y. & Tarasov, G. G. Excitonic transfer in coupled InGaAs/GaAs quantum well to InAs quantum dots. *Applied Physics Letters* **89,** 151914 (2006).

115. Borri, P., Langbein, W., Woggon, U., Schwab, M., Bayer, M., Fafard, S., Wasilewski, Z. & Hawrylak, P. Exciton dephasing in quantum dot molecules. *Physical Review Letters* **91,** 267401 (2003).

116. Wang, L., Rastelli, A., Kiravittaya, S., Atkinson, P., Ding, F., Bufon, C. C. B., Hermannstädter, C., Witzany, M., Beirne, G. J., Michler, P. & Schmidt, O. G. Towards deterministically controlled InGaAs/GaAs lateral quantum dot molecules. *New Journal of Physics* **10,** 045010 (2008).

117. Dawson, P., Rubel, O., Baranovskii, S. D., Pierz, K., Thomas, P. & Göbel, E. O. Temperature-dependent optical properties of InAs/GaAs quantum dots: Independent carrier versus exciton relaxation. *Physical Review B* **72,** 155 (2005).

118. Stufler, S., Ester, P., Zrenner, A. & Bichler, M. Power broadening of the exciton linewidth in a single InGaAs/GaAs quantum dot. *Applied Physics Letters* **85,** 4202–4204 (2004).

119. Williams, K. J., Esman, R. D. & Dagenais, M. Effects of high space-charge fields on the response of microwave photodetectors. *IEEE Photonics Technology Letters* **6,** 639–641 (1994).

Symbols

$\mathcal{B}$ Magnetic field 19

c_0 Vacuum speed of light 6
χ Electric susceptibility 19

$\mathcal{D}$ Electric displacement field 19
ΔG Differential gain 9
$\Delta\Phi$ Differential phase 47

$\mathcal{E}$ Electric field 6
E General energy 2
$\mathcal{E}_{2\mathrm{D}}$ 2D spectrum 59
η Extraction efficiency 73

$\mathcal{F}$ Fourier transformation 2

Γ Transition rate 12
γ Homogeneous linewidth (typically with 2γ FWHM of a Lorentzian) 21

$\mathcal{H}$ Magnetizing field 19
h The Planck constant 2
  $\hbar$ Reduced Planck constant $h/(2\pi)$ 2

J SOA injection current. 62

k_B The Boltzmann constant 13

$\mathcal{M}$ Magnetization 19
m Mass 6
  m_0 Electron rest mass 11
  m^* Effective mass 11
    m_e^* Effective electron mass 70
    m_h^* Effective hole mass 70
    m_x^* Effective exciton mass 77

n Refractive index 6
ν Light frequency 2
$\widehat{\nu}$ General mode shift frequency 7
  $\widehat{\nu}_\mathrm{rep}$ Laser repetition rate 5
$\widetilde{\nu}$ General modulation frequency
  $\widetilde{\nu}_\mathrm{daq}$ Data acquisition rate 37

Ω Rabi frequency 23
ω Angular frequency $\omega = 2\pi\nu$. 2

$\mathcal{P}$ Polarization 19
P General power 9
  $P_{\max}$ Maximum power in an SMPM. 39

$\mathfrak{r}$ Effective mass ratio $m_{\mathrm{h}}^*/m_{\mathrm{e}}^*$ 70
$\boldsymbol{\rho}$ Bloch vector
  v Absorptive component of dipole moment 23
  w Inversion 23

σ Inhomogeneous linewidth (typically with σ FWHM of a Gaussian) 2

T the temperature 77
T_1 Population lifetime 23
T_2 Coherence lifetime 23
t_{ij} General delay of pulse i and pulse j
  t_{ab} Pulse delay in FWM experiments 32
    $t_{\mathrm{ab}}^{(0)}$ Uncorrected pulse delay in FWM experiments 58
  t_{ac} Delay between the two pulses passing the sample. Can either be equivalent to t_{ab} or t_{bc}. 30
  t_{bc} Pump–probe delay in pump–probe experiments 30
  t_{cd} Local oscillator delay 30
    $t_{\mathrm{cd}}^{(0)}$ Uncorrected local oscillator delay 58
τ General decay time
  τ_{TC} Lock-in time constant 9

U SOA bias. 62
U_{th} Injection threshold bias of the SOA. 62

Abbreviations

Notation	Description	Page List
0D	zero–dimensional	12
2D	two–dimensional	12
2DCS	two-dimensional coherent spectroscopy	viii, 8
2LS	two level system	viii, 23
2cPP	two-color pump-probe	68
3D	three–dimensional	12
4PS	four pulse scheme	ix, 8, 20
ADC	analog–to–digital converter	37
AOM	acousto-optic modulator	7
ASE	amplified spontaneous emission	15
CB	conduction band	11
CCD	charge–coupled device	29
CE	crossed exciton	14
DAQ	data acquisition	vii, 37
DC	direct current	52
DEQ	differential equation	16
DFG	Deutsche Forschungsgemeinschaft	vi
DOS	density of states	11
DWELL	dot–in–a–well	16
ES	excited state	12
fDAQ	fast data acquisition	38
FROSCH	Frequency Resolved Optical Short–pulse Characterization by Heterodyning	ii, vii, 31
FT	Fourier transform	2
FTS	Fourier transform spectroscopy	viii, 30
FWHM	full width at half maximum	2
FWM	four-wave mixing	19
GaAs	gallium arsenide	71
GPIB	General Purpose Interface Bus	vii

Notation	Description	Page List
GRK 1558	Graduiertenkolleg 1558	vi
GS	ground state	12
GT	Gabor transform	4
InAs	indium arsenide	viii
InGaAs	indium gallium arsenide	viii
IR	infrared	11
LED	light emitting diode	15
LO	local oscillator	28
LV	LabView	93
MBE	molecular beam epitaxy	13
MDCS	multi-dimensional coherent spectroscopy	32
MOLCH	More–Or–Less Characterization by Heterodyning	vii, 38
MOVPE	metalorganic vapor–phase epitaxy	13
NI	National Instruments	93
NIR	near infrared	14
NMR	nuclear magnetic resonance	32
OPO	optical parametric oscillator	21
PL	photoluminescence	17
PP	pump-probe	vii, 14
QD	quantum dot	viii, 6
QW	quantum well	viii, 12
RWA	rotating wave approximation	23
SFB 787	Sonderforschungsbereich 787	vi
SHG	second harmonic generation	35
SK	Stranski-Krastanow	13
SMPM	Simultaneous multi-power measurement	vii, 39
SNR	signal–to–noise ratio	37
SOA	semiconductor optical amplifier	viii, 15
STORCH	Supercontinuum–based Two–dimensional Observation of Radiation Coherence by Heterodyning	viii

Notation	Description	Page List
TC	time constant	38
TDMS	Technical Data Management Streaming	95
TF	transfer function	8
TMD	transitionmetal-dichalcogenide	vi, vii, 14
TU	Technische Universität Berlin	vi
UT	University of Texas	vi
UV	ultraviolet	11
VB	valence band	11
VIS	visible	20
WL	wetting layer	13
XML	extended markup language	93
ZI	Zurich Instruments	10

List of Figures